CANADIAN HYDRAULICS CENTRE
CENTRE D'HYDRAULIQUE CANADIEN

HYDRODYNAMIC IMPACTS OF POWER GENERATION BY TIDAL LAGOONS IN THE BAY OF FUNDY

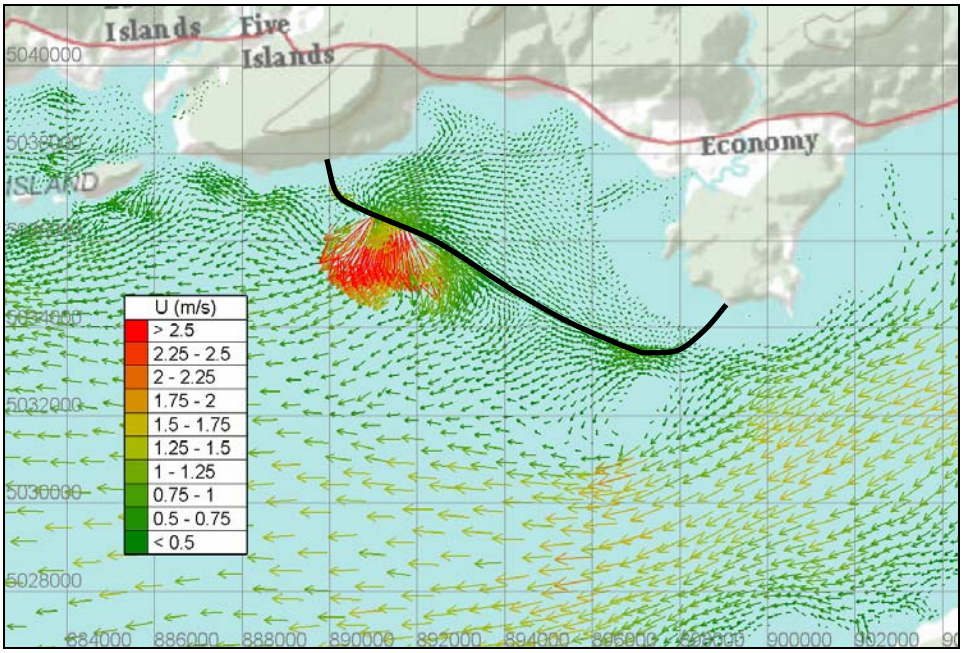

A. Cornett, J. Cousineau

CHC-TR-084

December 2011

National Research Council Canada
Conseil national de recherches Canada

CANADIAN HYDRAULICS CENTRE
CENTRE D'HYDRAULIQUE CANADIEN

Hydrodynamic impacts of power generation by tidal lagoons in the Bay of Fundy

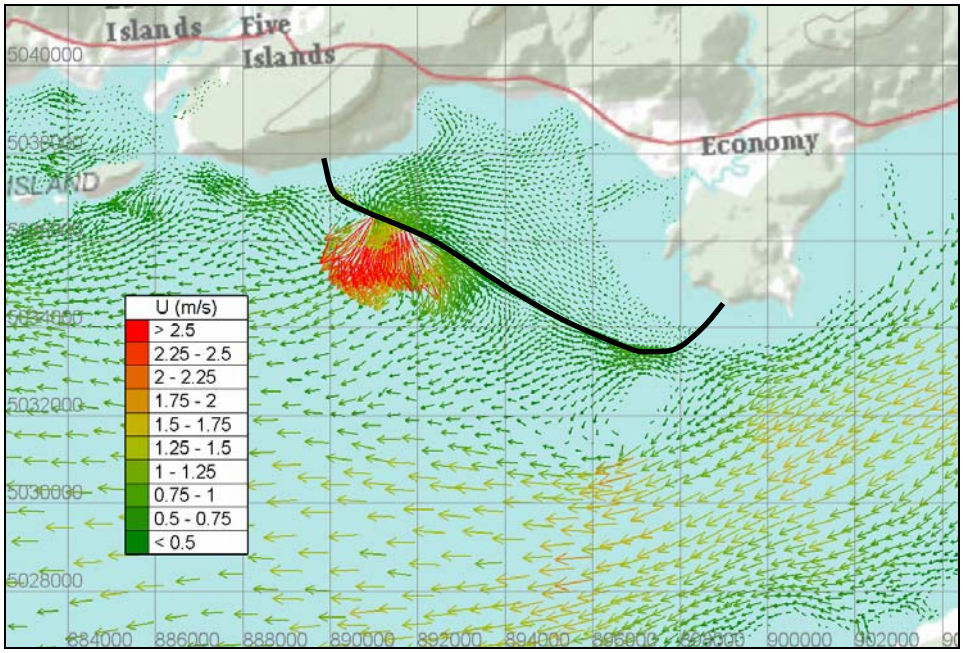

Technical Report CHC-TR-084

December 2011

A. Cornett, J. Cousineau
Canadian Hydraulics Centre
National Research Council Canada
Ottawa, K1A 0R6, Canada

National Research Council Canada | Conseil national de recherches Canada

Abstract

The Bay of Fundy in eastern Canada is renowned for its high tides, which are among the world's largest; and for this reason, the Bay of Fundy (BoF) has long been recognized as one of the world's premier locations for deployment of tidal power generation systems. The large tides are a result of the near-resonant response of the BoF-GoM system to the M_2 tidal forcing.

The tidal barrage at Annapolis Royal has been operating successfully since 1984; however, because of hydrodynamic and environmental impacts upstream of this barrage, this type of tidal power development remains highly controversial. Tidal power lagoons are an alternative approach to tidal power conversion that attempts to achieve high efficiency while avoiding some of the environmental problems associated with tidal barrages. A typical tidal power lagoon consists of a large impoundment structure (a rubble-mound dyke or caisson) and a power-house containing sluices and conventional low-head hydroelectric generating equipment, situated a mile or more offshore in an area with shallow depths and high tides. While tidal power lagoons are believed to be technically feasible and efficient, their potential effects on the hydrodynamics of the BoF-GoM tidal system has not been investigated previously and remains unknown. The main objective of the study described in this report was to discover and assess the scale and character of the changes in tidal hydrodynamics that would be caused by tidal power lagoons operating in the upper part of the Bay.

A detailed two-dimensional hydrodynamic model, based on the TELEMAC modelling system, has been developed to simulate tidal flows in the Bay of Fundy and Gulf of Maine. The model has been well calibrated and validated against water level and velocity data. Twenty different versions of the model have been developed to simulate existing conditions and nineteen hypothetical scenarios with one or more tidal power lagoons operating in the upper Bay. Methods were developed to simulate, numerically, the flows through low-head turbines and sluices, and the storage and release of water from a lagoon impoundment. Tidal power lagoons, varying in size from 12 km^2 up to 58 km^2, have been simulated at six prospective sites, three sites in Minas Basin and three in Chignecto Bay. In one scenario, the effect of six lagoons working together, one at each site, was investigated. The changes in tidal hydrodynamics throughout the BoF and GoM due to the presence and operation of one or more tidal lagoons have been estimated by differencing results from simulations with lagoons and an equivalent simulation of existing conditions without lagoons. The sensitivities to changes in lagoon location, lagoon size, lagoon type, the number of lagoons and their location have all been investigated. Moreover, relationships that describe the trade-off between power generation from lagoons and the magnitude of the resulting hydrodynamic change have been developed for several major communities around the BoF and GoM.

The methods employed in the study and the results of these simulations are presented and discussed in this report. These results will help inform current and future policies concerning the development of the vast tidal energy resources in the Bay of Fundy.

Table of Contents

Page

Abstract ..... **i**

Table of Contents ..... **ii**

List of Tables ..... **iv**

List of Figures ..... **iv**

1 Introduction **1**

1.1 Tidal Lagoon Concept 2

1.2 Study Objective 6

1.3 Previous Investigations 6

2 Model Development and Calibration **16**

2.1 Model Development 16

2.2 Model Grids 17

2.3 Boundary conditions 20

2.4 Model Calibration 20

3 Numerical Simulation of Tidal Power Lagoons **25**

3.1 Simulation of Sluices and Turbines 26

3.2 Operating Modes 28

3.3 Power Output 32

3.4 Analytical Model of Plant Operations 32

4 Modelled Scenarios **35**

5 Results & Discussion **41**

5.1 Existing Conditions, Scenario S0 41

5.2 Single Coastal and Offshore Lagoons at Site A, Scenarios S1 and S2 46

5.3 Influence of Operating Mode, Scenarios S3-S5 54

5.4 Influence of Lagoon Size. Scenarios S3, S8-S12 59

5.5 Influence of Lagoon Location, Scenarios S3, S13, S14 66

5.6 Three Lagoons in Minas Basin, Scenarios S15, S16 69

5.7 Three Lagoons in Minas Basin, Scenarios S17, S18 72

5.8 Six Lagoons in Minas Basin and Chignecto Bay, Scenario S19 75

5.9 Summary of Hydrodynamic Impacts at Reference Sites 77

5.10 Relationships between power output and hydrodynamic impact 79

6 Conclusions 87
7 Acknowledgment 90
8 References & Bibliography 90

List of Tables

Page

Table 1. Summury of time periods used for model calibration and validation. 21
Table 2. Summary of validation errors for reference stations 1-15. 23
Table 3. Summary of ADCP datasets consulted for model validation. 24
Table 4. Turbine performance relationships employed in this study. 27
Table 5. Properties of numerical tidal power lagoons considered in this study. 36
Table 6. Description of scenarios S1-S19. 40
Table 7. Summary of hydrodynamic changes at reference sites for scenarios S1-S19. 78

List of Figures

Page

Figure 1. Gulf of Maine and Bay of Fundy, with reference stations 1-15. 1
Figure 2. Maximum tide range in the upper Bay of Fundy. 2
Figure 3. Artist's renderings: a) offshore lagoon; b) coastal lagoon. 3
Figure 4. Offshore and coastal lagoons proposed by DMC [11]. 4
Figure 5. Typical dyke section with geo-bag sand core protected with armour stone and x-bloc units. 4
Figure 6. Typical turbine caisson section. 5
Figure 7. Typical sluice caisson section. 5
Figure 8. Minas Passage is a 5 km wide channel located in the upper Bay of Fundy (view looking SW). 7
Figure 9. Depth averaged currents in Minas Passage: a) spring flood; b) spring ebb. 8
Figure 10. Depth-averaged and time-averaged kinetic power density at Minas Passage. 9
Figure 11. Vertical profile of velocity and kinetic power for a site in northern Minas Passage. 10
Figure 12. Map of the Severn Estuary showing the location of the Fleming Lagoon and the Cardiff-Weston (Severn) Barrage. 12
Figure 13. Severn Estuary bathymetry with the Severn Barrage and the Fleming Lagoon (Xia et al., 2010). 12
Figure 14. Representation of the Fleming Lagoon in the numerical model (Xia et al., 2010). 13
Figure 15. Numerical simulation of flows near the power house during: a) flood; b) ebb (Xia et al., 2010). 13
Figure 16. Numerical prediction of maximum water level for: a) existing conditions; b) with the Severn Barrage; c) with the Fleming Lagoon (Xia et al., 2010). 14

Figure 17. Numerical prediction of maximum velocity for: a) existing conditions; b) with the Severn Barrage; c) with the Fleming Lagoon (Xia et al., 2010). 15
Figure 18. Model domain, finite element mesh and bathymetry. 18
Figure 19. Model mesh and variable grid resolution. 19
Figure 20. Spatial coverage of bathymetric data sets. 20
Figure 21. Simulated and observed water levels for September 2007. 22
Figure 22. Simulated and observed depth-averaged velocity for a site in Minas Basin. 24
Figure 23. Numerical representation of tidal power lagoons. 25
Figure 24. Arrangement of numerical turbines and sluices. 26
Figure 25. Performance curves for a double-regulated bulb turbine (after Baker, 1991). 27
Figure 26. Turbine performance curves employed in this study. 28
Figure 27. Illustration of ebb generation. 29
Figure 28. Illustration of flood generation. 30
Figure 29. Illustration of bi-directional generation. 31
Figure 30. Temporal fluctuations of water level and power output for a bi-directional power generation protocol. 32
Figure 31. Water level – area curves for several coastal lagoons. 34
Figure 32. Optimisation of powerhouse configuration for lagoon A_C1, 2-way generation. 34
Figure 33. Sites A-F are located on the shallow tidal flats in Minas Basin and Chignecto Bay. . 35
Figure 34. Arrangement of coastal tidal lagoons at sites A-F. 37
Figure 35. Arrangement of offshore tidal lagoons at sites A-F. 37
Figure 36. Computational meshes for simulationg coastal and offshore lagoons at site A 38
Figure 37. Bathymetry for the upper Bay of Fundy. 43
Figure 38. Maximum tide range for existing conditions (scenario S0). 43
Figure 39. Spring tide flood currents at Minas Passage for existing conditions (scenario S0). .. 44
Figure 40. Spring tide ebb currents at Minas Passage for existing conditions (scenario S0). 44
Figure 41. Maximum depth-averaged current speed U_{max} for existing conditions (scenario S0). 45
Figure 42. Depth-averaged RMS current speed U_{RMS} for existing conditions (scenario S0). 45
Figure 43. Maximum bed shear stress τ_{max} for existing conditions (scenario S0). 46
Figure 44. Change in maximum tide range for scenarios S1 and S2. 47
Figure 45. Change in maximum water level for scenarios S1 and S2. 48
Figure 46. Velocity field near a 26.7 km^2 coastal lagoon during a) flood and b) ebb, (2-way generation). 50

Figure 47. Local change in U_{max} and residual circulation for scenarios S1 and S2. 51
Figure 48. Far-field change in U_{max} for scenarios S1 and S2..... 52
Figure 49. Predicted change in maximum bed shear stress for scenarios S1 and S2. 53
Figure 50. Power output for scenarios S3-S5. 55
Figure 51. Change in maximum tide range for scenarios S3-S7. 56
Figure 52. Change in U_{RMS} for scenarios S3-S7. 57
Figure 53. Change in U_{max} and residual circulation for scenarios S3-S7. 58
Figure 54. Change in maximum tide range for scenarios S3, S8 and S9. 60
Figure 55. Far-field change in U_{RMS} for scenarios S3, S8 and S9. 61
Figure 56. Local change in U_{RMS} and residual current for scenarios S3, S8 and S9. 62
Figure 57. Change in maximum tide range for scenarios S10-S12. 63
Figure 58. Far-field change in U_{RMS} for scenarios S10-S12. 64
Figure 59. Local change in U_{RMS} and residual current for scenarios S10-S12. 65
Figure 60. Change in maximum tide range for scenarios S3, S13 and S14. 67
Figure 61. Far-field change in U_{RMS} for scenarios S3, S13 and S14. 68
Figure 62. Change in maximum tide range for scenarios S15 and S16. 70
Figure 63. Far-field change in U_{RMS} for scenarios S15 and S16. 71
Figure 64. Change in maximum tide range for scenarios S17 and S18. 73
Figure 65. Far-field change in U_{RMS} for scenarios S17 and S18. 74
Figure 66. Change in maximum tide range for scenario S19. 75
Figure 67. Far-field change in U_{RMS} for scenario S19. 76
Figure 68. Map of reference stations and reference sites..... 77
Figure 69. Relationship between lagoon area and power output. 79
Figure 70. Influence of power generation by tidal lagoons on the maximum tide range at Boston. 81
Figure 71. Influence of power generation by tidal lagoons on the maximum tide range at Bar Harbor..... 81
Figure 72. Influence of power generation by tidal lagoons on the maximum tide range at Saint John. 82
Figure 73. Influence of power generation by tidal lagoons on the maximum tide range at Chignecto. 82
Figure 74. Far field change in maximum tide range due to tidal power lagoons in Minas Basin. 84
Figure 75. Change in maximum tide range versus distance for scenarios S3-S7. 85

Figure 76. Change in maximum depth-averaged current speed versus distance for scenarios S3-S7. 85

Figure 77. Influence of power generation by tidal lagoons on current speed at Minas Passage. 86

Figure 78. Influence of power generation by lagoons at site A on current speed at Minas Passage. 86

1 Introduction

The Bay of Fundy (BoF), located on the Atlantic coast of North America between the Canadian provinces of Nova Scotia and New Brunswick, is renowned for its impressive tides, which are among the world's largest. Because of the large tide range and the strong tidal currents that arise in certain locations, the BoF has long been recognized as an ideal site for tidal energy projects. For example, the BoF is home to the Annapolis Royal Generating Station, a tidal barrage with 20 MW installed capacity constructed on the Annapolis River, which has been operating since 1984, and is one of three tidal barrages constructed worldwide to date. There is also considerable interest nowadays in deploying in-stream turbines to extract energy from the strong currents flowing through Minas Passage and other smaller channels. The Fundy Ocean Research Center for Energy (FORCE) is currently investing on the order of $80M to develop a test centre for tidal energy technologies in the upper BoF near the north shore of Minas Passage.

The main part of the BoF is approximately 45 km wide by roughly 200 km long (see Figure 1). The upper part of the BoF bifurcates into two smaller bays, known as Chignecto Bay to the north, and Minas Passage leading to Minas Basin to the east (see Figure 2). The eastern part of Minas Basin is known as Cobequid Bay, while Cumberland Basin and Shepody Bay are located in the upper (northern) part of Chignecto Bay.

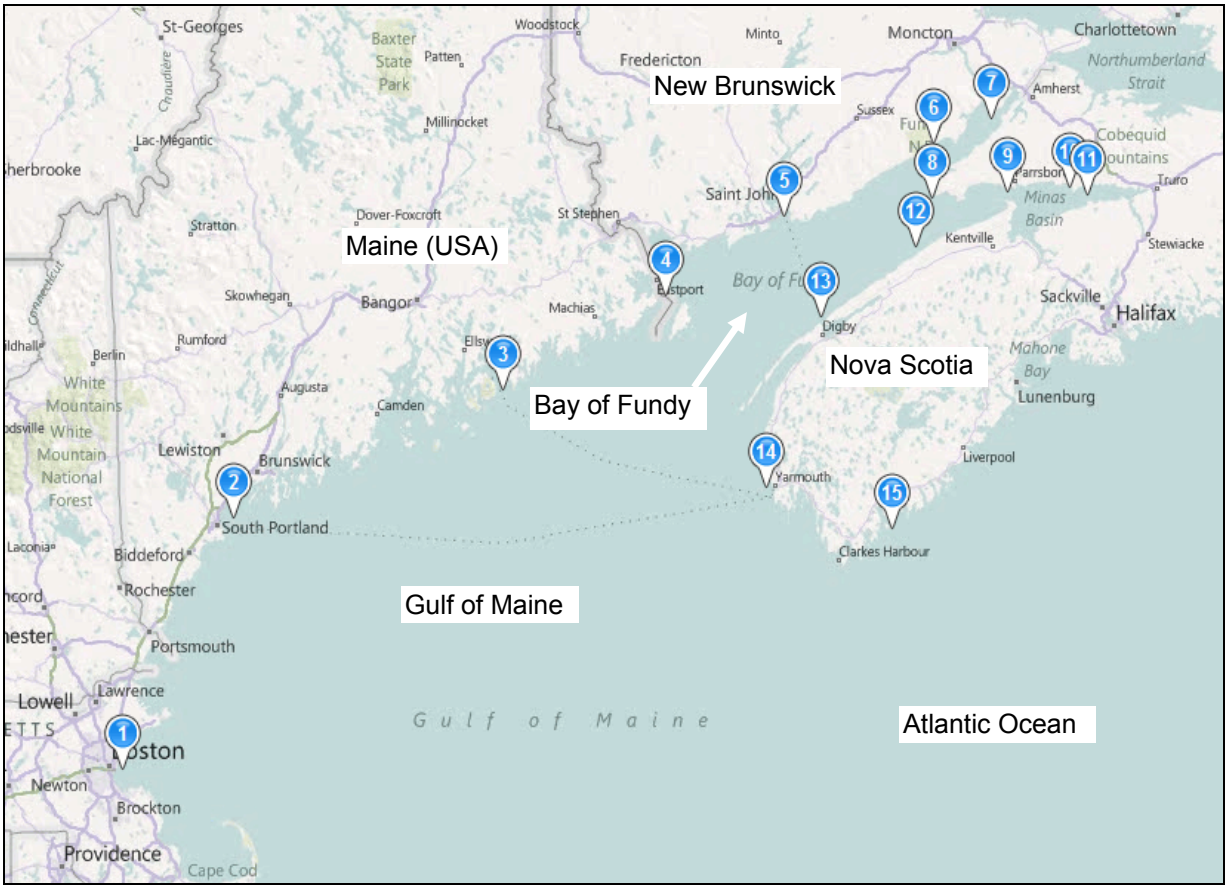

Figure 1. Gulf of Maine and Bay of Fundy, with reference stations 1-15.

Figure 2. Maximum tide range in the upper Bay of Fundy.

The Fundy tides are semi-diurnal; twice each day roughly 115 billion tonnes of seawater flow in and out of the 255 km long Bay. The tidal amplitude near Burntcoat Head, located in Minas Basin, can exceed 8.4 m during spring tide. The natural geometry and bathymetry of the BoF are the main factors responsible for producing the extraordinarily large tides. The BoF, together with Gulf of Maine (GoM), form a funnel with a natural period of approximately 13 hours, close to the 12.42 hour period of the dominant M_2 tidal forcing. The large tides are a result of the near-resonant response of the BoF-GoM system to the M_2 tidal forcing [15].

1.1 Tidal Lagoon Concept

There are two main methods of extracting energy from the tides: either by harnessing the fluctuations in potential energy associated with the rise and fall of the sea level; or by exploiting the kinetic energy associated with the tidal-driven water flows. While tidal power technology is constantly evolving, today's technologies can be grouped into three main categories.

- In-stream devices extract kinetic energy from flowing water to power isolated turbines, in a similar way as windmills are powered by air currents. Since seawater is roughly 800 times denser than air, tidal in-stream turbines tend to be smaller than wind turbines, and operate at slower flow speeds.
- Tidal Barrages exploit the difference in water level (head) on two sides of a barrage or dam to generate power by releasing water through low-head turbines installed in a power house. Tidal barrages are essentially dams built across the full width of a tidal estuary, or a river mouth. Although tidal barrages have high efficiency, but they are plagued by high capital costs and undesirable environmental impacts.

- Tidal Lagoons are similar to barrages, but can be constructed as self-contained structures without blocking an estuary or river. Their proponents claim that tidal lagoons couple high efficiency with smaller environmental impacts (compared with a tidal barrage).

Tidal power lagoons are a newer approach to tidal power conversion that attempts to achieve high efficiency while avoiding some of the environmental problems associated with tidal barrages. Tidal Electric Canada LLC (TEC) is proposing to build and operate tidal power lagoons in the upper Bay of Fundy in order to convert the rise and fall of the tides into electrical energy. A typical tidal power lagoon consists of a large impoundment structure (a rubble-mound dyke or caisson) and a power-house containing sluices and conventional low-head hydroelectric generating equipment, situated a mile or more offshore in an area with shallow depths and high tides (offshore lagoon, see Figure 3). A tidal lagoon may also be attached to the shore, so that the shoreline forms a part of the impoundment (coastal lagoon, see Figure 3). Shallow tidal flats with a high tide range provide the most economical sites.

Delta Marine Consultants (DMC) were retained by TEC to assess the feasibility of constructing tidal power lagoons in the upper Bay of Fundy. DMC [11] proposed constructing a tidal lagoon on the tidal flats along the northern shore of Minas Basin between Five Islands and Economy Point. Various plant layouts were investigated by DMC, including lagoons with single and multiple basins and lagoons with direct and rectified flow through the power station. They concluded that a single basin with direct flow through the power station would be most cost efficient for the Minas Basin site. DMC developed conceptual designs for two lagoon types:

- an offshore lagoon comprising a power station and a 12 km^2 circular impoundment enclosed by a 11.9 km long dyke detached from the shore; and
- a coastal lagoon comprising a power station and a 24 km^2 impoundment formed between a 10.2 km long dyke and the existing shoreline (see Figure 4).

a) b)

Figure 3. Artist's renderings: a) offshore lagoon; b) coastal lagoon.

According to DMC [11], a 12 km^2 offshore lagoon fitted with fourteen 7.5 m diameter bulb turbine generators (up to 20 MW each) and 15 sluice gates (56 m^2 area each) would have an average power output of approximately 124 MW. The larger coastal lagoon, equipped with twenty-four 20 MW bulb turbines and 15 sluices, is estimated to have an average power output of approximately 220 MW. Conceptual designs for the rubble-mound impoundment structure, for a turbine caisson and for a sluice caisson are presented in Figure 5 - Figure 7. The sluices are provided to increase the overall efficiency of the power station. They provide the ability to

release additional water from the lagoon at low tide, thereby lowering the water level within the impoundment and increasing the head and the power generated on the following flood tide. Similarly, the sluices can be opened to fill the lagoon at high tide, thereby raising the water level in the lagoon, creating more head for generating greater power on the subsequent ebb tide.

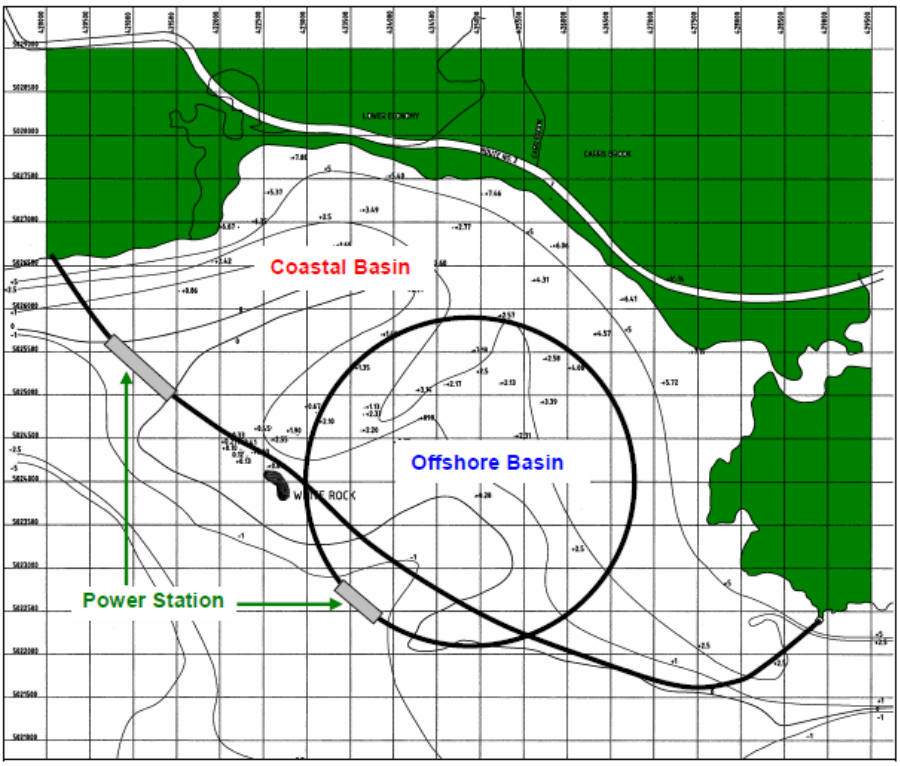

Figure 4. Offshore and coastal lagoons proposed by DMC [11].

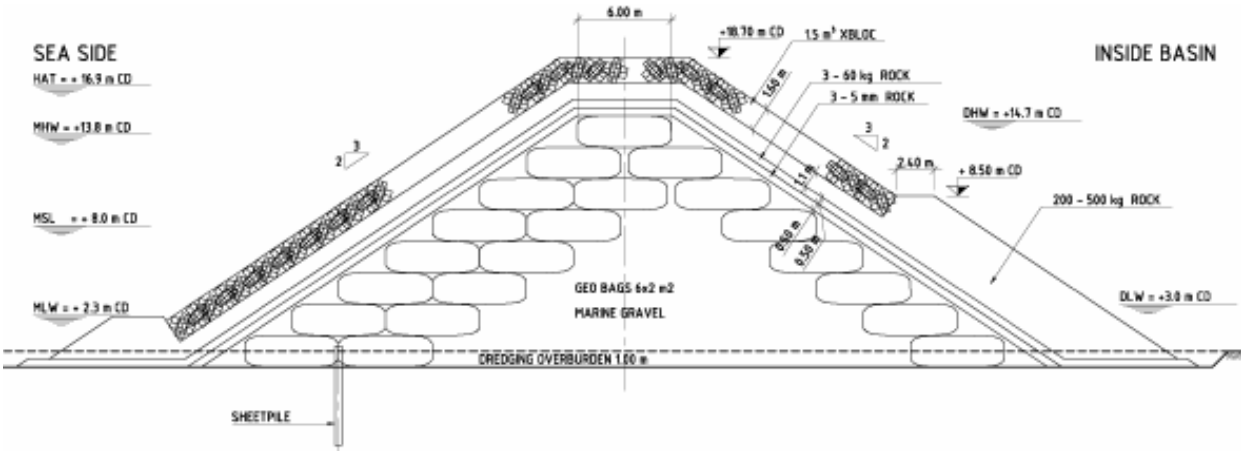

Figure 5. Typical dyke section with geo-bag sand core protected with armour stone and x-bloc units (from [11]).

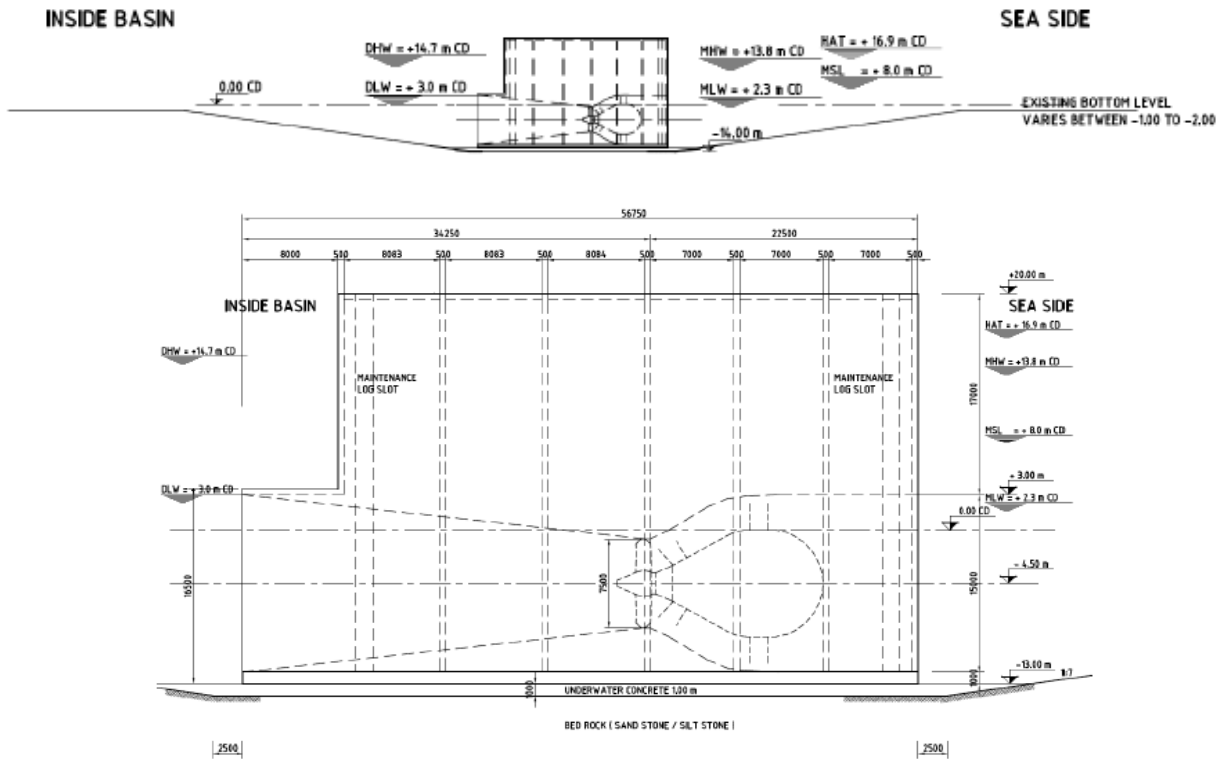

Figure 6. Typical turbine caisson section (from [11]).

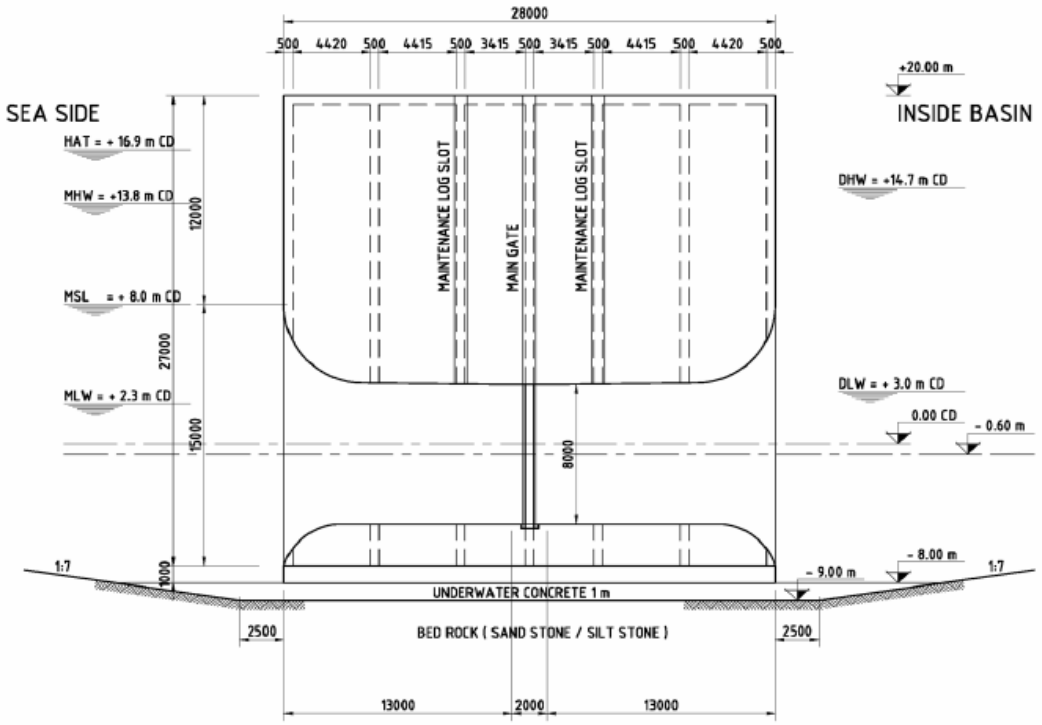

Figure 7. Typical sluice caisson section (from [11]).

1.2 Study Objective

The Gulf of Maine and the Bay of Fundy is one of world's most biologically productive environments. Its marine waters and shoreline habitats host some 2,000 species of plants and animals. Any large tidal power lagoon operating in the upper Bay of Fundy will likely modify the tides and tidal currents near the lagoon, and could perhaps create effects that are felt throughout the entire BoF-GoM region. The nature of these hydrodynamic impacts will likely depend on the size of the tidal lagoon, its location, and its method of operation. Changes to the tidal hydrodynamics may also affect the movement of sediments and alter natural ecosystems that are presently well adapted to existing conditions. The scale and character of the potential hydrodynamic impacts due to tidal lagoons operating in the upper Bay of Fundy have not been previously investigated and remain unknown. The main objective of the present study is to quantify some of these changes. Such information is required to help guide the development of sustainable, science-based policies for the management and development of the tidal energy resources in the Bay.

Previous studies by others (see Section 1.3) have suggested that large tidal barrages located in the upper BoF could have important impacts on the tides and tide-related processes in the BoF and GoM. However, recent studies from the UK suggest a large tidal power lagoon located in the upper Severn Estuary would have "little influence" on the hydrodynamic processes in the Estuary. The potential changes in tidal hydrodynamics due to a single tidal lagoon, or multiple lagoons, operating in the upper BoF have not been previously investigated and remain unknown. This report presents results from a research study undertaken to address this question. The study uses numerical modelling to estimate the changes in tidal hydrodynamics throughout the BoF and GoM that will be caused by several hypothetical development scenarios involving the presence and operation of one or more tidal power lagoons located in the upper part of the Bay of Fundy.

This research was undertaken by the Canadian Hydraulics Centre of the National Research Council (NRC-CHC) in collaboration with the Department of Civil Engineering at the University of Ottawa (uOttawa). The study was funded by the Nova Scotia Associations for Offshore Energy Environmental and Technical Research (OEER/OETR).

1.3 Previous Investigations

Various authors, including [1], [12], [20] and [28] have developed numerical models to simulate tidal hydrodynamics in the GoM and BoF over the years. Greenberg [20] estimated changes in the tidal range throughout the BoF and GoM associated with various proposals to construct large tidal barrages in the upper part of the BoF. Because of the near-resonant state of the existing system, it has been shown that small changes in the geometry of the Bay, associated with the construction of a tidal barrage, could produce significant changes in tidal amplitudes as far away as Boston.

Karsten et al. [28] applied a three dimensional model to investigate the energy that could in theory be extracted from the tidal flows at Minas Passage, a 5.5 km wide channel located at the entrance to Minas Basin in the upper part of the BoF. They showed that the energy that could (in theory) be recovered exceeds the kinetic energy associated with the undisturbed flow through the

Passage by a factor of three or more. They also developed relationships between the amount of energy dissipated at the Passage and the change in the tidal range at various locations throughout the BoF and the GoM.

Cornett et al. [10] developed detailed two- and three-dimensional models of the tidal flows in the BoF and applied these models to delineate and assess the considerable kinetic energy resources around the Bay associated with the energetic tidal currents. The largest kinetic energy resources are found at Minas Passage, a 5 km wide by 12 km long channel located in the upper part of the Bay of Fundy, between Minas Basin and main part of the Bay (see Figure 8). Numerical predictions from [10] of the depth averaged tidal currents in Minas Passage during Spring floods and Spring ebbs are shown below in Figure 9. Figure 10 shows the depth-averaged and time-averaged kinetic power density derived from the modeled tidal flows. Figure 11 shows an example of the vertical profile of the tidal flows in Minas Passage, derived from analysis of ADCP data for a site in the northern part of the Passage. Also shown is the vertical profile of available mean kinetic power density, derived from the velocity data, and a reasonable estimate of the mean power that might be generated by an isolated in-stream turbine deployed at various elevations.

Figure 8. Minas Passage is a 5 km wide channel located in the upper Bay of Fundy at the entrance to Minas Basin (view looking SW).

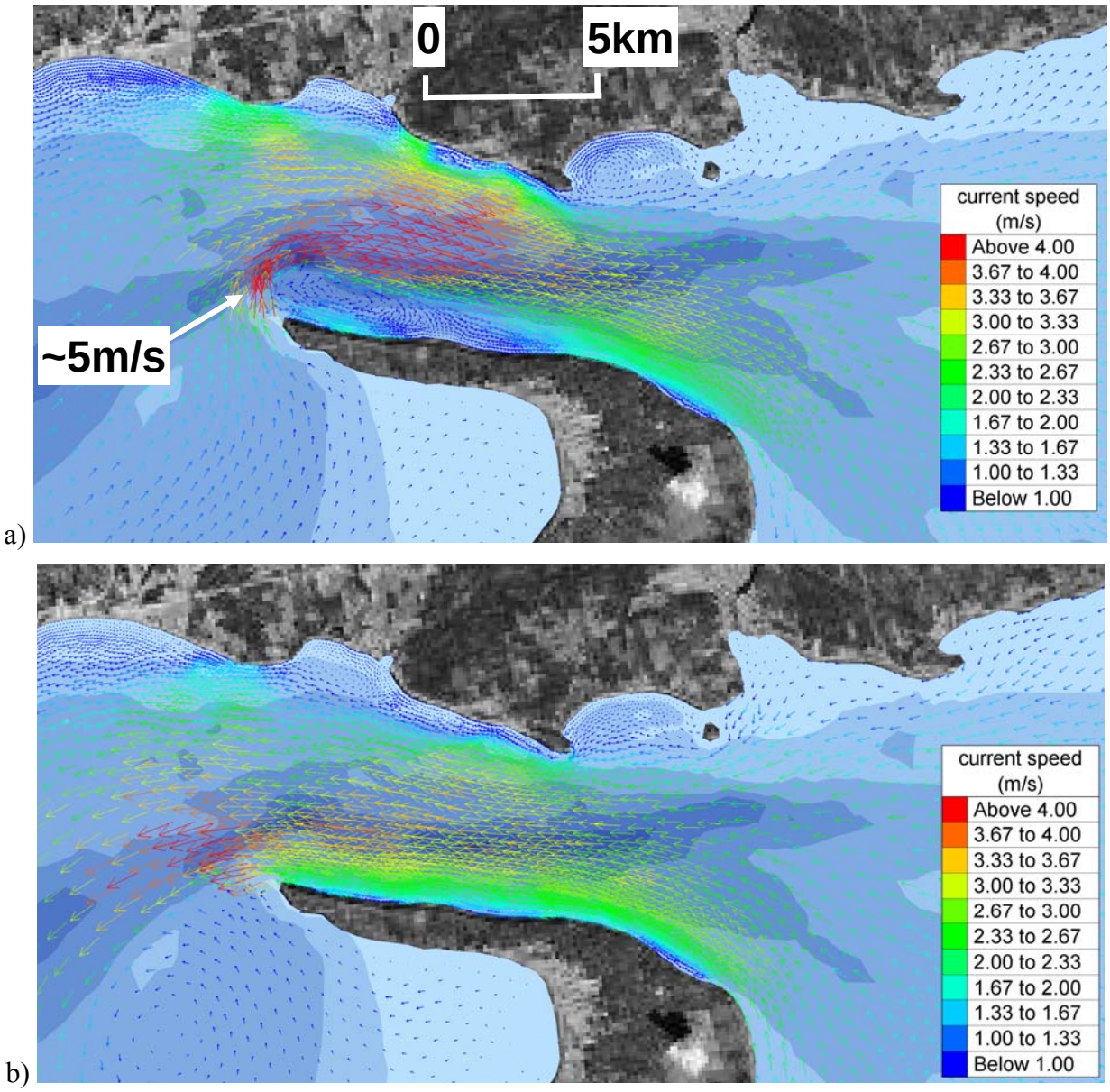

Figure 9. Depth-averaged currents in Minas Passage: a) Spring flood; b) Spring ebb.

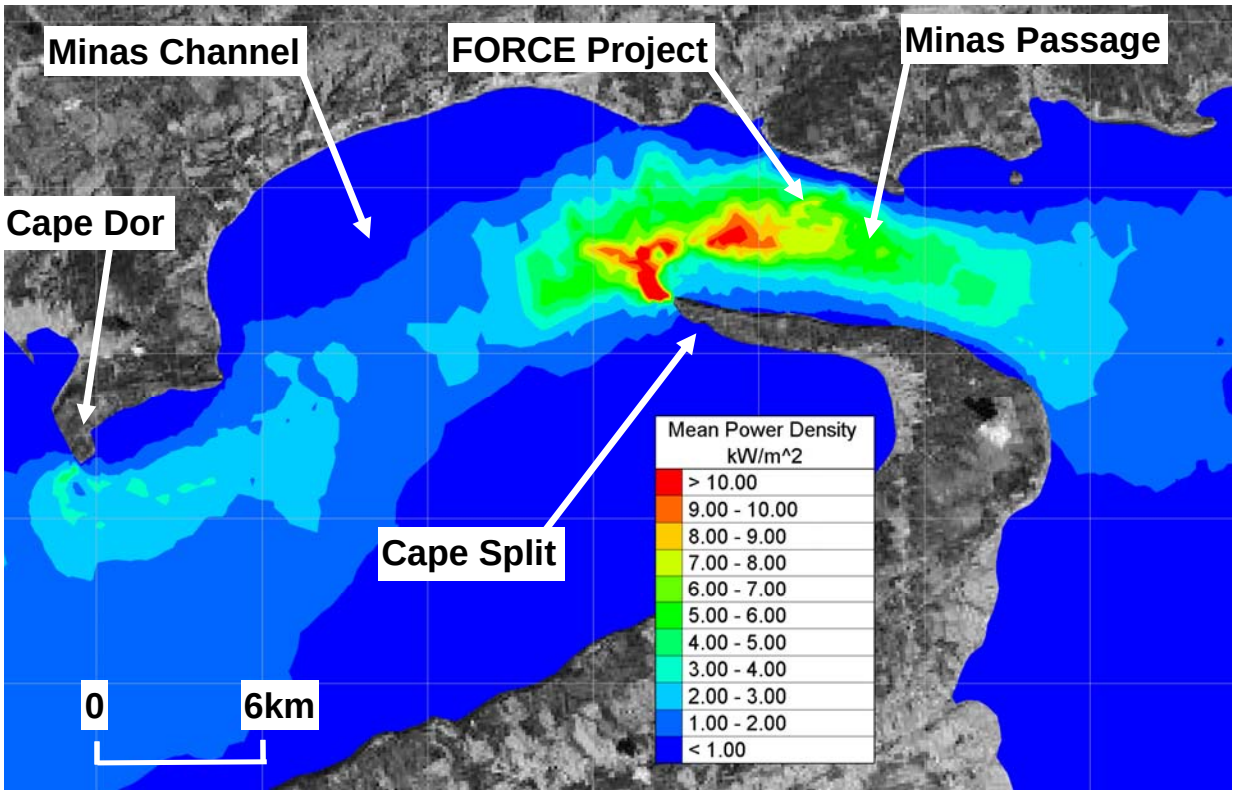

Figure 10. Depth-averaged and time-averaged kinetic power density at Minas Passage.

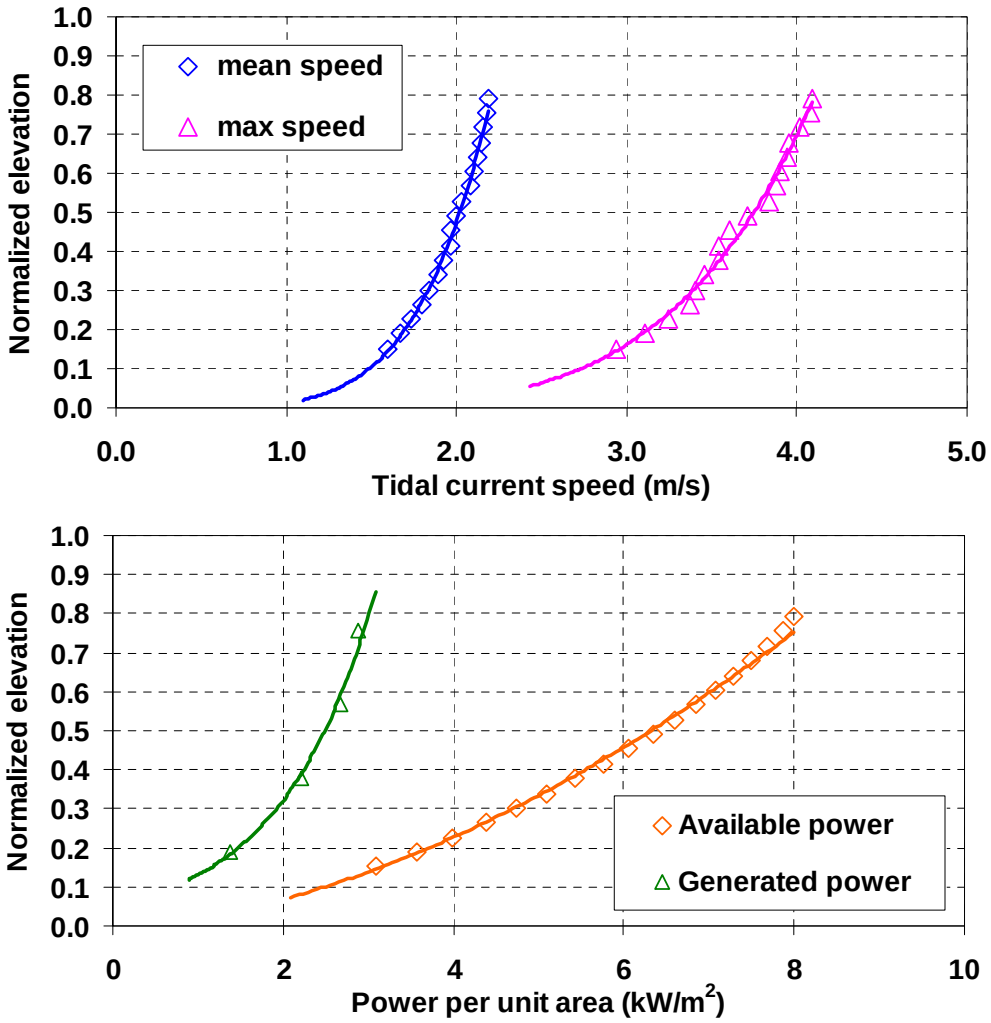

Figure 11. Vertical profile of velocity and kinetic power density for a site in northern Minas Passage.

The Severn Estuary, located between England and Wales, is another ideal site for tidal renewable energy projects, since it has the third highest tidal range in the world, with a spring tide amplitude approaching 7 m. Several studies have been undertaken over the years to investigate the feasibility and impacts of constructing large scale tidal energy projects in this estuary, including several tidal barrages and tidal lagoons. It is worthwhile to consider the results of these studies as they may, by analogy, provide good information on processes and impacts for the Bay of Fundy as well.

Xia, Falconer and Lin [38] have examined the potential hydrodynamic impacts on the Severn Estuary due to several different proposed renewable energy projects, including a large tidal barrage known as the Severn Barrage, and a large coastal lagoon referred to as the Fleming Lagoon. They refined a two-dimensional finite volume numerical model and applied it to forecast the hydrodynamic impacts due to several different power projects. They modelled a

large coastal lagoon (the Fleming Lagoon) with an area of approximately 86 km^2 and an installed capacity of 1,500 MW, and concluded that the lagoon would have "little influence" on the hydrodynamic processes in the Severn Estuary.

Xia, Falconer and Lin [40] examined the impact of constructing a very large tidal barrage across the Severn Estuary (the Severn Barrage). They refined a two-dimensional hydrodynamic model and used the model to simulate the tidal hydrodynamics with and without the barrage. They concluded that discharges, water levels, and tidal currents would all decrease significantly above the barrage. In [39] these same authors discuss the influence of alternative operating modes on the hydrodynamic impacts of the Severn Barrage. After considering various factors, they conclude that, for efficient electricity generation and reduced flood risk, ebb-generation or bi-directional generation are preferred over flood-generation.

Figure 12 - Figure 16 are borrowed from [38] and are reproduced here for easy reference. Figure 12 shows a map of the Severn Estuary, including the locations of the proposed Severn Barrage and Fleming Lagoon. The depths throughout the estuary are shown in Figure 13. The numerical representation of the Fleming Lagoon, using triangular elements, is shown in Figure 14. Xia et al. defined two non-overlapping numerical sub-domains, one within the lagoon and the other outside the lagoon, and used pairs of sources and sinks to exchange seawater between the two sub-domains, simulating the flows through turbines and sluices. Figure 15 shows the numerical flow field around the lagoon at two distinct times, one during the ebb, and the other during the flood tide. During the flood, water enters the lagoon through the sluices located on either side of the powerhouse; while during the ebb, water exits the lagoon through the turbines located at the centre of the numerical powerhouse. Figure 16 shows the maximum water level predicted by Xia et al. for a) existing conditions; b) with the Severn Barrage; and c) with the Fleming Lagoon. It can be seen that the changes in water level are much greater for the Severn Barrage than for the Fleming Lagoon. Finally, Figure 17 compares the maximum depth-averaged velocity predicted by Xia et al. for the three cases (existing conditions, Severn Barrage, Fleming Lagoon). These results clearly show that the changes in maximum velocity due to the Fleming Lagoon are generally smaller than the changes due to the Severn Barrage. These results suggest that the hydrodynamic impacts of the Fleming Lagoon, while considerably smaller than those of the Severn Barrage, are certainly not negligible. While both large scale tidal energy schemes (Severn Barrage and Fleming Lagoon) will modify the tidal hydrodynamics in the estuary, the changes due to the Fleming Lagoon are generally smaller than those due to the Severn Barrage.

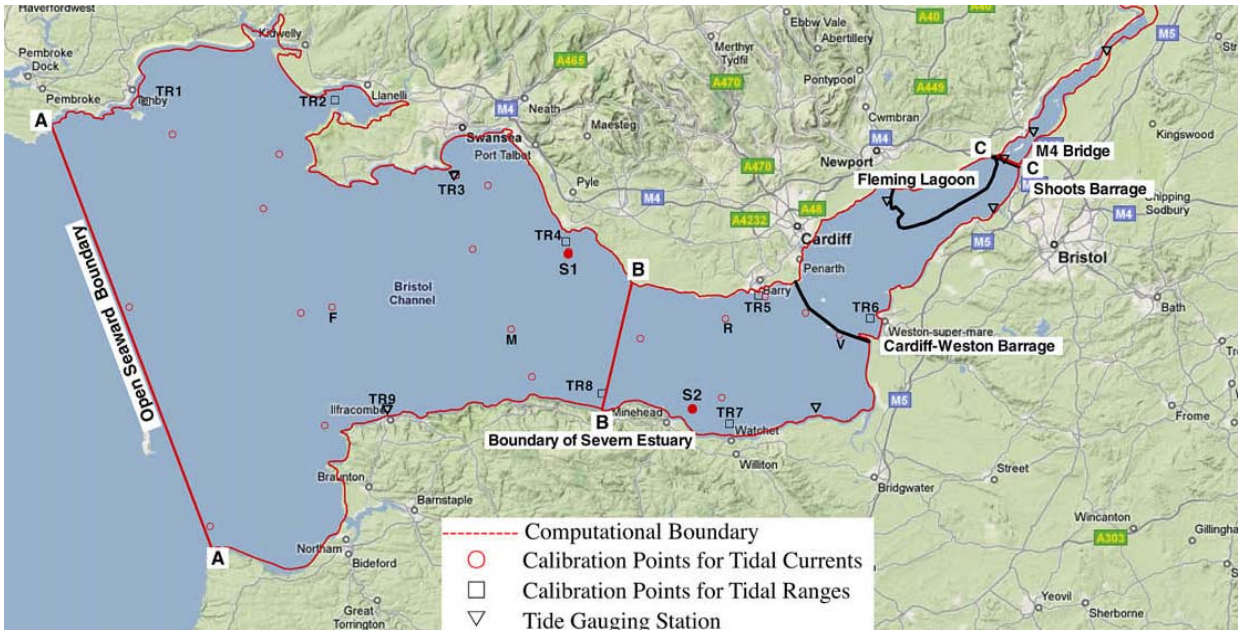

Figure 12. Map of the Severn Estuary showing the location of the Fleming Lagoon and the Cardiff-Weston (Severn) Barrage.

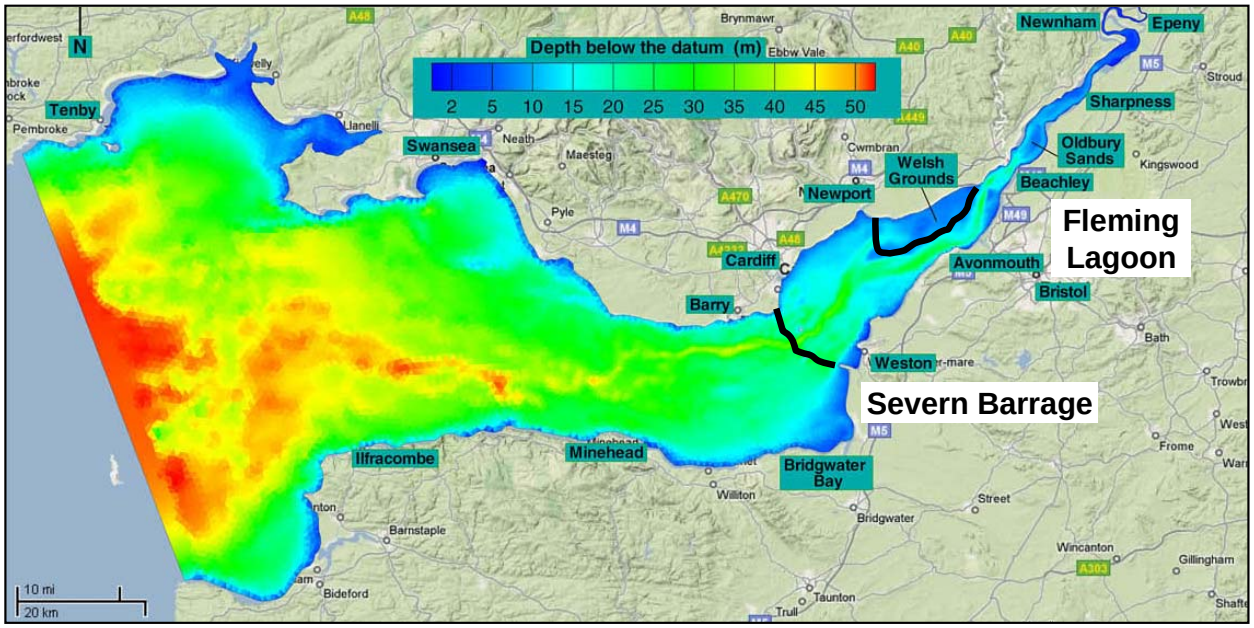

Figure 13. Severn Estuary bathymetry with the Severn Barrage and the Fleming Lagoon (Xia et al., 2010).

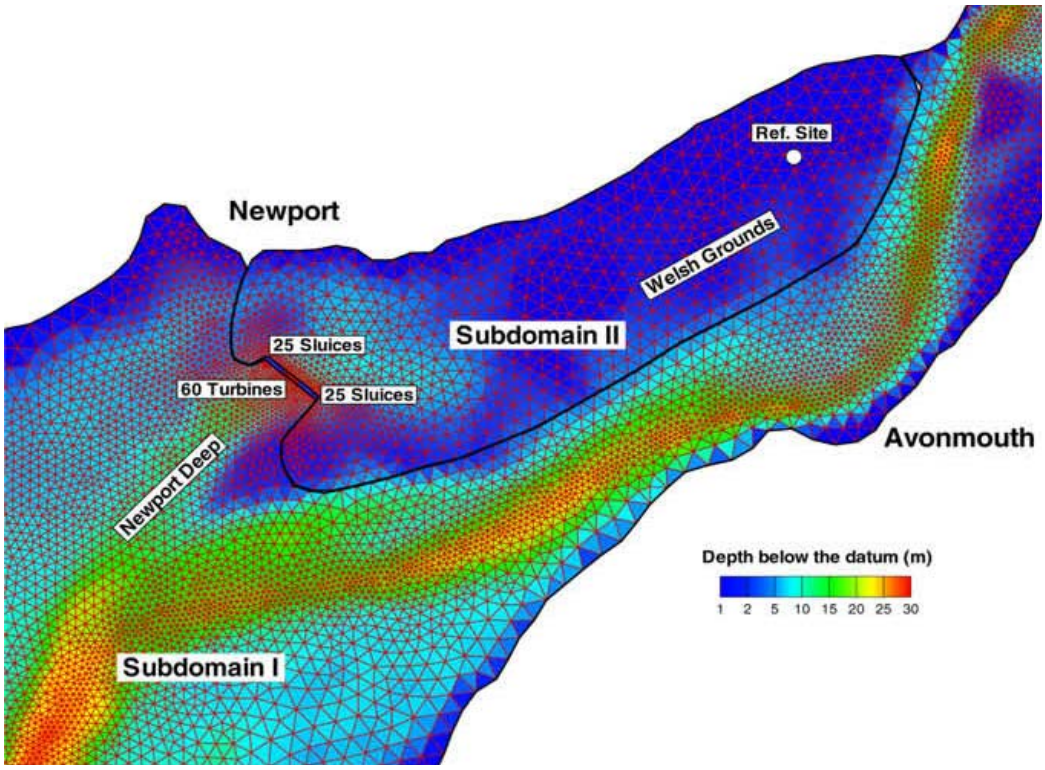

Figure 14. Representation of the Fleming Lagoon in the numerical model (Xia et al., 2010).

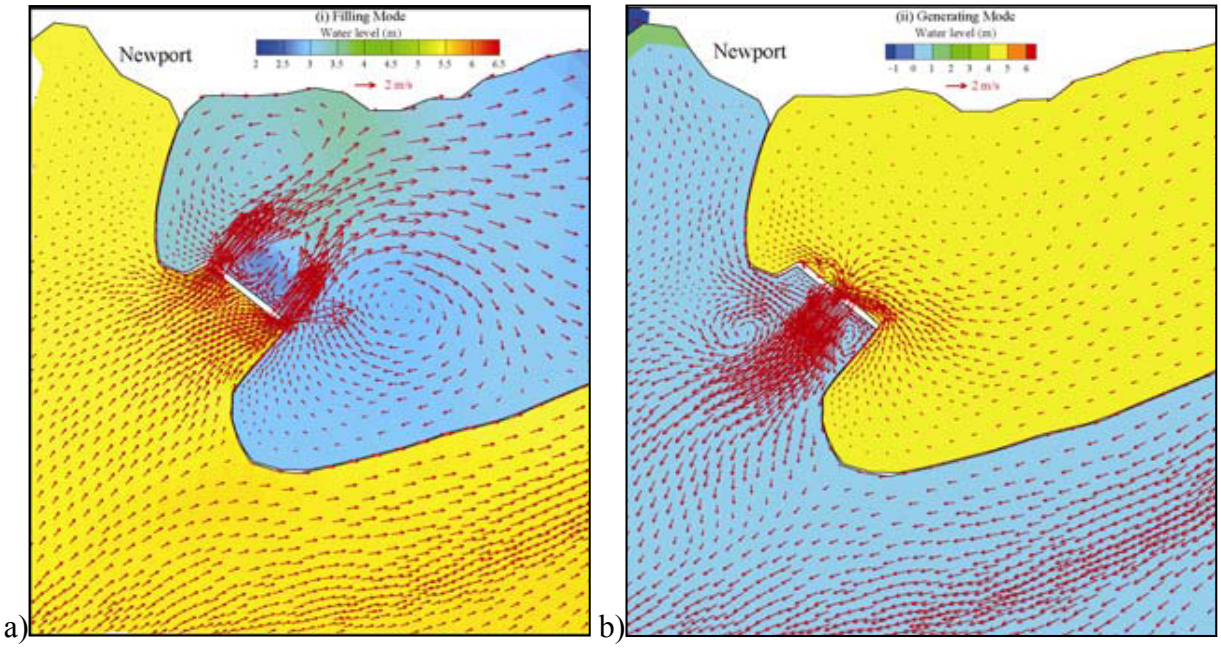

a) b)

Figure 15. Numerical simulation of flows near the power house during: a) flood; b) ebb (Xia et al., 2010).

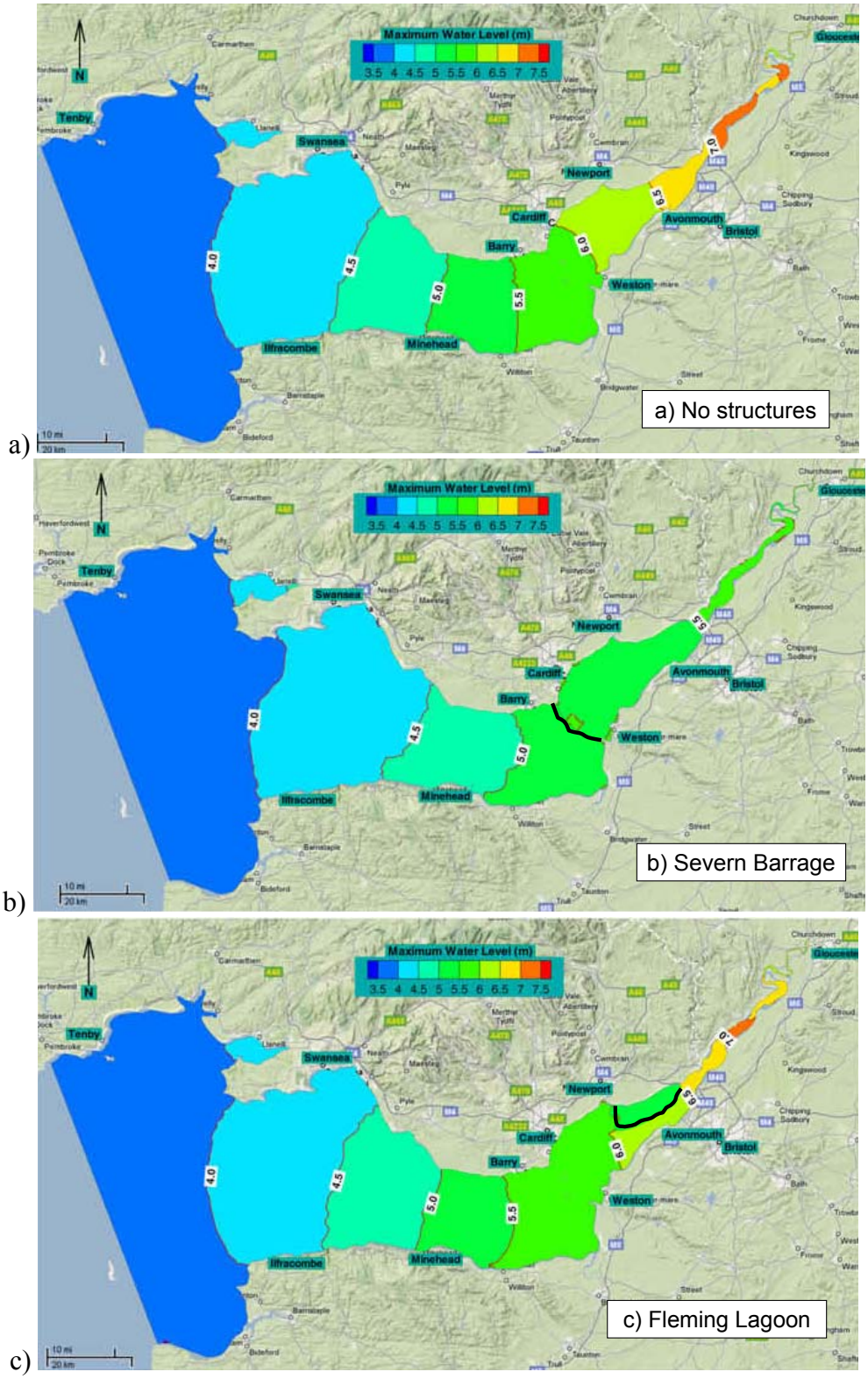

Figure 16. Numerical prediction of maximum water level: a) for existing conditions; b) with the Severn Barrage; c) with the Fleming Lagoon (Xia et al., 2010).

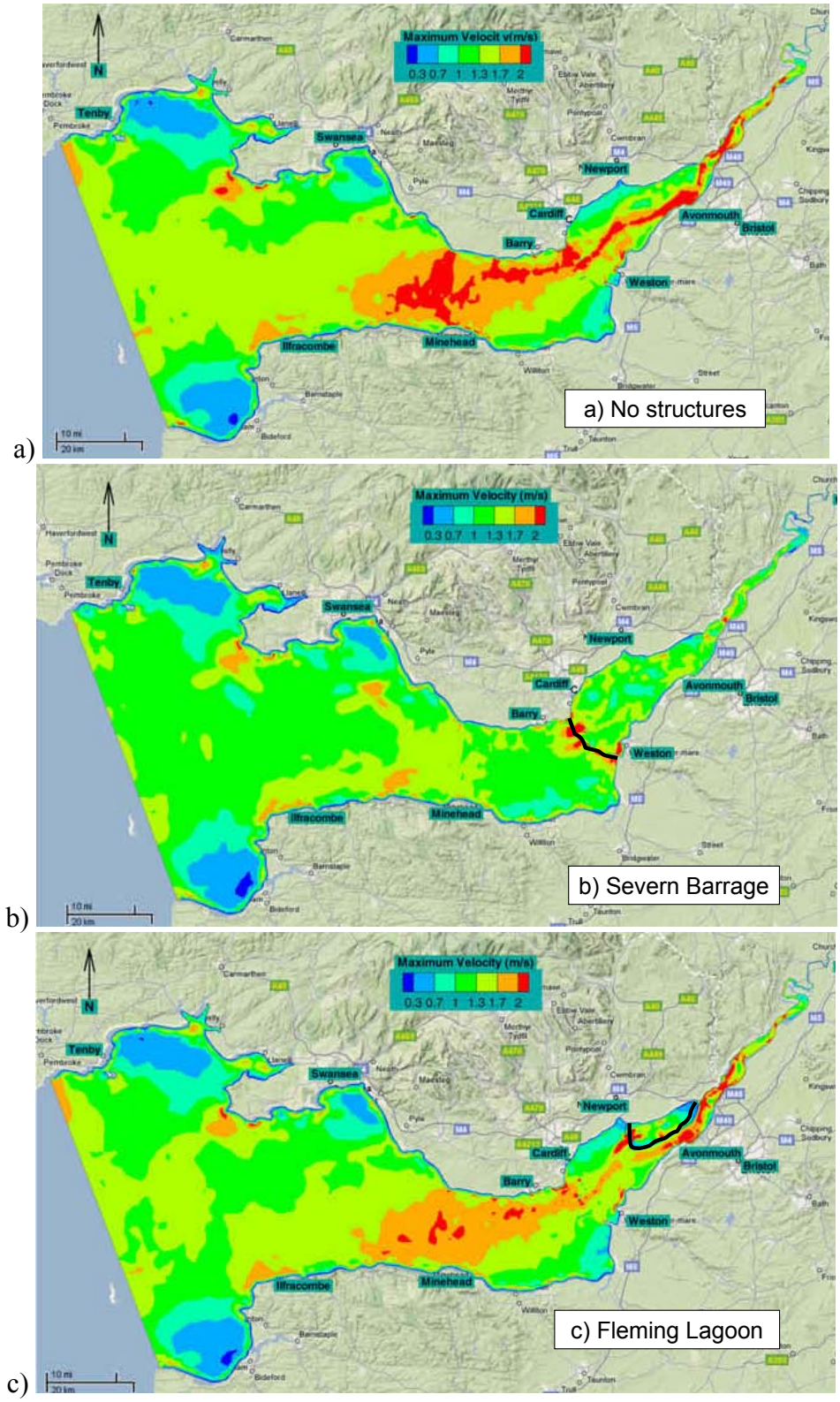

Figure 17. Numerical prediction of maximum velocity: a) for existing conditions; b) with the Severn Barrage; c) with the Fleming Lagoon (Xia et al., 2010).

2 Model Development and Calibration

2.1 Model Development

In this study, tidal hydrodynamics in the BoF and GoM have been simulated using a two-dimensional (depth averaged) numerical model based on the TELEMAC modelling system, developed by Electricité de France [24]. Most phenomena of importance in free-surface flows can be included in this model, such as the friction on the bed and lateral boundaries, wind stress on the free surface, Coriolis force, turbulence, and density effects. The dynamic wetting and drying of the tidal flats influences the tidal hydrodynamics in the upper part of the Bay, and these processes were included in the TELEMAC-2D simulations.

TELEMAC-2D employs finite-element methods to solve the Saint-Venant equations over a computational domain subject to initial conditions and boundary conditions. Since the computational domain is represented by a flexible unstructured triangular mesh, a higher spatial resolution can be used in areas of special interest and where spatial gradients are large (i.e., near shorelines), while a lower resolution can be used in areas of lesser interest. The Saint-Venant equations can be written as:

$$\frac{\partial h}{\partial t} + u \cdot \vec{\nabla}(h) + h \cdot div(\vec{u}) = S_h \tag{1}$$

$$\frac{\partial u}{\partial t} + \vec{u} \cdot \vec{\nabla}(u) = -g \frac{\partial Z}{\partial x} + S_x + \frac{1}{h} \cdot div\left(h v_t \vec{\nabla} u\right) \tag{2}$$

$$\frac{\partial v}{\partial t} + \vec{u} \cdot \vec{\nabla}(v) = -g \frac{\partial Z}{\partial y} + S_y + \frac{1}{h} \cdot div\left(h v_t \vec{\nabla} v\right) \tag{3}$$

where h = total water depth; x, y = horizontal space coordinates; u, v = depth-averaged velocities in x, y direction, respectively; g = gravitational acceleration; v_t = momentum coefficients; Z = free surface water elevation; t = time; S_h, S_x and S_y = source term including: bed friction, bed slope and the Coriolis force.

The effects of bed friction, Coriolis force, and turbulence were all included in the model. Large eddy simulation (LES) was used to simulate turbulent flows. This technique allows one to explicitly solve for the large eddies in a calculation and implicitly account for the small eddies by using a subgrid-scale model (SGS model). The SGS model used in this study was the Smagorinsky model as described in [34].

The Coriolis effect refers to a deflection of moving objects when they are viewed in a rotating frame of reference, such as the Earth. The effect is caused by the rotation of the Earth and the inertia of the mass experiencing the effect. Because the Earth completes only one rotation per day, the Coriolis force is quite small, and its effects generally become noticeable only for motions occurring over large distances and long periods of time, such as large-scale movement of water in the ocean. This force causes moving objects on the surface of the Earth, including air in the atmosphere and water in the oceans, to appear to veer to the right in the northern hemisphere, and to the left in the southern. Rather than flowing directly from A to B, as they would on a non-rotating planet, currents tend to flow to the right of this direction north of the equator, and to the left of this direction south of it.

The bed friction was implemented through Strickler's equation:

$$F_x = -\frac{1}{\cos\theta}\frac{g}{h^{4/3}K^2}\sqrt{u^2+v^2}u \quad (4)$$

$$F_y = -\frac{1}{\cos\theta}\frac{g}{h^{4/3}K^2}\sqrt{u^2+v^2}v \quad (5)$$

where F_x and F_y are the components of the friction force on the bottom in the x and y directions; θ is the bottom slope, h is the depth, g is the acceleration due to gravity; K is the Strickler friction coefficient, and (u, v) are the components of velocity in the x and y directions.

The wetting and drying of inter-tidal flats was also included in the modelling. Linear interpolation is used to calculate the free surface slope where there are semi-wet elements.

2.2 Model Grids

The model domain includes the entire Bay of Fundy and Gulf of Maine. The offshore boundary was set beyond the edge of the continental shelf so that the model could be used to assess the hydrodynamic impacts along the entire GoM-BoF coastline.

Several different unstructured model grids were developed for this study, representing both existing conditions without lagoons and hypothetical future conditions with between one and six power lagoons operating in the upper part of the Bay. The specific development scenarios that were modelled are considered further in Section 4. The computational domain spans a 235,289 km^2 area extending from Providence, Rhode Island, to Halifax, Nova Scotia, and it includes the Bay of Fundy and the entire Gulf of Maine (see Figure 18). In general, smaller elements were used to provide a higher resolution in shallow coastal areas and in the upper Bay of Fundy, while coarser elements were used further away from the coast. Finer elements were also generated along the continental shelf to accurately reflect the bathymetric variability in this region. The grid of existing conditions consists of 108,993 nodes and 205,148 triangular elements varying in size from 50 m to 10 km (see Figure 19).

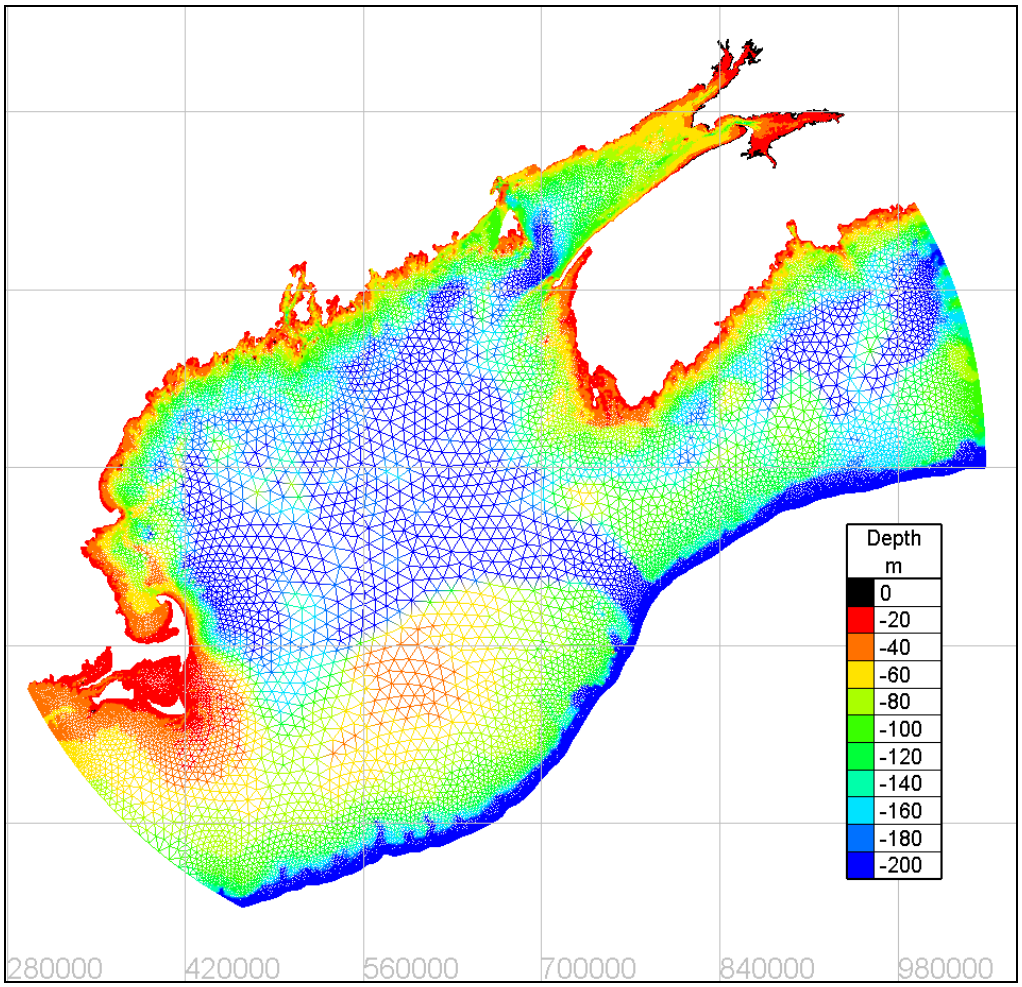

Figure 18. Model domain, finite element mesh and bathymetry.

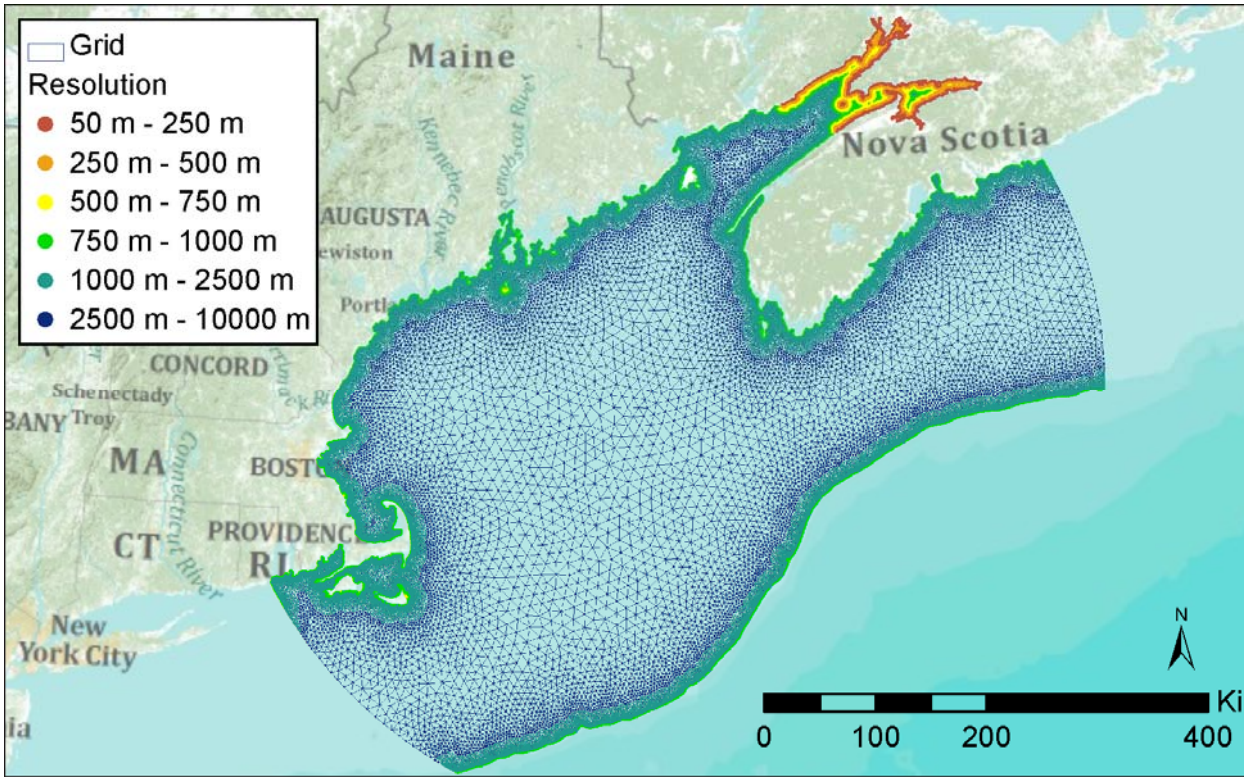

Figure 19. Model mesh and variable grid resolution.

The elevation of the seabed was specified at each node. The inter-tidal areas up to the highest astronomical tide (HAT) shoreline were included in the model domain. The depths/elevations were derived from an integration of data from the following sources:

1. Geobase Canadian Digital Elevation Data,
2. USGS National Elevation Dataset,
3. CHS Multibeam Bathymetry,
4. CHS Nautical Charts,
5. NOAA Soundings and Electronic Navigational Charts, and
6. BODC Gridded Bathymetric Chart of the Oceans.

The spatial coverage of the various datasets is shown in Figure 20. The first two datasets were used to define the elevations within the intertidal zone. Sources (3), (4) and (5) cover the GoM, the BoF and the Nova Scotian continental shelf. Deep ocean areas not covered by datasets (1) – (5) were populated with the BODC bathymetric dataset. The six datasets were originally referenced to different tidal datums and were adjusted to Universal Transverse Mercator North American Datum (NAD) 83 (Zone 19) coordinates in the horizontal plane and referenced to North American Vertical Datum of 1988 (NAVD 88) in the vertical plane.

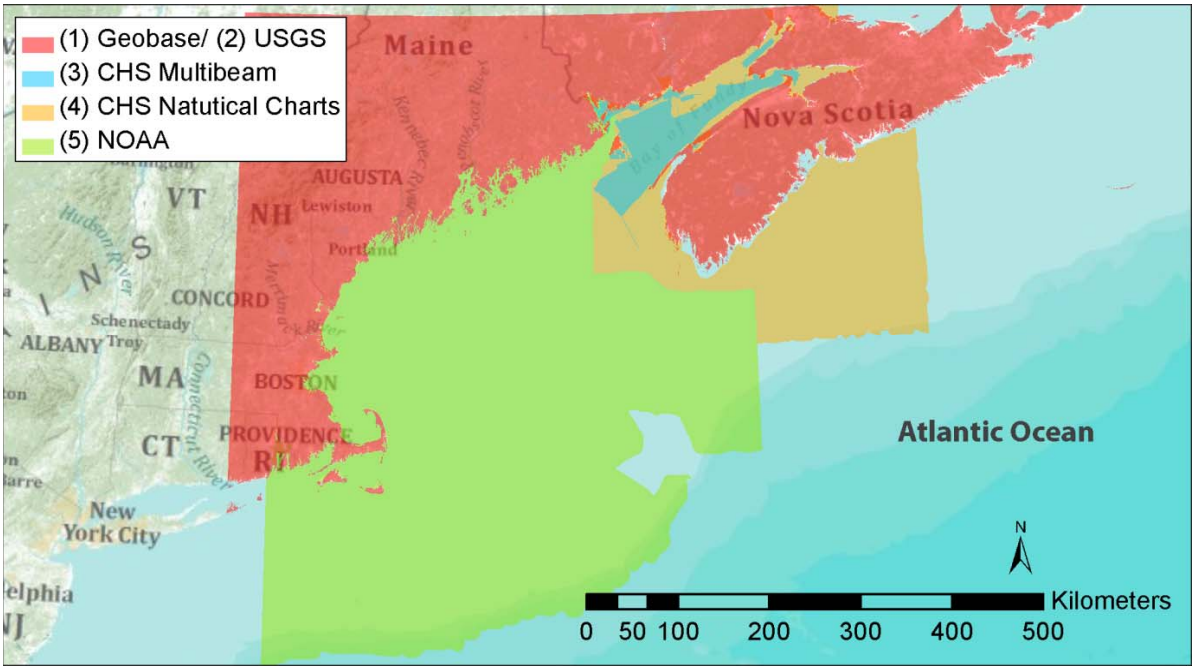

Figure 20. Spatial coverage of bathymetric data sets.

2.3 Boundary conditions

Many previous researchers considered only the M_2 tidal constituent when studying the hydrodynamic impacts due to tidal power projects in the Bay of Fundy ([19], [20], [22], [23], [24], [28], [29]). The M_2 constituent is certainly dominant and contributes over 80% of the total tidal energy in the upper Bay. However, in order to achieve better accuracy, other constituents must be included as well.

The tidal flows due to the M_2 constituent and nine other leading constituents have been considered in the present study. Sea surface elevations and initial depth-averaged currents were interpolated along the open ocean boundary using harmonic constants for ten leading constituents (M_2, N_2, S_2, K_1, O_1, K_2, L_2, $2N_2$, NU_2, M_4). The boundary conditions were calculated from model results produced by a depth-integrated finite-element tidal circulation model developed by Dupont et al. [12] . This 2D tidal model has a domain covering the Gulf of Maine, the Bay of Fundy and part of the Scotian Shelf, and assimilates tidal constituents derived from sea level observations made by the TOPEX-Poseidon altimeter. According to [12], the nine constituents, excluding M_4, account for 88% of the sum of the amplitudes of the 67 official tidal constituents at Saint John.

Freshwater inflows from rivers are insignificant relative to the tidal flows, and were ignored in the present study.

2.4 Model Calibration

The new model was calibrated by adjusting the bottom roughness in different parts of the domain to minimize the error in tide range and time-of-tide between the model's predictions and water

level time histories for 142 NOAA/DFO tidal stations distributed throughout the domain. For each tidal station, model results were compared to predictions synthesized from harmonic constants established by DFO and NOAA. The same set of 10 constituents (M_2, N_2, S_2, K_1, O_1, K_2, L_2, $2N_2$, NU_2, M_4) used to drive the numerical model were also used to generate the target water level time histories for each tidal station. During the initial calibration, tides were simulated for a 7-day period. The model was first calibrated for the M_2 tidal constituent alone, and then for all 10 constituents combined together. The Strickler roughness coefficient for different areas was adjusted over the range from 20 to 40 in order to minimize calibration errors throughout the domain. The characteristics of the seabed were taken into consideration when selecting the bottom roughness coefficient for each area.

A sensitivity analysis was conducted to determine the optimal time step for these simulations. It was concluded that a model time step of 10 seconds was sufficient to ensure numerical stability.

Tides were simulated for a 7-day period during the calibration process. Once successfully calibrated, the model was validated by predicting the tides over three different 28-day periods, each including two full spring-neap tidal cycles. The calibration and validation periods are summarized below in Table 1.

Figure 21 shows two examples of the good agreement obtained between the modelled tide and the astronomical tide predication at most stations. It can be seen that both the minimum and maximum water levels, as well as their timing, are predicted with good precision. Table 2 summarizes the validation errors for the fifteen reference stations mapped in Figure 1. The error (e) in water level is calculated as:

$$e = \frac{\eta_m - \eta_o}{\eta_o} \tag{6}$$

where η_m is the modelled water level and η_o is the observed water level.

Simulation period	Calibration	Validation
10/08/2007 00:00 - 17/08/2007 00:00	C1	
17/08/2007 00:00 - 14/09/2007 00:00		V1
07/01/2009 00:00 - 04/02/2009 00:00		V2
17/07/2009 00:00 - 15/08/2009 00:00		V3

Table 1. Summury of time periods used for model calibration and validation.

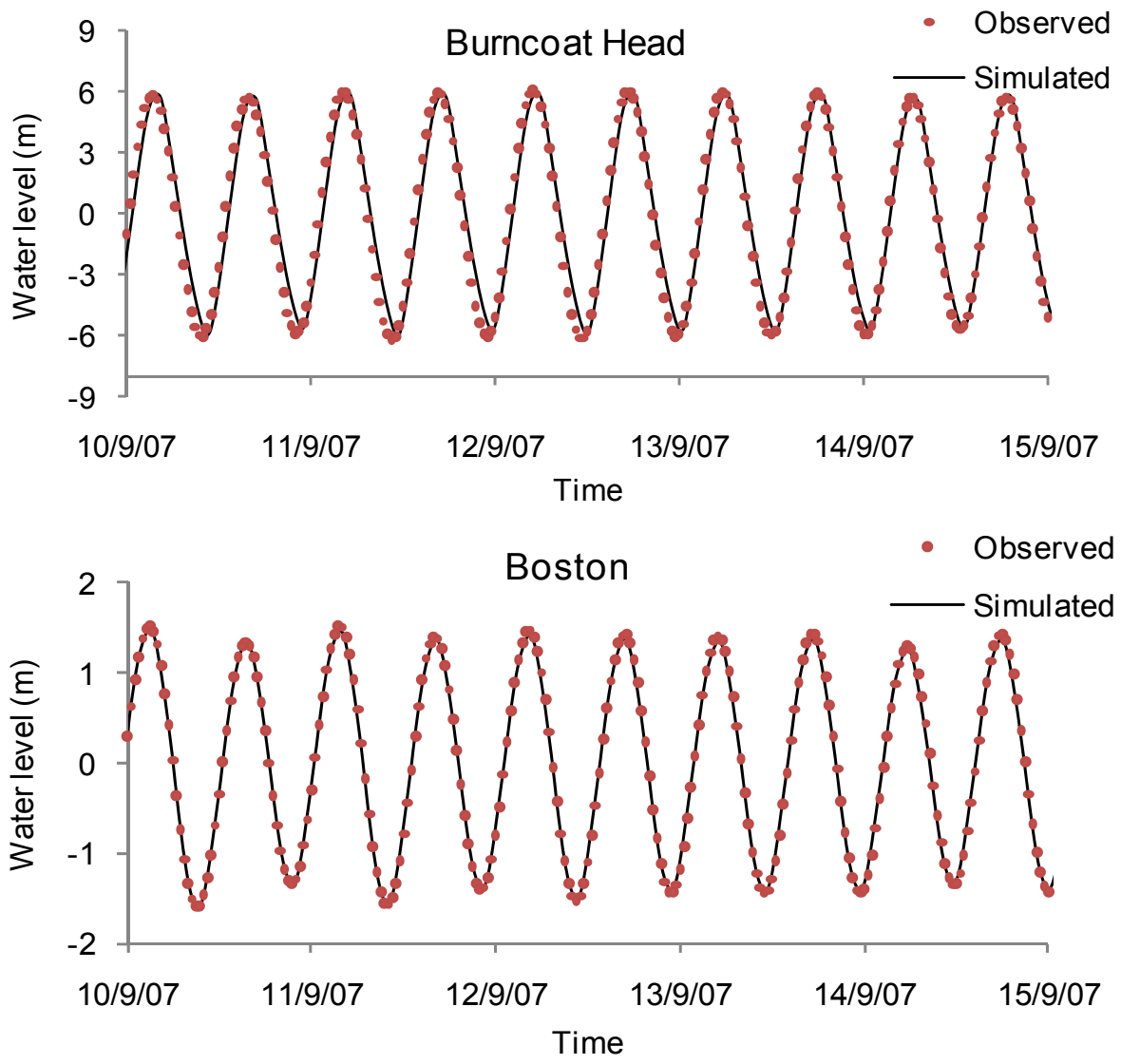

Figure 21. Simulated and observed water levels for September 2007.

The depth-averaged tidal currents predicted by the model were also compared with available ADCP data for several sites in Minas Passage and Minas Basin. The ADCP data is collected and archived by Fisheries and Oceans Canada (DFO) and the datasets that were consulted in this study are summarized in Table 3. Each dataset contains velocity measurements at discrete intervals for various elevations above the seabed. Since the numerical model computed a single depth-averaged velocity at each node, the ADCP data was first analysed to obtain a depth-averaged velocity from the measured velocity profile. The agreement between the measured and modelled currents was generally satisfactory; an example is presented in Figure 22. The small discrepancies between the measured and modeled velocities are likely due to a number of factors, including:

- Measurement errors;

- Errors in estimating depth-averaged velocity from ADCP data;
- Numerical model based on only 10 tidal constituents;
- Finite spatial and temporal resolution of the numerical model;
- Approximate numerical representation of bathymetry;
- Approximate numerical representation of turbulence; and
- Measurements could include currents from non-tidal sources (storm surges, waves).

				High tide		Low tide	
No.	Station	Lat	Long	RMS error in height	RMS phase difference	RMS error in height	RMS phase difference
		deg	deg	(%)	(min)	(%)	(min)
1	Boston	42.36	-71.05	3.70%	11	3.72%	9
2	Portland	43.66	-70.25	2.94%	10	2.58%	18
3	Bar Harbor	44.39	-68.21	5.15%	12	6.55%	11
4	South Lubec	44.87	-66.98	4.24%	14	5.17%	11
5	Saint John	45.27	-66.07	6.98%	15	8.49%	13
6	Herring Cove	45.57	-64.97	7.78%	19	7.43%	20
7	Chignecto	45.48	-64.98	6.88%	18	6.20%	20
8	Cape D'or	45.28	-64.77	9.29%	15	3.50%	17
9	Diligent River	45.40	-64.42	7.46%	19	6.53%	15
10	Five Islands	45.38	-64.07	7.43%	17	6.82%	17
11	Burntcoat Head	45.30	-63.80	7.22%	22	6.41%	30
12	Hantsport	45.07	-64.17	7.35%	21	6.57%	24
13	Digby	44.63	-65.75	9.70%	13	10.11%	13
14	Yarmouth	43.83	-66.12	4.98%	17	3.30%	13
15	Shelburne	43.75	-65.30	4.66%	11	5.09%	17

Table 2. Summary of validation errors for reference stations 1-15.

Based on these results, it was concluded that the calibrated model is able to predict tidal fluctuations throughout the Bay of Fundy and Gulf of Maine with good accuracy. The model was deemed sufficiently accurate to investigate the changes in tidal hydrodynamics due to tidal power lagoons.

ID	Longitude	Latitude	Start	End
1658	-64.40383	45.35648	17/08/2007 19:15	28/08/2007 14:30
1659	-64.40335	45.35615	28/08/2007 16:30	14/09/2007 16:45
1708	-64.40330	45.35760	07/01/2009 14:43	07/02/2009 15:00
1709	-64.42103	45.33210	07/01/2009 15:19	20/02/2009 00:00
1710	-64.32438	45.33525	07/01/2009 14:16	12/02/2009 06:46
1711	-64.33605	45.31007	07/01/2009 13:52	15/02/2009 14:14
1715	-64.25802	45.24182	28/01/2009 14:35	18/02/2009 10:14
1737	-64.25968	45.24060	17/07/2009 11:57	27/08/2009 10:50
1738	-64.29440	45.24967	17/07/2009 12:12	27/08/2009 11:19
1739	-64.47642	45.33508	17/07/2009 13:22	23/08/2009 13:00
1740	-64.47026	45.35777	17/07/2009 13:48	14/08/2009 13:49

Table 3. Summary of ADCP datasets consulted for model validation.

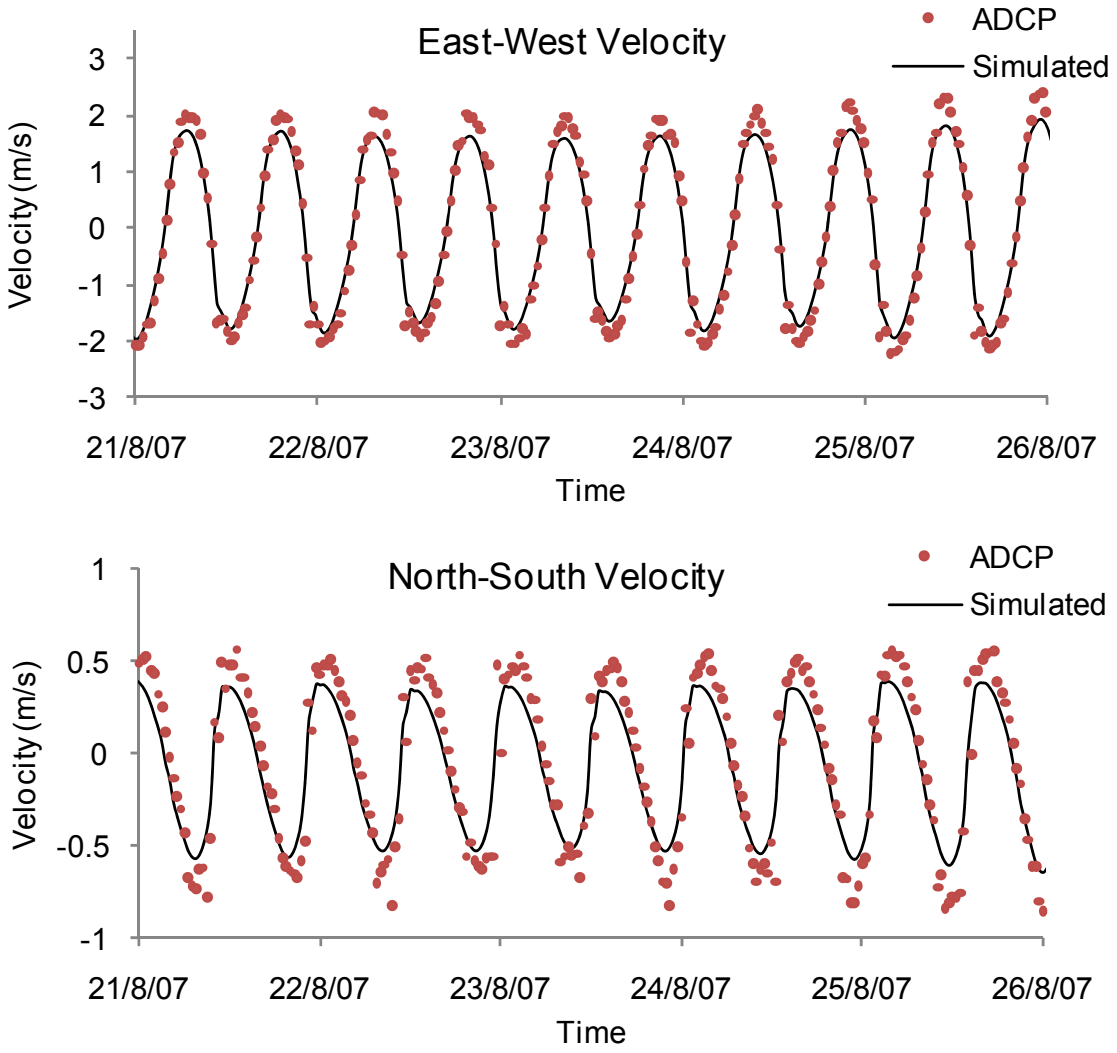

Figure 22. Simulated and observed depth-averaged velocity for a site in Minas Basin.

3 Numerical Simulation of Tidal Power Lagoons

In addition to the grid of existing conditions, thirteen other grids have been developed to represent various hypothetical scenarios including one or more tidal lagoons. The lagoons are modelled by refining the mesh locally to a resolution of 50 m along the impoundment dyke and around the powerhouse (see Figure 23). The mesh is only refined near the lagoon and remains unchanged away from the lagoon. The dyke and powerhouse are idealized in the model as vertical sided structures having a width of 50 m. Following Xia et al. [38], the interior of the lagoon is modelled as a sub-domain that is disconnected from the main domain outside the lagoon. Multiple pairs or sources and sinks are defined to transfer seawater between the two domains, simulating the flows through the sluices and turbines within the powerhouse. For each lagoon layout, the powerhouse was assumed to have turbines located centrally between the sluices as shown in Figure 24.

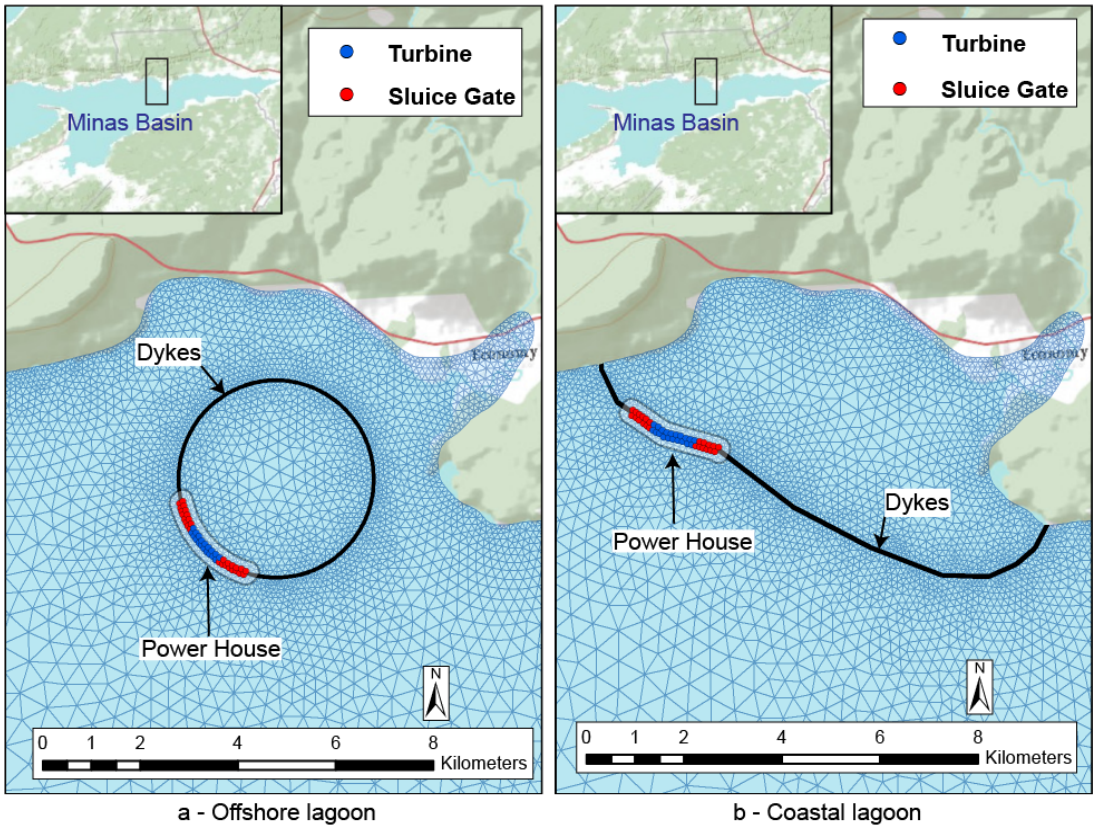

Figure 23. Numerical representation of tidal power lagoons.

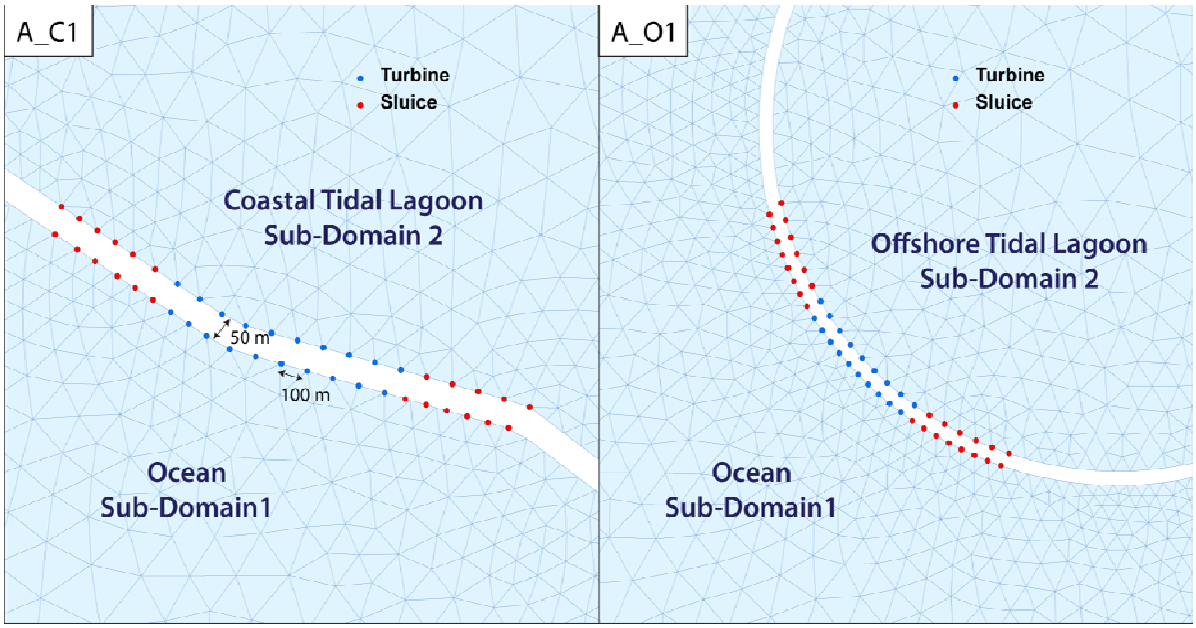

Figure 24. Arrangement of numerical turbines and sluices.

3.1 Simulation of Sluices and Turbines

Several sluices (see Figure 7) are provided to increase the overall efficiency of the power station. The sluices can be used to minimize the water level in the impoundment at low tide, and to maximize the water level within the lagoon at high tide. In the present simulations, the discharge through each sluice Q_S is given by the orifice equation:

$$Q_S = C_S A\sqrt{2g\Delta H} \tag{7}$$

where C_S is the discharge coefficient for a sluice; A is the cross-sectional area (56 m^2); g is the acceleration due to gravity (9.806 m/s); and ΔH is the difference in water level across the powerhouse. In the simulations presented here, $C_S = 0.75$ is assumed.

Following DMC [11], it has been assumed in this study that the powerhouse will be fitted with several horizontal bulb turbines with a runner diameter of 7.5 m, connected to generators that are able to produce up to 20 MW of electrical power. Moreover, it is assumed that the turbines are bi-directional, and are hence able to generate power from water flowing in both directions.

The performance of a turbine is often defined as a "hill chart", relating specific discharge, unit speed and efficiency. These charts are based largely on physical and computational fluid dynamics models. However, detailed information on the performance of turbines and generators for tidal power schemes is difficult to obtain due to the desire by manufacturers to maintain confidentiality. An idealized but realistic turbine performance curve has been developed for use in this study, based on data from Baker [1], reproduced in Figure 25. The curves from [1] have been adapted to suit the case where the maximum power output to the generator is 20 MW, the minimum operating head is 2 m, and the normal operating head is 6 m. The turbine performance curves employed in this study are plotted in Figure 26. It can be seen from the figure that the power increases with increasing water head up to a head of 6 m, and then the power remains

constant at 20 MW for heads above 6 m. The discharge through the turbine also reaches its maximum value when the water head is around 6 m, and decreases for both smaller and larger heads. In this study, efficiencies of 90% on lagoon outflow and 80% on lagoon inflow were assumed. The expressions given in Table 4 were developed to represent the turbine performance curves plotted in Figure 26, and were employed in the numerical simulations to regulate the discharge through each turbine as function of the water head across the powerhouse, and to compute the power output at each time step.

Output	Relationship	Flow conditions
Power (MW)	$P = 0$	$H < H_{min}$
	$P = 0.6638 \cdot H^2 - 0.3376 \cdot H - 1.7601$	$H_{min} \leq H \leq H_{normal}$
	$P = 20$	$H > H_{normal}$
Discharge (m^3/s)	$Q = 0$	$H < H_{min}$
	$Q = -14.45 \cdot H^2 + 196.94 \cdot H - 215.81$	$H_{min} \leq H \leq H_{normal}$
	$Q = 11185 \cdot H^{-1.802}$	$H > H_{normal}$

Notes: H_{min}: Minimum operating head(= 2 m); H_{normal}: Normal operating head(= 6 m).

Table 4. Turbine performance relationships employed in this study.

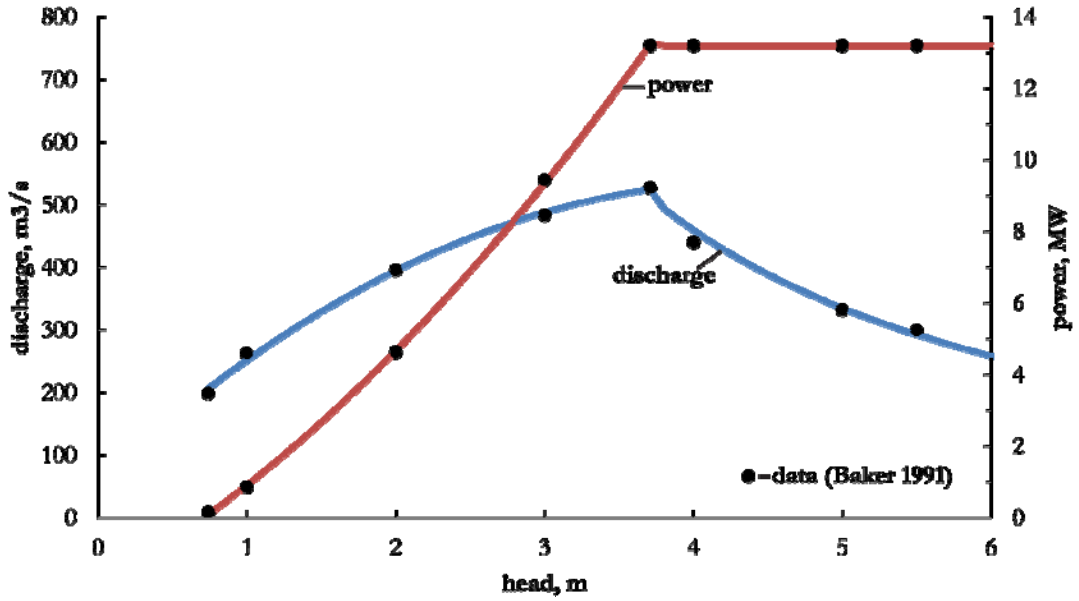

Figure 25. Performance curves for a double-regulated bulb turbine (after Baker, 1991).

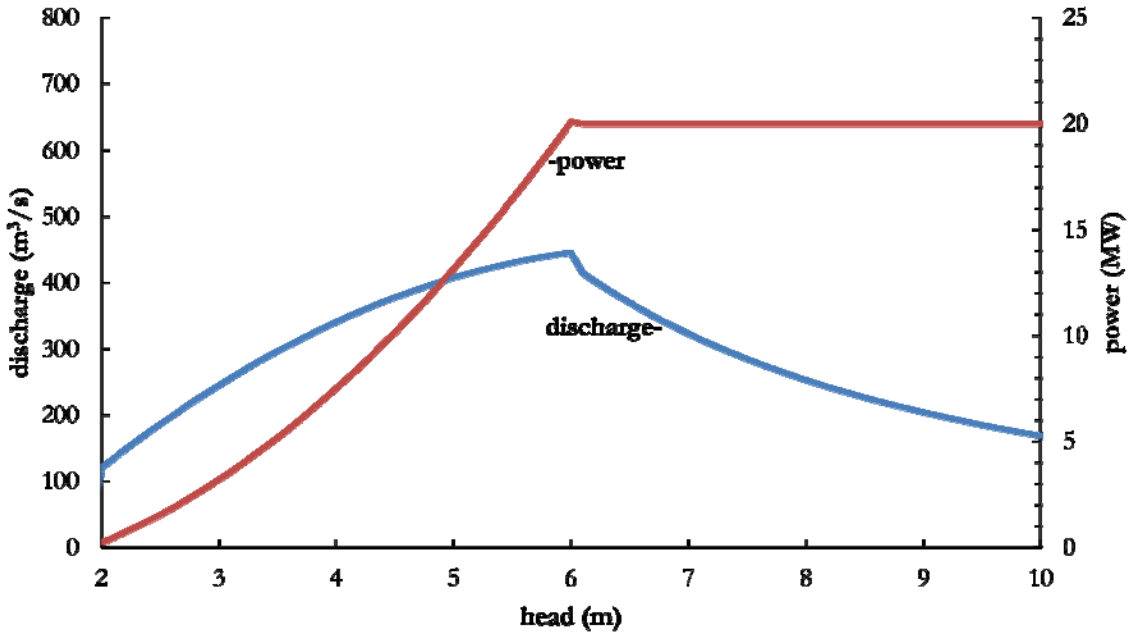

Figure 26. Turbine performance curves employed in this study.

3.2 Operating Modes

Tidal lagoons and barrages can be operated in several different modes, including ebb-generation, flood-generation and bi-directional generation. Ebb-generation is used at the Annapolis Royal Tidal Generating Station. For ebb-generation, the sluices are used to fill the lagoon during flood tide, and power is generated only during ebb tide. For flood generation, power is generated during flood tide only, and the lagoon is drained during ebb tide. For bi-directional generation, power is generated when filling the lagoon during the flood tide and when draining the lagoon during the ebb tide. Bi-directional generation requires that the turbines are operated in both forward and reverse directions. The ebb-generation, flood-generation and bi-directional generation protocols are compared graphically in Figure 27 - Figure 29.

Ebb-generation comprises four stages per tidal cycle, namely: filling, holding, generating and holding. For flood-generation, the four stages are releasing, holding, generating and holding. For bi-directional generation, each tidal cycle comprises six stages: generating, filling, holding, generating, releasing, holding. Each generating stage begins when the head difference across the powerhouse exceeds a minimum value, assumed to be 2.0 m in this study; and ends when the head difference falls below a minimum level, also assumed to be 2.0 m. Figure 30 shows the temporal fluctuations of internal water level, external water level, and power output for the bi-directional generation scheme over several tidal cycles.

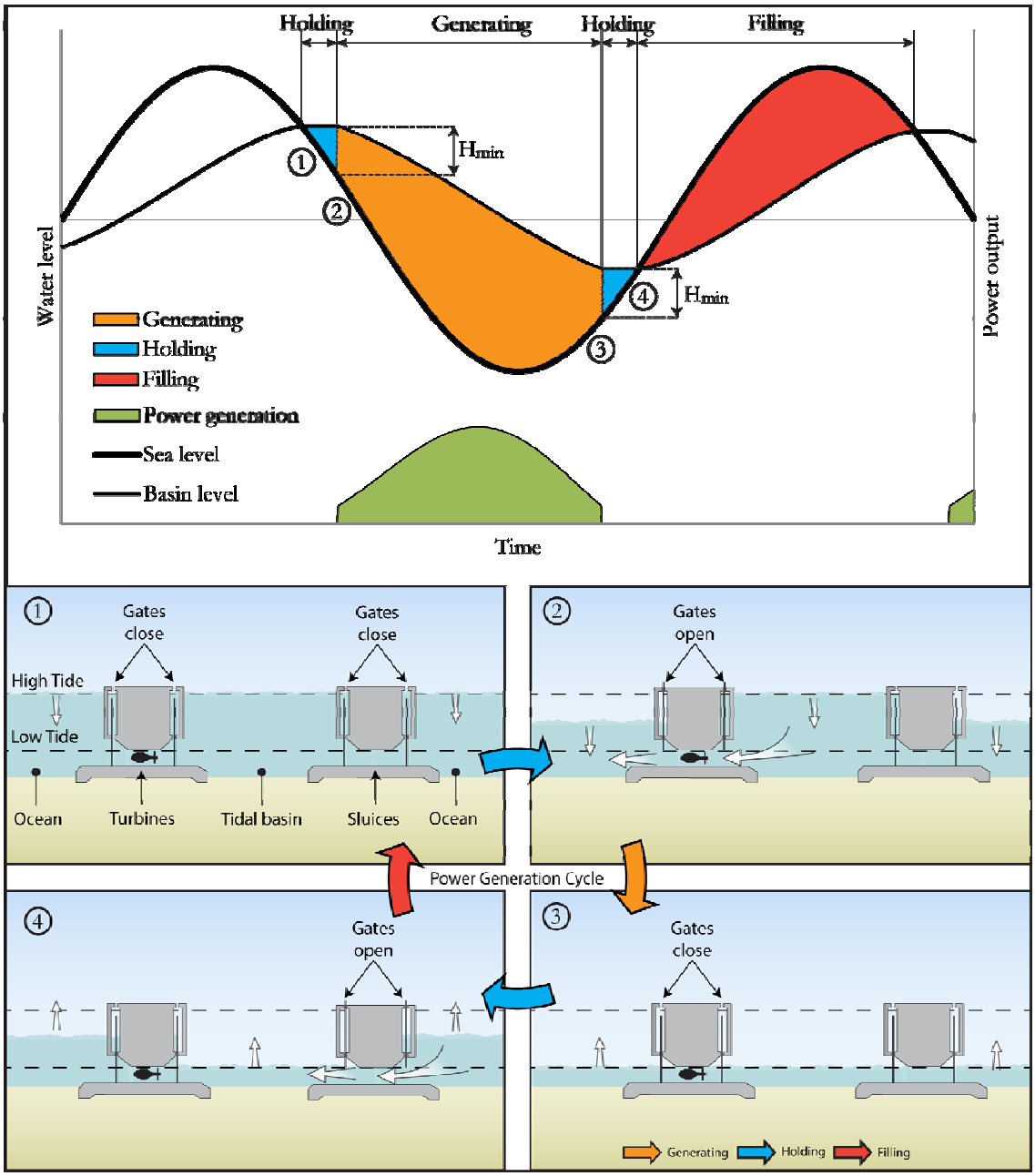

Figure 27. Illustration of ebb generation.

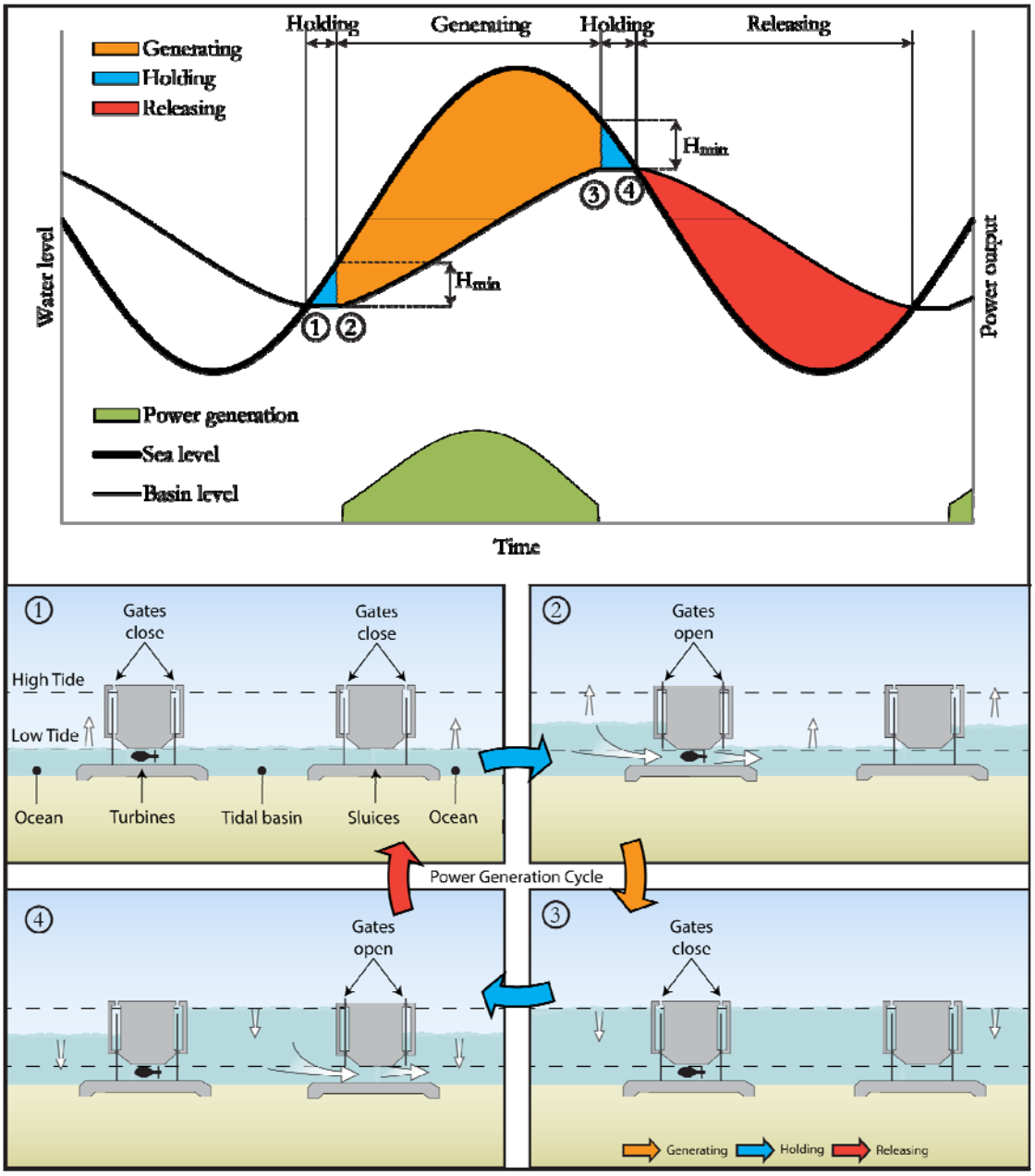

Figure 28. Illustration of flood generation.

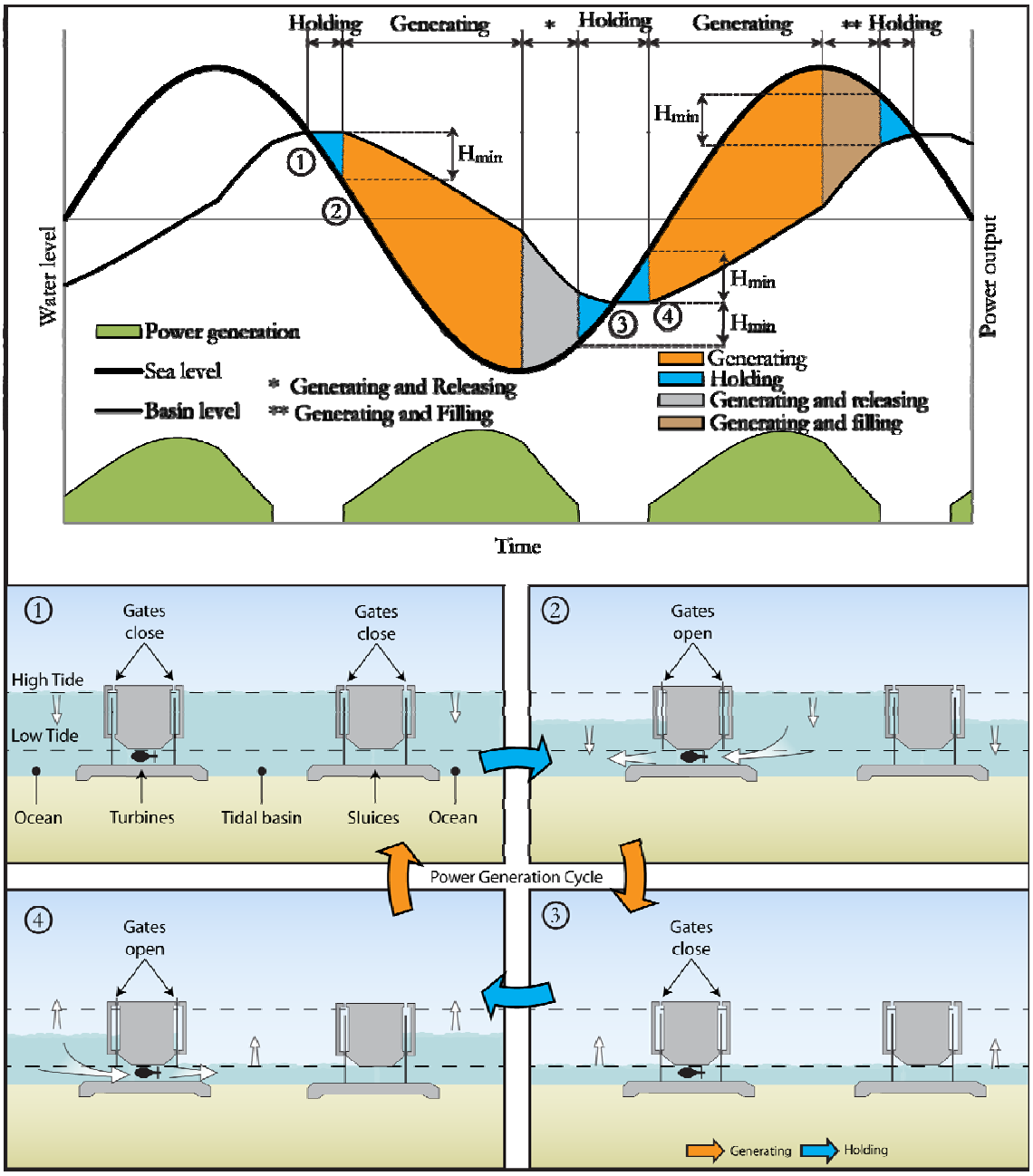

Figure 29. Illustration of bi-directional generation.

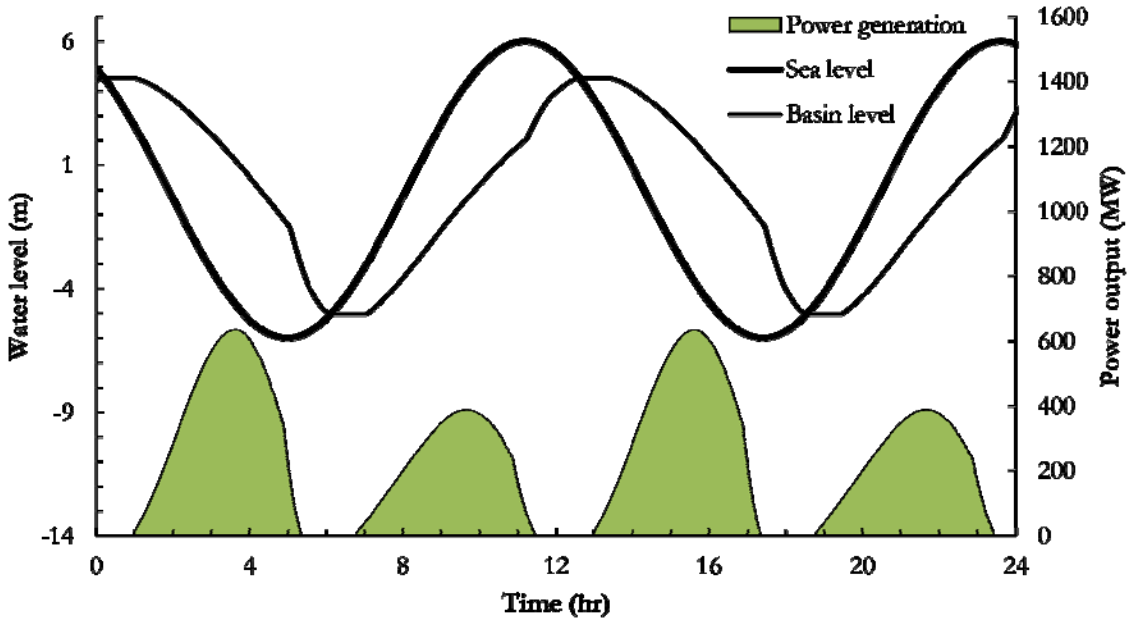

Figure 30. Temporal fluctuations of water level and power output for a bi-directional power generation protocol.

3.3 Power Output

The power output, P, produced by a tidal power lagoon will vary considerably over time as indicated in Figure 27 - Figure 30, depending on whether or not there is flow through the turbines and the head forcing the flow. In this study, the root-mean-square (RMS) value of the power output, P_{RMS}, is used to characterise the time-varying power output. P_{RMS} is defined as

$$P_{RMS} = \sqrt{\frac{\sum_{j=1}^{m}\left(\sum_{i=1}^{n} P_i\right)^2}{m}} \tag{8}$$

where i is the turbine number, n is the number of turbines, j is the simulation step number, and m is the number of steps in the simulation. In this study, the power output at each time step of the numerical computations has been calculated using the equations in Table 4.

3.4 Analytical Model of Plant Operations

A simple analytical model describing the operation of a tidal lagoon power plant was developed and applied to determine the optimal number of turbines and sluices for a given lagoon. In this model, the lagoon impoundment is defined by a curve relating the water level to the surface area of the impoundment. Water level - surface area curves developed for some of the different coastal lagoons considered in this study are shown in Figure 31. More information on these lagoons can be found in Section 4. In the simple analytical model, the flows through the sluices are calculated using the orifice equation, while the flows through the turbines and the power output are based on the performance curves shown in Figure 25.

The simple model was applied to assess the sensitivity of power output to the number of turbines in the powerhouse, and to assess the influence of sluice capacity on the overall plant efficiency. In other words, the simple model was used to obtain an estimate of the optimal number of turbines and sluices for each tidal power lagoon, and for each mode of operation (2-way generation, ebb-generation or flood-generation). A simple sinusoidal tidal wave with 6 m amplitude and 12.42 hour period was assumed in these calculations.

Figure 32 shows an example of the variation in power output with the number of turbines and the number of sluices, calculated by the analytical model, for the case of lagoon A_C1 (a 26.7 km^2 coastal lagoon located along the northern shore of Minas Basin). The results show that, in order to maximize power generation, it is important to maintain a balance between the number of turbines and the number of sluices. For this case, the optimal number of turbines for maximum power generation varies with the number of sluices over the range from ~22 turbines (for 1 sluice) up to ~36 (for 1000 sluices). In reality, installing a large number of sluices to obtain a small increase in power output will not be economically viable. In this study, we have assumed that a realistic powerhouse will more likely be configured to achieve roughly 80% of power output that could be generated with an infinite number of sluices. In the case of lagoon A_C1 (see Figure 32), the optimal powerhouse configuration features 29 turbines and 31 sluices. Adding more turbines without adding sluices will result in reduced power output.

Results from the simple analytical model show that the average power output for the flood-generation mode is approximately 65% of the output for either the ebb-generation or bi-directional generation modes, which are roughly equal. Menint [30] has shown from experience with the tidal barrage at La Rance in France that, due to various inefficiencies, 2-way generation produces less energy than ebb-generation. Although bi-directional generation requires turbines that are able to generate power on both the inflow and outflow, it can in theory produce as much or even more energy than the ebb-generation mode. For 2-way generation there are 2 periods of power generation per tide cycle, compared to one period per tide cycle for both the ebb- and flood-generation modes. This feature may make it easier to match fluctuations in demand.

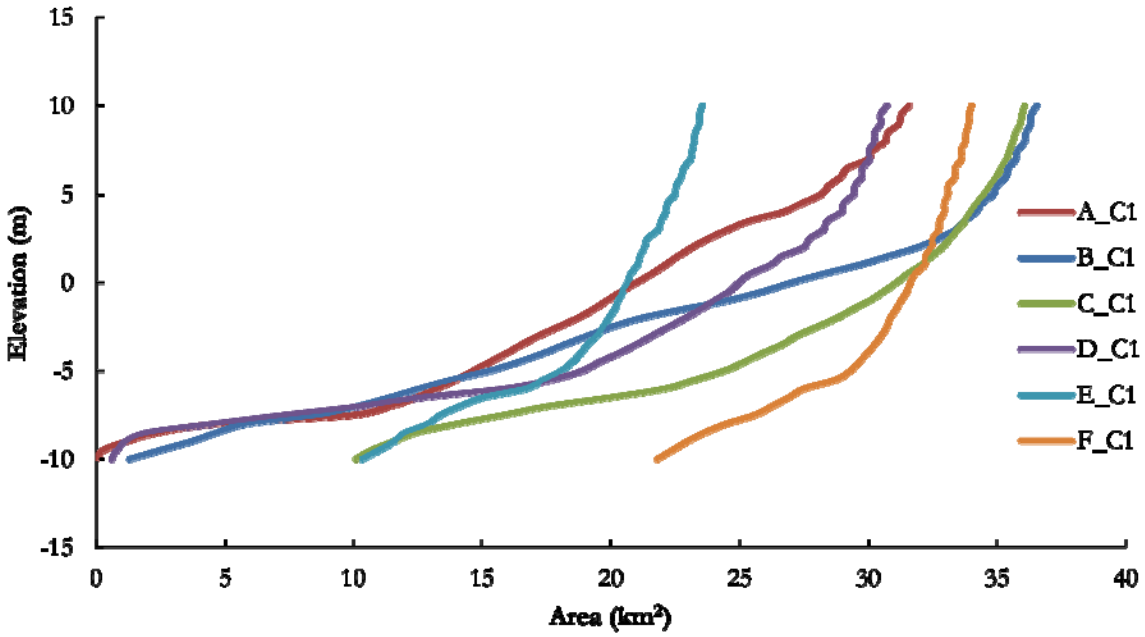

Figure 31. Water level – area curves for several coastal lagoons.

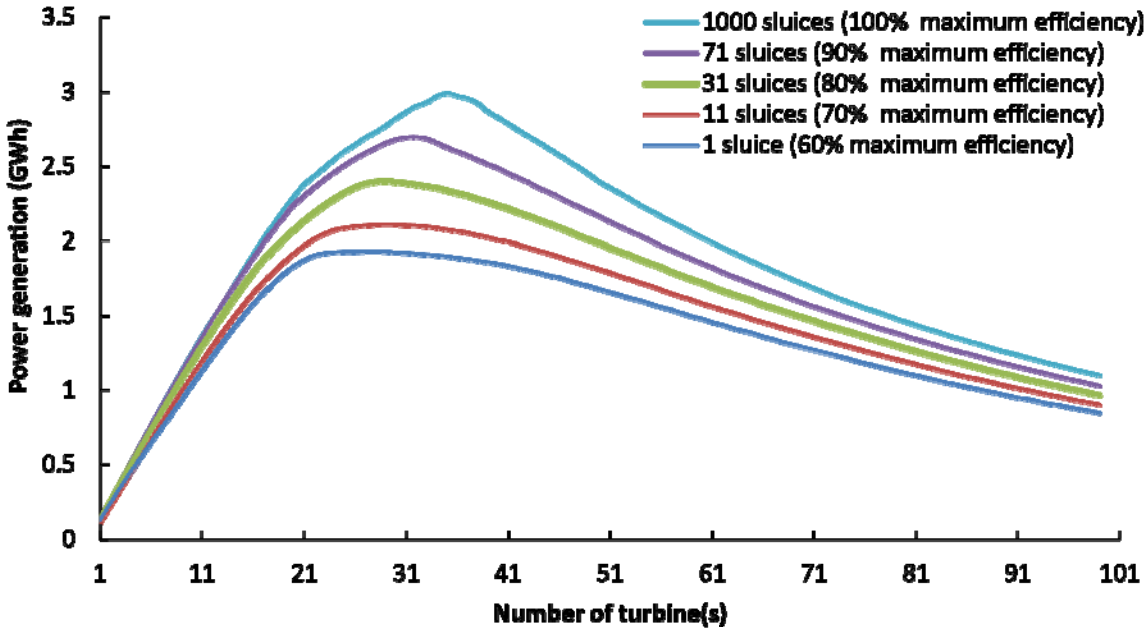

Figure 32. Optimisation of powerhouse configuration for lagoon A_C1, 2-way generation.

4 Modelled Scenarios

The numerical model has been used to study the effects that operating tidal lagoons might have on the tidal hydrodynamics in the Bay of Fundy and throughout the Gulf of Maine. Nineteen different hypothetical scenarios with one or more tidal power lagoons located in Minas Basin and/or in Chignecto Bay have been modelled. These nineteen scenarios were developed to allow the influence of various parameters to be assessed, including: lagoon type; lagoon location; lagoon size; number of lagoons; and operating protocol. Single lagoons were simulated in some scenarios, while up to six lagoons operating simultaneously were modeled in others. In this way, the relationship between the scale of lagoon development and the scale of potential impacts has been ascertained.

Numerical lagoons were constructed at six different sites where shallow tidal flats create ideal conditions. These sites, named sites A - F, are mapped in Figure 33. Site A is located along the northern shore of Minas Basin between Five Islands and Economy Point. Site A was considered by DMC [11]. Site B is also found along the northern shore of Minas Basin, east of site A near Upper Economy. Site C is located along the southern shore of Minas Basin near Cambridge. Site D is found along the western shore of Chignecto Bay near Mountville. Site E is located on the eastern shore of Chignecto Bay near Ragged Reef. Finally, site F is found on the south-western shore of Chignecto Bay between Alma and Cape Enrage.

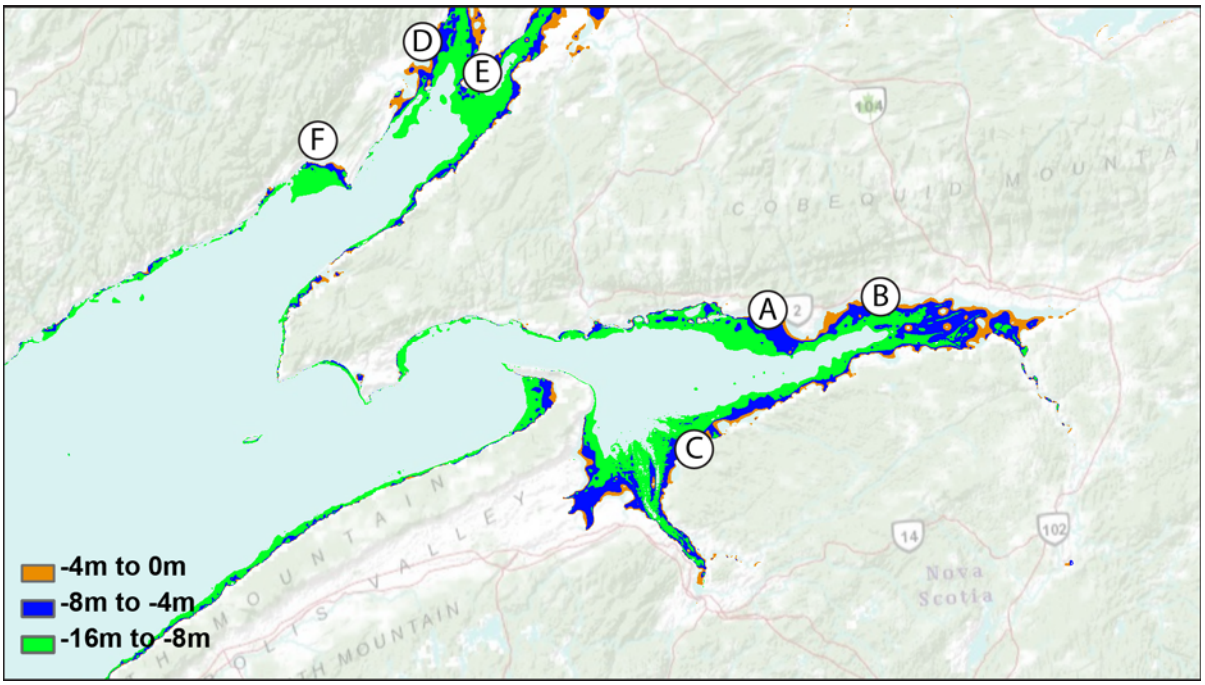

Figure 33. Sites A-F are located on the shallow tidal flats in Minas Basin and Chignecto Bay.

Eight different lagoons were modelled at site A; four of these were coastal lagoons where the shoreline formed a portion of the impoundment; and four were offshore lagoons separated from the natural shoreline. A single coastal lagoon and a single offshore lagoon were modelled at each

of the other five sites. All of the lagoons featured a single storage basin. Several key properties of the eighteen different numerical tidal power lagoons considered in this study are summarized in Table 5, including the impoundment area (at mean sea level); the dyke length, and the number of 7.5 m, 20 MW turbines and 56 m^2 sluices. Note that the number of sluices and turbines was varied depending on whether flood-generation, ebb-generation or bi-directional generation was modelled. The nine different coastal lagoons are mapped in Figure 34, while the nine offshore lagoons are shown in Figure 35. The different computational meshes (grids) developed to simulate the various coastal and offshore lagoons at site A are compared in Figure 36.

No.	Site	Lagoon Name	Lagoon Area (km^2)	Dyke length (km)	Two-way generation		Ebb generation		Flood generation	
					# of turbines	# of sluices	# of turbines	# of sluices	# of turbines	# of sluices
1	A	A_C1	26.66	10.92	24	15	20	26	16	17
2	A	A_O1	12.01	12.44	14	15	10	12	10	12
3	A	A_C1	26.66	10.92	22	31	20	26	16	17
4	A	A_C2	35.10	13.92	30	41	26	34	22	25
5	A	A_C3	57.65	19.00	52	72	45	54	41	47
6	A	A_O1	12.01	12.44	12	23	10	12	10	12
7	A	A_O2	17.98	15.20	19	29	14	17	15	19
8	A	A_O3	23.99	17.52	23	39	20	23	20	25
9	B	B_C1	34.16	14.43	29	31	26	32	18	19
10	B	B_O1	12.01	12.44	12	22	10	12	10	12
11	C	C_C1	33.96	16.32	31	40	26	32	24	28
12	C	C_O1	12.01	12.44	12	24	10	12	10	13
13	D	D_C1	28.95	14.90	25	32	22	27	19	22
14	D	D_O1	12.01	12.44	12	23	10	12	10	12
15	E	E_C1	22.13	10.63	21	31	18	21	17	20
16	E	E_O1	12.00	12.44	12	23	10	12	10	12
17	F	F_C1	32.94	12.38	32	48	26	31	26	31
18	F	F_O1	12.01	12.44	12	23	10	12	10	12

Table 5. Properties of numerical tidal power lagoons considered in this study.

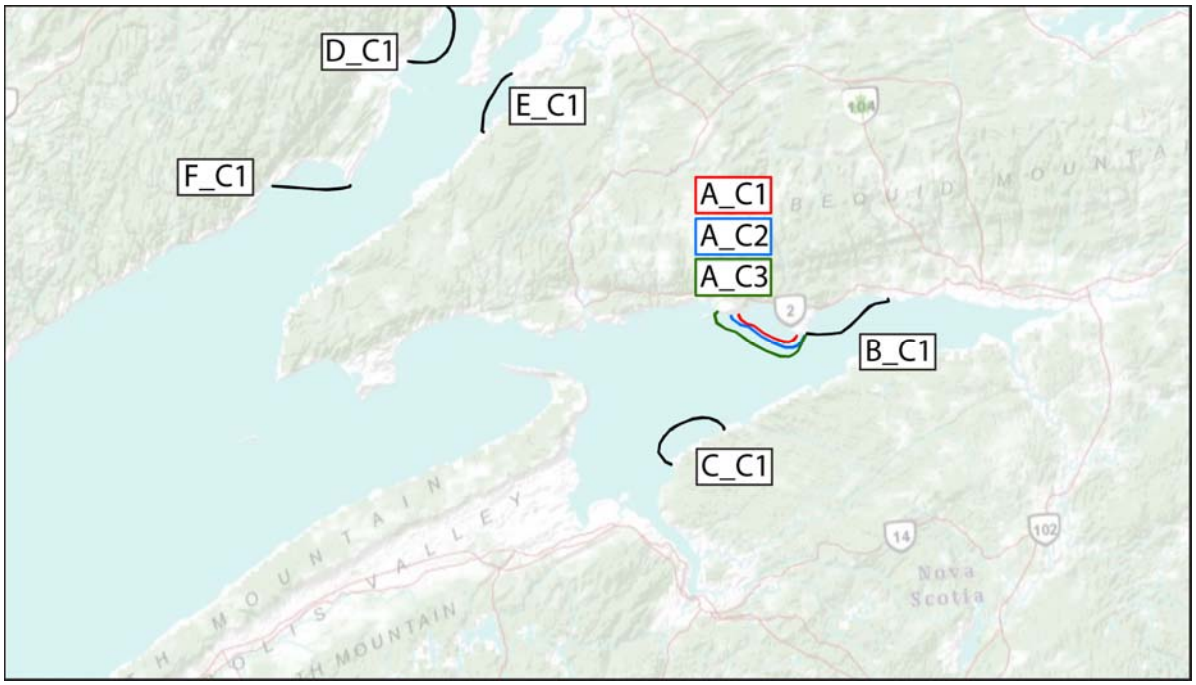

Figure 34. Arrangement of coastal tidal lagoons at sites A-F.

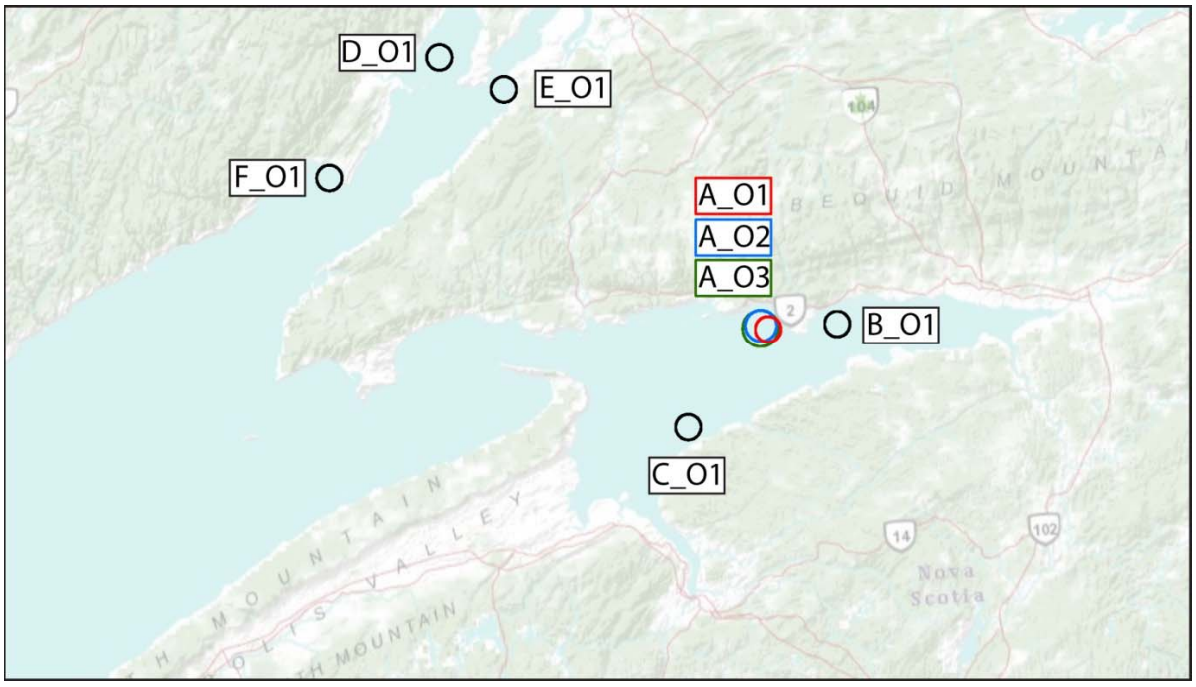

Figure 35. Arrangement of offshore tidal lagoons at sites A-F.

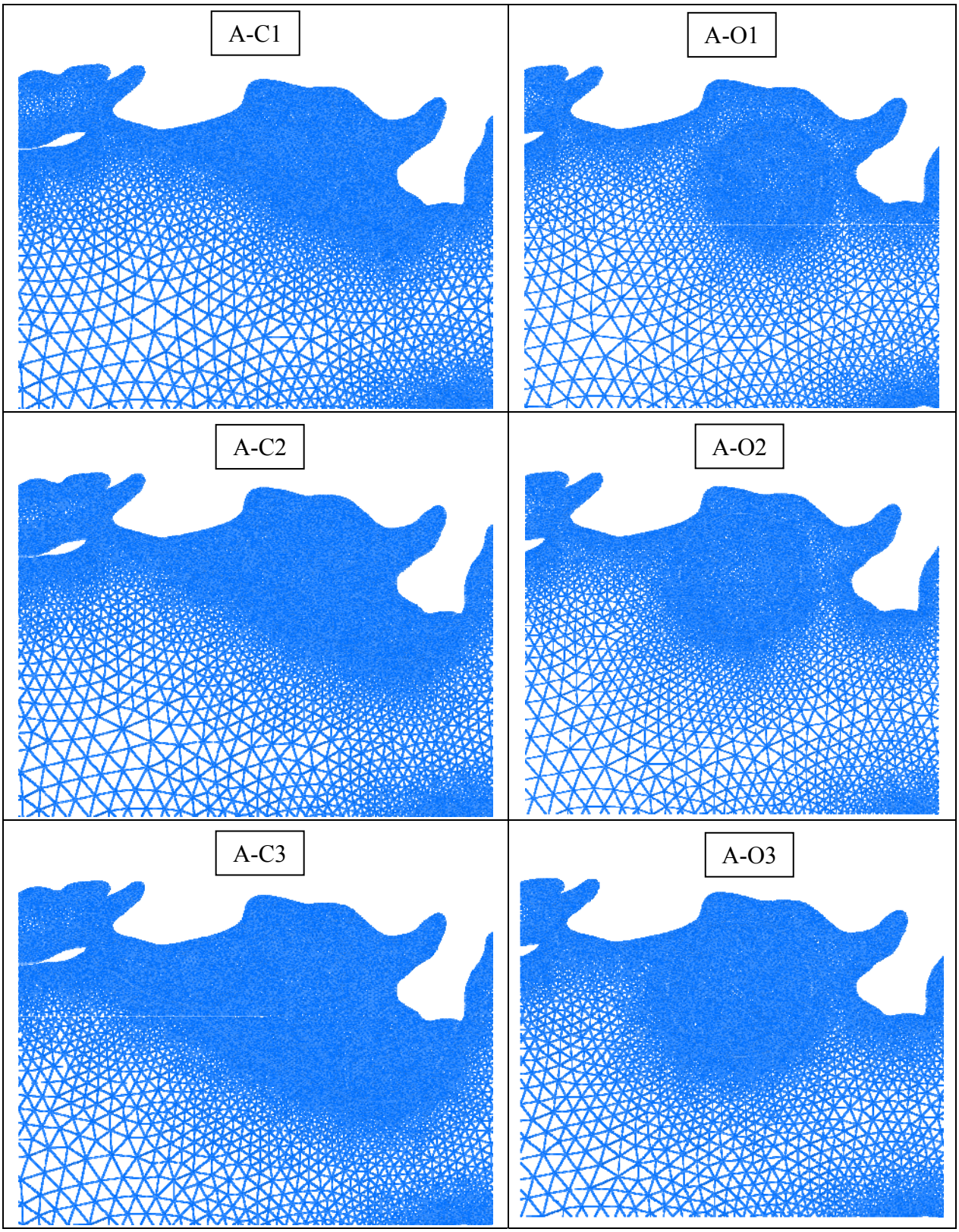

Figure 36. Computational meshes (grids) for simulating coastal and offshore lagoons at site A.

The nineteen different scenarios considered in this study were developed by assuming the presence of one or more of the individual lagoons described in Table 5. Single lagoons were modelled in scenarios S1-S14, while multiple lagoons were considered in scenarios S15-S19. The arrangement of lagoons for the various scenarios is summarised below in Table 6. Also listed in this table are the total number of 7.5 m diameter, 20 MW turbines, the total number of 56 m^2 sluices, the total area impounded within the lagoons (at mean sea level), and the operating mode (power cycle) that was assumed. For example, the table shows that three coastal lagoons at sites A, B and C were assumed for scenario S15. Six offshore lagoons, one each at sites A-F, were assumed for scenario S19. The total area impounded by the lagoons varied from a minimum of 12 km^2 for scenarios S2 and S10, up to a maximum of 94.8 km^2 for scenario S15.

Scenarios S1 and S2 (12 km^2 offshore lagoon or 26.7 km^2 coastal lagoon at site A) were based on proposals developed for Tidal Electric Canada by DMC [11]. The 12 km^2 offshore lagoon is detached from shore and comprises a 11.9 km long circular dyke and a powerhouse with fourteen 20 MW bulb turbine generators centered between 15 sluice gates (total sluice area: 15*56 m^2 = 840 m^2). According to DMC, this offshore lagoon will generate an average power output of approximately 124 MW. The larger coastal lagoon, equipped with twenty-four 20 MW bulb turbines and 15 sluices, is estimated to have an average power output of approximately 220 MW.

The influence of operating mode can be assessed by comparing results for scenarios S3-S7. In scenario S6, it was assumed that no power was being generated and the turbines remained permanently closed while the sluices were locked open. For scenario S7, the lagoon was modelled with both the turbines and sluices closed, hence there was no exchange of seawater between the lagoon and the surrounding sea.

The influence of lagoon size can be assessed by comparing results for scenarios S3 and S8-S12. In these scenarios, lagoon size varied from 12.0 km^2 to 57.7 km^2.

The influence of lagoon location can be assessed by comparing results for scenarios S3, S13 and S14. In these three scenarios, single coastal lagoons of similar size were modelled at sites A, B and C. The influence of location can also be judged by comparing results for scenarios S15 and S17, and for scenarios S16 and S18. In scenario S15, 3 coastal lagoons located in Minas Basin were modelled; whereas in scenario S17, 3 similarly-sized coastal lagoons located in Chignecto Bay were modelled. Three 12 km^2 offshore lagoons located in Minas Basin were modelled in scenarios S16, while three identical offshore lagoons located in Chignecto Bay were modelled in scenario S18.

The same boundary forcing, developed from 10 harmonic constituents, was employed in every case. All the simulations spanned the same 14.8 day period from 0:00 on 28 Aug 2007 to 18:30 on 11 September 2007, when the Spring and Neap tides were very close to long term average conditions. A 3-day warm-up simulation was performed in order to obtain reasonable initial conditions throughout the domain at the start of the 14.8 day period. Flows through the powerhouse were not calculated during the warm-up period.

In addition to modelling hypothetical scenarios S1 to S19 as described above, the tidal flows for existing conditions without lagoons (scenario S0) were also modelled for the same 14.8 day period using the same boundary conditions. The changes in tidal hydrodynamics due to each hypothetical scenario with lagoons were estimated by differencing the model results for each hypothetical scenario with those for existing conditions. The impact of each hypothetical

scenario on water levels, tide range, depth-averaged tidal current speed and bed shear stress have all been assessed in this manner.

Scenario	Model grid	Coastal lagoons	Offshore lagoons	Power cycle	# of Lagoons	# of Turbines	# of Sluices	Total area (km^2)	RMS Power output (MW)
S1	A_C1	A_C1	-	2-way	1	24	15	26.7	265
S2	A_O1	-	A_O1	2-way	1	14	15	12.0	156
S3	A_C1	A_C1	-	2-way	1	22	31	26.7	264
S4	A_C1	A_C1	-	ebb	1	20	26	26.7	246
S5	A_C1	A_C1	-	flood	1	16	17	26.7	172
S6	A_C1	A_C1	-	open	1	-	-	26.7	0
S7	A_C1	A_C1	-	closed	1	-	-	26.7	0
S8	A_C2	A_C2	-	2-way	1	30	41	35.1	373
S9	A_C3	A_C3	-	2-way	1	52	72	57.7	658
S10	A_O1	-	A_O1	2-way	1	12	23	12.0	142
S11	A_O2	-	A_O2	2-way	1	19	29	18.0	239
S12	A_O3	-	A_O3	2-way	1	23	39	24.0	296
S13	B_C1	B_C1	-	2-way	1	29	31	34.2	360
S14	C_C1	C_C1	-	2-way	1	31	40	34.0	385
S15	m3_C1	A_C1 B_C1 C_C1	-	2-way	3	22 29 31	31 31 40	94.8	988
S16	m3_O1	-	A_O1 B_O1 C_O1	2-way	3	12 12 12	23 22 24	36.0	411
S17	m3_C2	D_C1 E_C1 F_C1	-	2-way	3	25 21 32	32 31 48	84.0	747
S18	m3_O2	-	D_O1 E_O1 F_O1	2-way	3	12 12 12	23 23 23	36.0	312
S19	m6_O1	-	A_O1 B_O1 C_O1 D_O1 E_O1 F_O1	2-way	6	12 12 12 12 12 12	22 23 24 23 23 23	72.1	723

Table 6. Description of scenarios S1-S19.

5 Results & Discussion

5.1 Existing Conditions, Scenario S0

Numerical results for scenario S0 (existing conditions) are presented below to provide an overview of the main features of the tidal hydrodynamics in the upper Bay of Fundy.

The bathymetry of the upper Bay of Fundy is mapped in Figure 37. The deepest depths in this part of the Bay are found at Minas Passage (up to 150 m). Depths in Minas Basin are generally shallower than 20 m, while depths in central and upper reaches of Chignecto Bay are also generally less than 20 m.

The maximum tide range predicted by the numerical model for the upper bay is presented in Figure 38. The highest tide range over the 15-day simulation period is ~13.8 m, and occurs in the eastern part of Minas Basin between Economy and Highland Village. The tide range in Chignecto Bay is smaller, reaching a maximum of ~11.7 m in Cumberland Basin. Note that the simulation period was selected to include average Spring and Neap tides; hence the simulations do not include the extreme high tides that can occur at certain times, nor did they include the extreme low tides.

The depth-averaged flood and ebb currents at Minas Passage during an average Spring tide are mapped in Figure 39 and Figure 40. The predicted flows are generally consistent with results from other numerical models, and with velocity measurements. On the flood, a large eddy forms immediately north of Cape Split which forces the main flow towards the central and northern parts of the Passage, and the flow reverses along the southern shore. On the ebb, the main flow is distributed more evenly across the Passage. As a result, currents in the neck of the passage are stronger on the flood than on the ebb. There are also several large eddies that form in bays along the shore which then detach when the tide turns and are subsequently swept through the Passage. On the flood, the main flow separates from the tip of Cape Split, and concentrates in the central and northern parts of the Passage, whereas the ebb flow fills the entire passage and is slightly weaker.

The maximum depth-averaged current speed, U_{max}, over the 15-day simulation is mapped in Figure 41. It is important to note that these maximum velocities generally do not all occur at the same time, but occur at different times in different places. The strongest depth-averaged currents (exceeding 4 m/s) are found near the tip of Cape Split and in the western and central parts of Minas Passage. In most parts of Minas Basin and Chignecto Bay, maximum currents do not exceed 2 m/s.

The depth-averaged root-mean-square (RMS) velocity, U_{RMS}, is mapped in Figure 42. This parameter, which provides a robust statistical measure of the magnitude of a time-varying quantity, is defined as

$$U_{RMS} = \sqrt{\frac{\sum_{i=1}^{n} U_i^2}{n}} \tag{9}$$

Where U_i is the depth-averaged velocity at time step i, and n is the number of steps in the simulation. The RMS velocity includes contributions from all time steps throughout the entire simulation.

Bottom sediments will be mobilized whenever the shear stress exerted on the seabed due to the tidal flows exceeds the critical shear stress for incipient motion, which, for non-cohesive materials, is mainly a function of the sediment grain size and density. Increases in bed shear stress can lead to increases in sediment transport and erosion of a seabed, while reductions in bed shear stress can lead to decreases in sediment transport and accretion of a seabed. An estimate of the maximum shear stress exerted by the tidal flows on the seabed, τ_{max}, is mapped in Figure 43. This parameter is defined as

$$\tau_{max} = \max_{i=1 \to n} \left(\rho \frac{u_i^2 v_i^2}{C^2} \right) \tag{10}$$

where ρ is the water density, u_i and v_i are the depth-averaged velocities in the x and y directions at time step i, and C is the local Chézy coefficient. The root-mean-square (RMS) value of the shear stress, τ_{RMS}, is calculated as:

$$\tau_{RMS} = \sqrt{\frac{\sum_{i=1}^{n} \left(\rho \frac{u_i^2 v_i^2}{C^2} \right)^2}{n}} \tag{11}$$

The RMS shear stress includes contributions from all time steps, whereas the maximum shear stress denotes the single largest shear stress over the 15-day simulation.

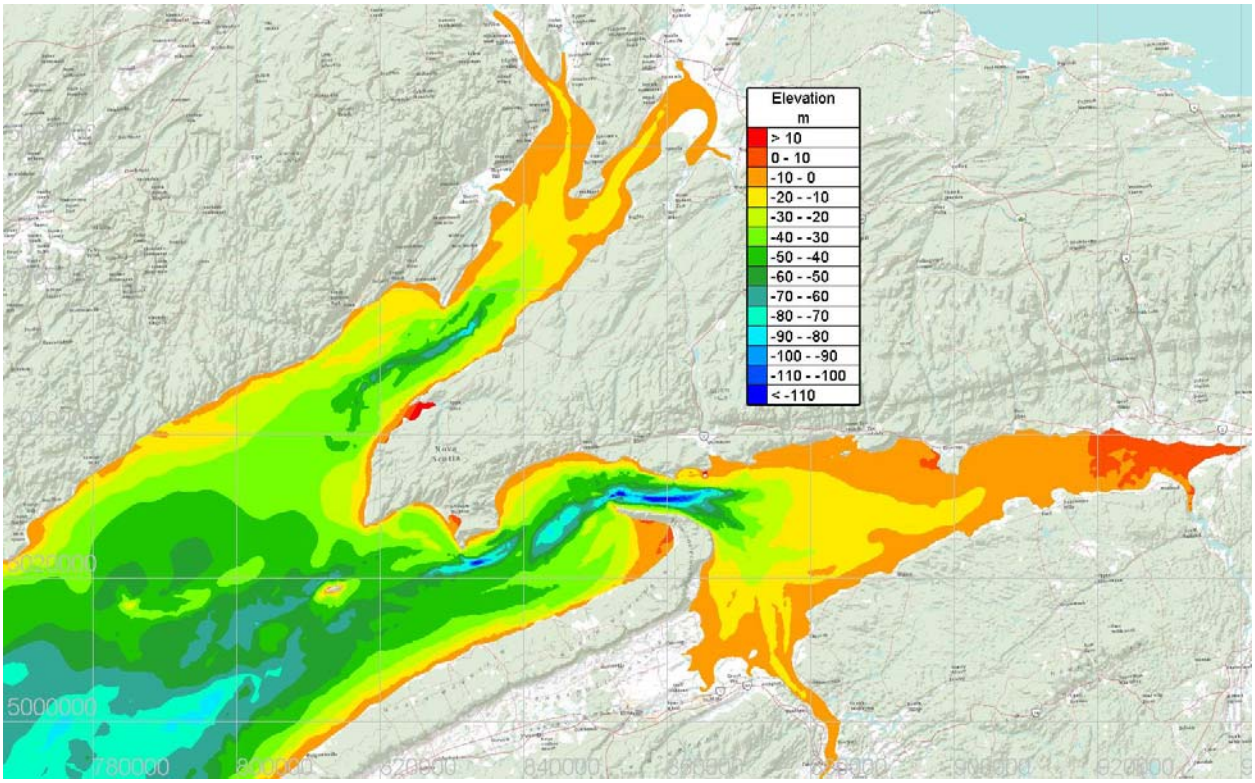

Figure 37. Bathymetry of the upper Bay of Fundy.

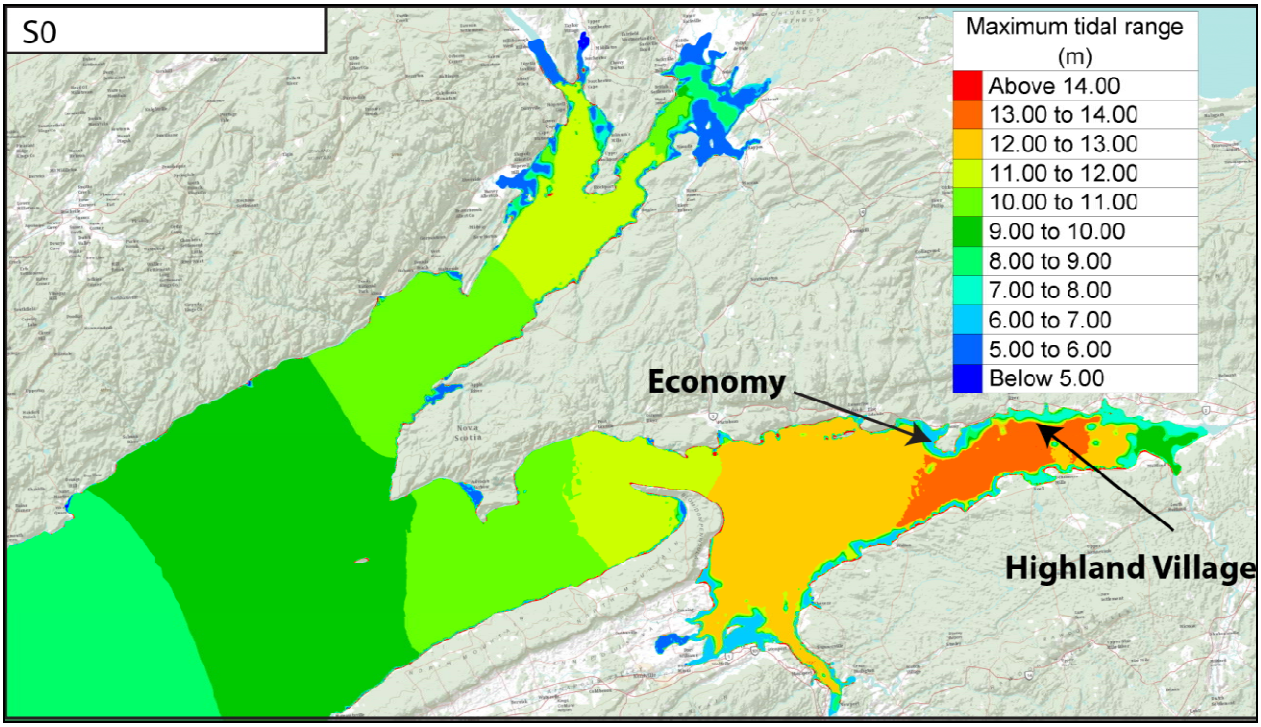

Figure 38. Maximum tide range for existing conditions (scenario S0).

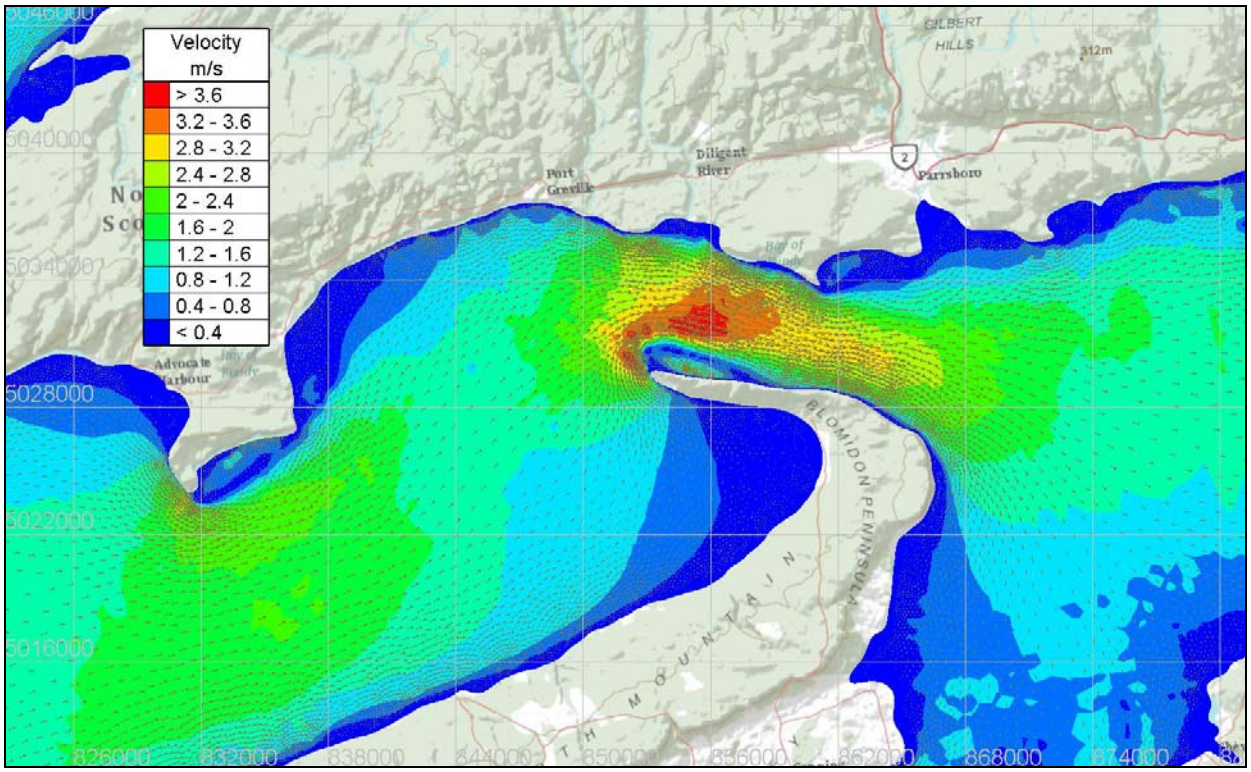

Figure 39. Spring tide flood currents at Minas Passage for existing conditions (scenario S0).

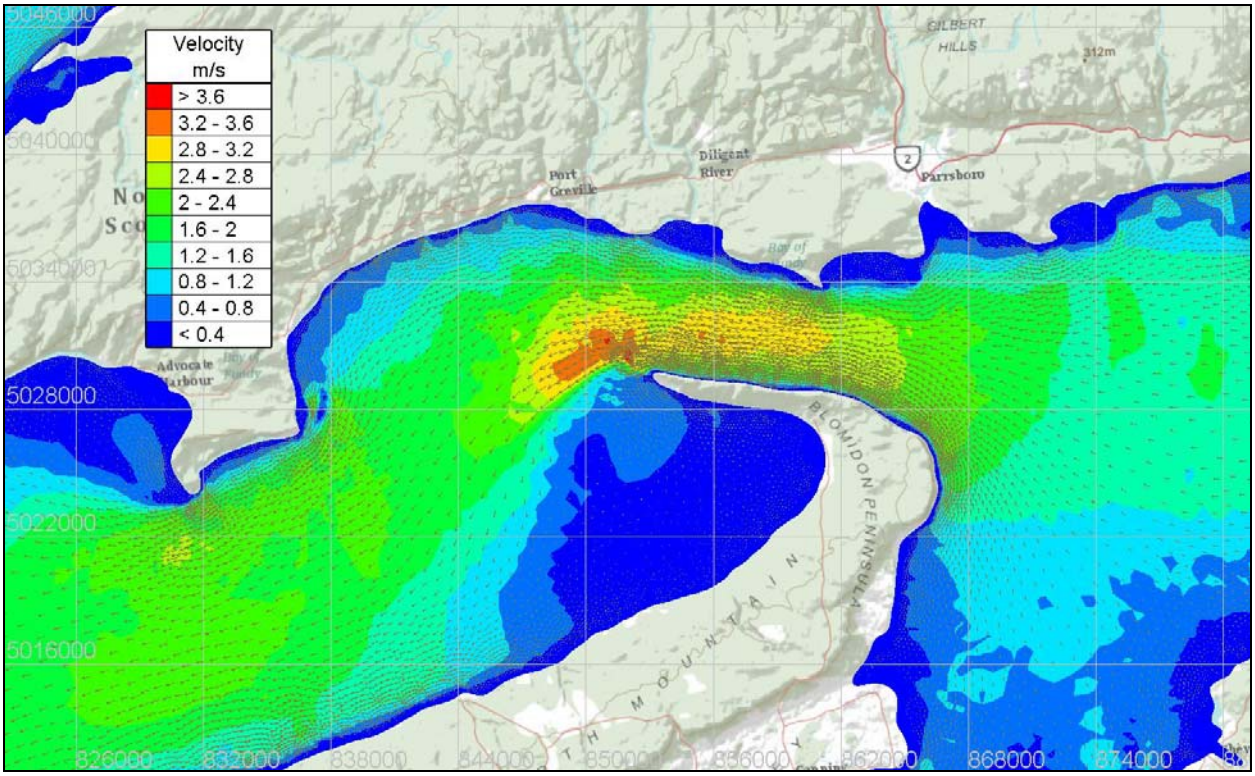

Figure 40. Spring tide ebb currents at Minas Passage for existing conditions (scenario S0).

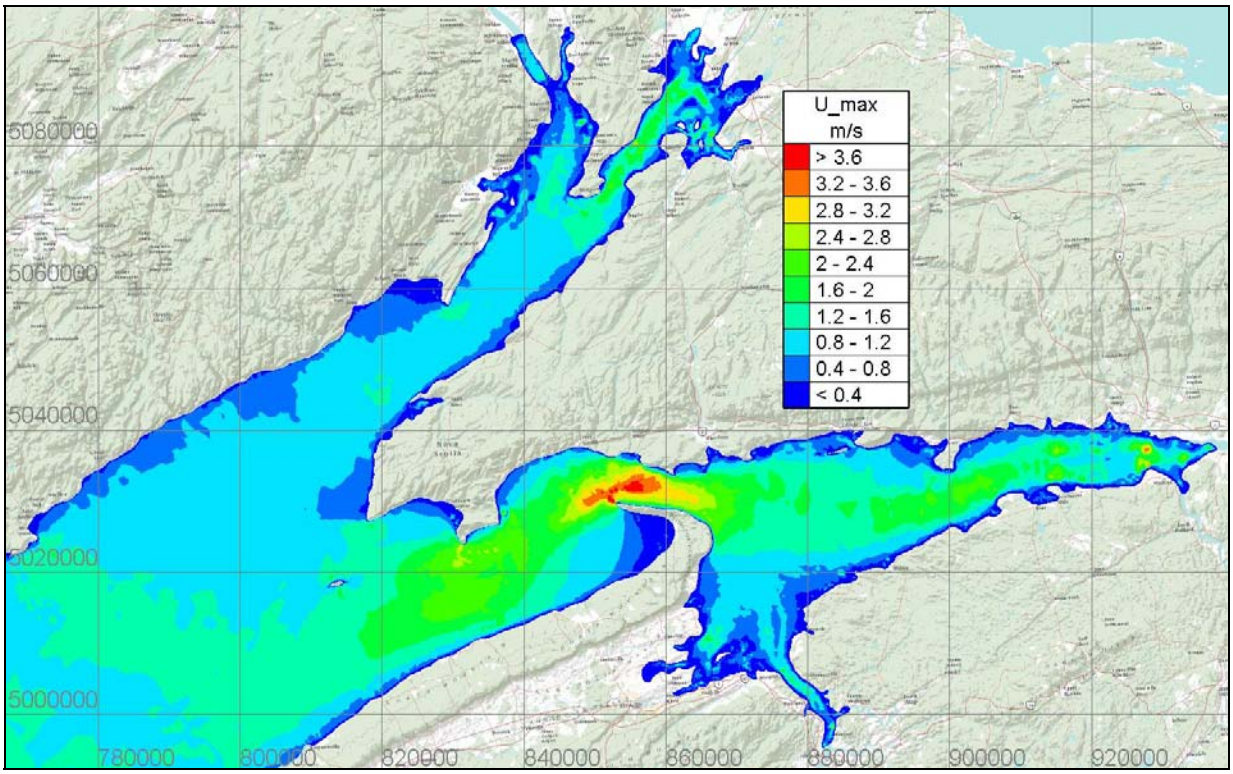

Figure 41. Maximum depth-averaged current speed U_{max} for existing conditions (scenario S0).

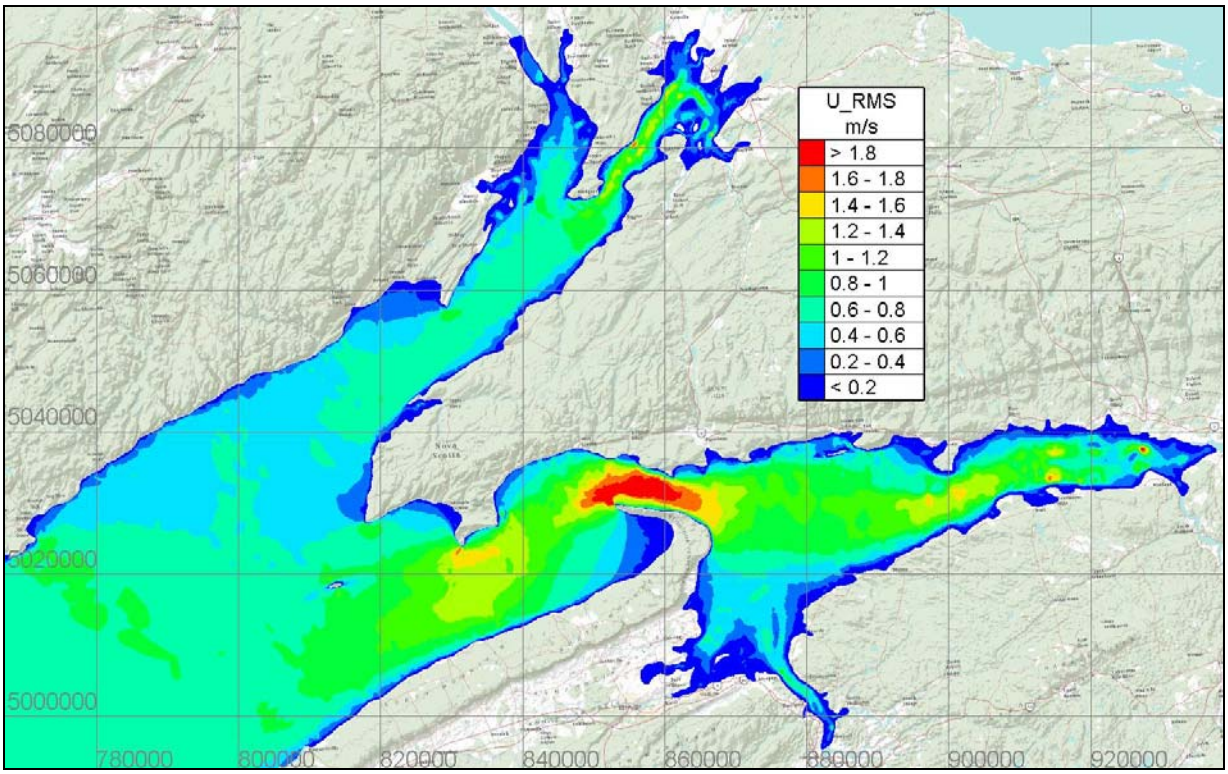

Figure 42. Depth-averaged RMS current speed U_{RMS} for existing conditions (scenario S0).

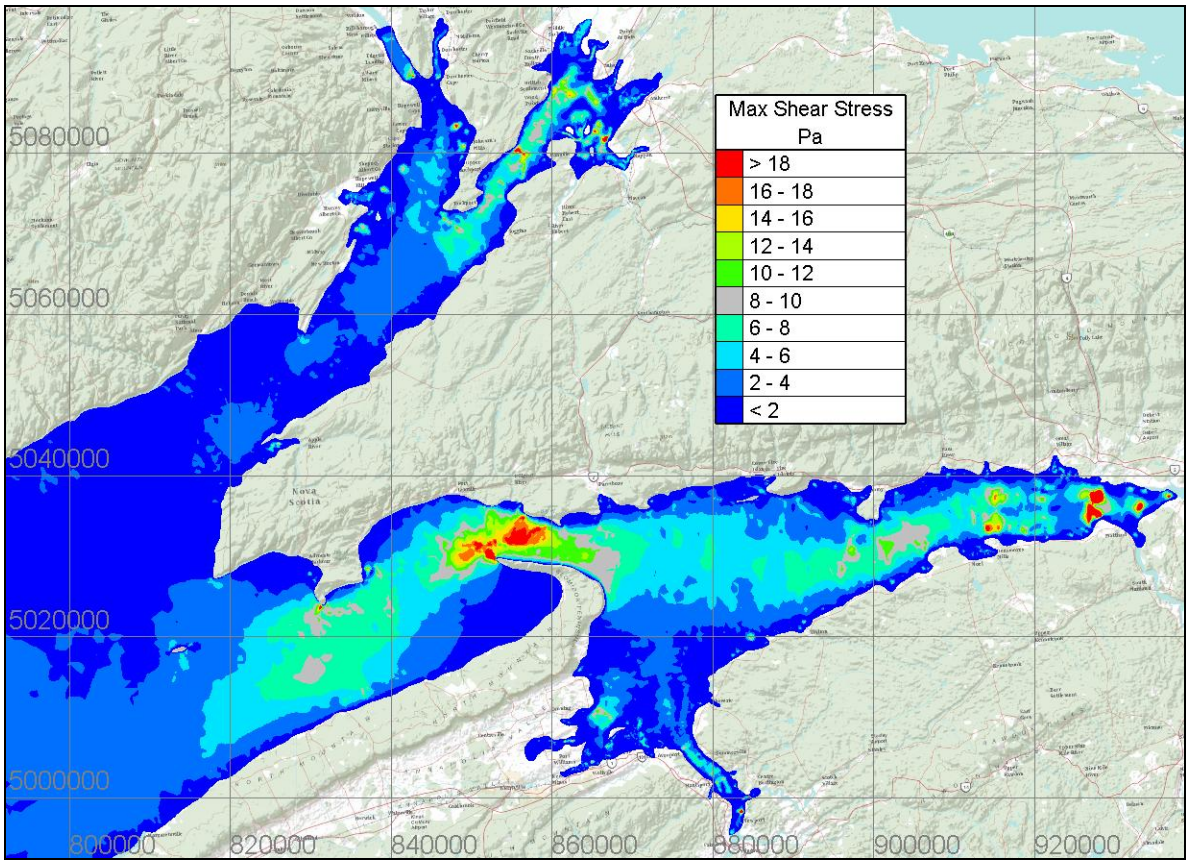

Figure 43. Maximum bed shear stress τ_{max} for existing conditions (scenario S0).

5.2 Single Coastal and Offshore Lagoons at Site A, Scenarios S1 and S2

The tidal power lagoons modelled in scenarios S1 and S2 were developed to replicate the lagoons proposed in the feasibility study by DMC [11]. The hydrodynamic impacts of these proposals are examined below.

The numerical simulations indicate that a 26.7 km^2 coastal lagoon at site A (scenario S1) will have a rather small impact on water levels within Minas Basin and throughout the BoF and GoM, and that the impact of the smaller 12 km^2 offshore lagoon (scenario S2) will be even smaller. Figure 44 shows the predicted change in maximum tide range for scenarios S1 and S2. Along the shores of Minas Basin outside the lagoon, the reduction in tide range for scenarios S1 varies from 0 cm at Minas Passage up to approximately 9 cm close to the lagoon, and up to approximately 6 cm for scenario S2. Moreover, the model predicts that the 26.7 km^2 coastal lagoon is responsible for a ~2 cm increase in tide range along a large portion of the BoF and GoM coastline. The 12 km^2 offshore lagoon modelled in scenario S2 has an even smaller effect on the far-field tide range; for this case, the predicted change in tide range along the shore of the Gulf of Maine is on the order of 1 cm or less.

While these changes represent a very small percentage of the tide range, their potential impact on communities and ecosystems warrants careful consideration and further investigation. The

largest water level changes occur inside the impoundment, where, compared to present conditions, the tide range is reduced by several meters.

The predicted changes in maximum water level for scenarios S1 and S2 are mapped in Figure 45. For scenario S1, small water level increases are predicted for the western and southern parts of Minas Basin, Minas Passage, and the upper Bay of Fundy, including Chignecto Bay. Virtually no change in maximum water level is predicted for the central and eastern parts of Minas Basin. For scenario S2, the predicted changes in maximum water level are even smaller than for scenario S1.

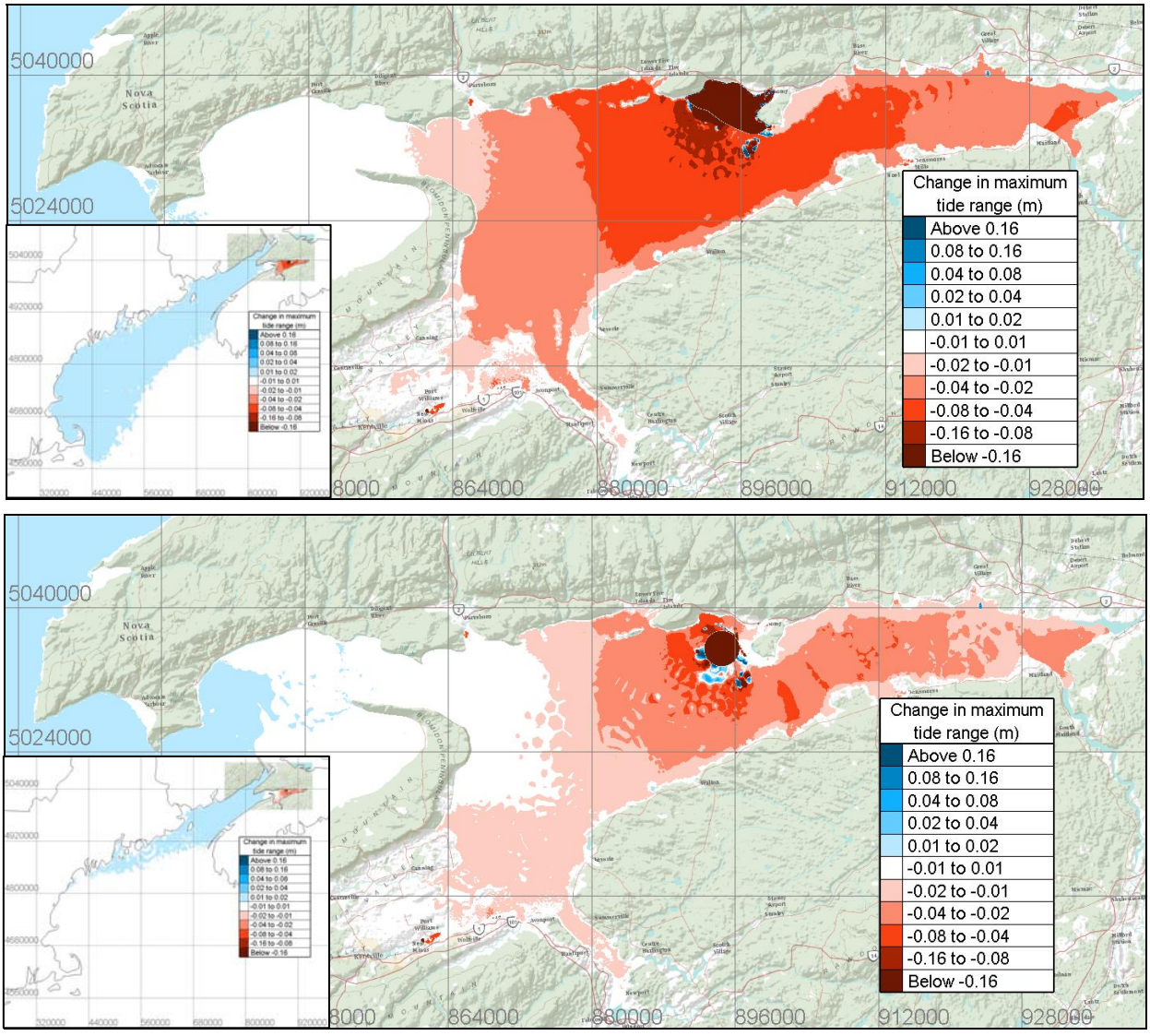

Figure 44. Change in maximum tide range for scenarios S1 and S2.

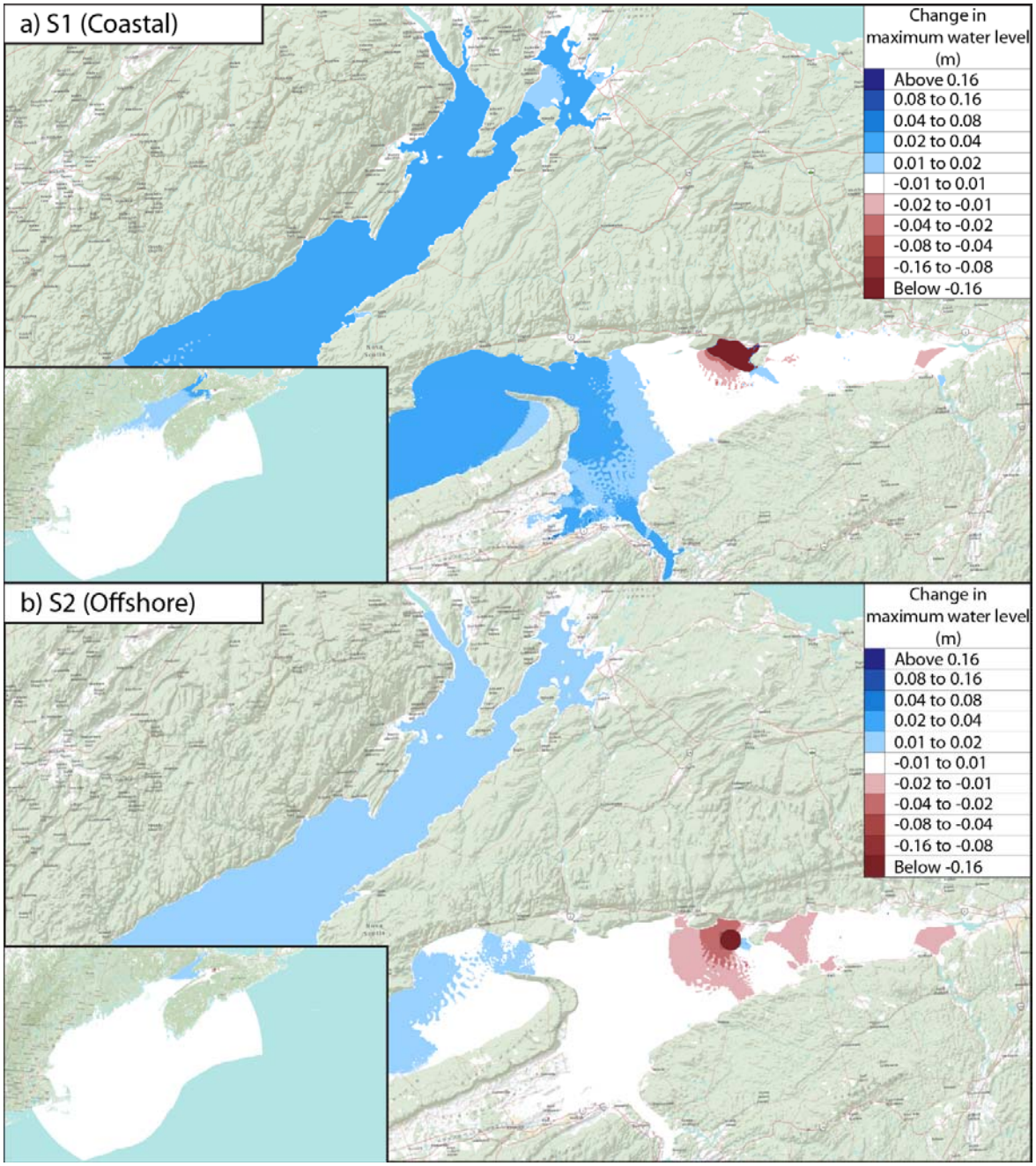

Figure 45. Change in maximum water level for scenarios S1 and S2.

A tidal lagoon will induce local changes in the direction and strength of the tidal currents both within the lagoon and outside it, especially near the powerhouse and along the external perimeter of the impoundment dyke. Depending on seabed conditions, scour protection may be required in these areas to mitigate the high energy flows emerging from the sluice gates and turbines. Scour protection may also be required to stabilize and protect the toe of the impoundment dyke.

Figure 46 shows the depth-averaged velocity field around a 26.7 km^2 coastal lagoon located along the north shore of Minas Basin (scenario S1) that is following a bi-directional operating

scheme. The numerical schematisation of this coastal lagoon is shown in Figure 23b. Figure 46 shows flow patterns during a typical flood tide and during a typical ebb tide. During the flood phase, seawater flows into the lagoon mainly through the turbines (some water also flows through the sluices near the end of the flood stage). Within the lagoon, velocities are highest near the powerhouse, and diminish with increasing distance away from the powerhouse. Outside the lagoon, relatively strong currents occur near the powerhouse and along the southern perimeter of the impoundment dyke. During the ebb phase, seawater flows out of the lagoon mainly through the turbines, although some water also passes through the sluices near the end of the ebb stage. Relatively strong velocities occur near the powerhouse, both inside and especially outside the lagoon. The peak velocities near the powerhouse tend to be stronger during the ebb stage than during the flood; this is due to the shallower water depths outside the lagoon near the end of the ebb phase.

Figure 47 shows the predicted local changes in U_{max} near the coastal and offshore lagoons modelled in scenarios S1 and S2. The vectors in this figure indicate the residual circulation, which is equivalent to the mean current averaged over a long duration. For the coastal lagoon, significant changes in flow speed (ΔU_{max} more than 10 cm/s) are confined to the local area around the lagoon and within the lagoon. It can be seen that, relative to present conditions, flow speeds are significantly greater near the powerhouse outside the lagoon. There is also a large area in the south-eastern part of the lagoon where speeds are reduced significantly. It is possible that fine sediments may tend to accumulate in this area because of these lower velocities. Increased sedimentation is obviously undesirable as this may cause the lagoon to silt up over time. If significant sediment deposition occurs, some intervention may be required to either prevent sediment from settling, or remove the sediment after it has deposited.

Figure 48 shows the predicted far-field changes in U_{max}, relative to existing conditions, for scenarios S1 and S2. At the center of Minas Passage, the maximum current speed is predicted to decrease by approximately 3.5 cm/s for scenario S1 and by approximately 2 cm/s for scenario S2. The tidal currents in distant locations beyond Minas Passage are virtually unchanged by the lagoons in Minas Basin.

Predicted changes in maximum bottom shear stress throughout the upper Bay of Fundy for scenarios S1 and S2 are mapped in Figure 49. The maximum shear stress at Minas Passage is predicted to decrease by 0.4 to 0.8 Pa for scenario S1, and by 0.2 to 0.4 Pa for scenario S2. These reductions are a small fraction of the maximum shear stress for existing conditions, and thus represent relatively small changes. It should be noted that the seabed at Minas Passage is generally comprised of exposed bedrock, and such small changes in shear stress are unlikely to cause significant change to sedimentary processes in the Passage.

The most significant changes in bed shear stress occur near the lagoons, and especially near the powerhouses, where the velocity changes are greatest. The maximum bed shear stress near the coastal lagoon modelled in scenario S1 is predicted to increase by up to 25 Pa, while the maximum bed shear stress near the smaller offshore lagoon is predicted to increase by up to 20 Pa. The sedimentary processes and sediment balances that currently prevail in these areas will likely be significantly altered by such strong changes in flow velocity and bed shear stress. If the local sediments are mobile, or become mobile, they will be scoured and transported away to be deposited elsewhere where the flows are less energetic. It may be necessary to armour a portion of the seabed adjacent to the powerhouse in order to control the scouring and erosion.

Significant reductions in bed shear stress are also predicted near the lagoons, particularly at certain locations within the impoundments. Such decreases suggest that sediments in these areas will be less mobile than before, and suggest that the rate of deposition may exceed the rate of erosion, leading to accretion of sediments and siltation. In this case, some intervention may be required to prevent the lagoon from silting up over time.

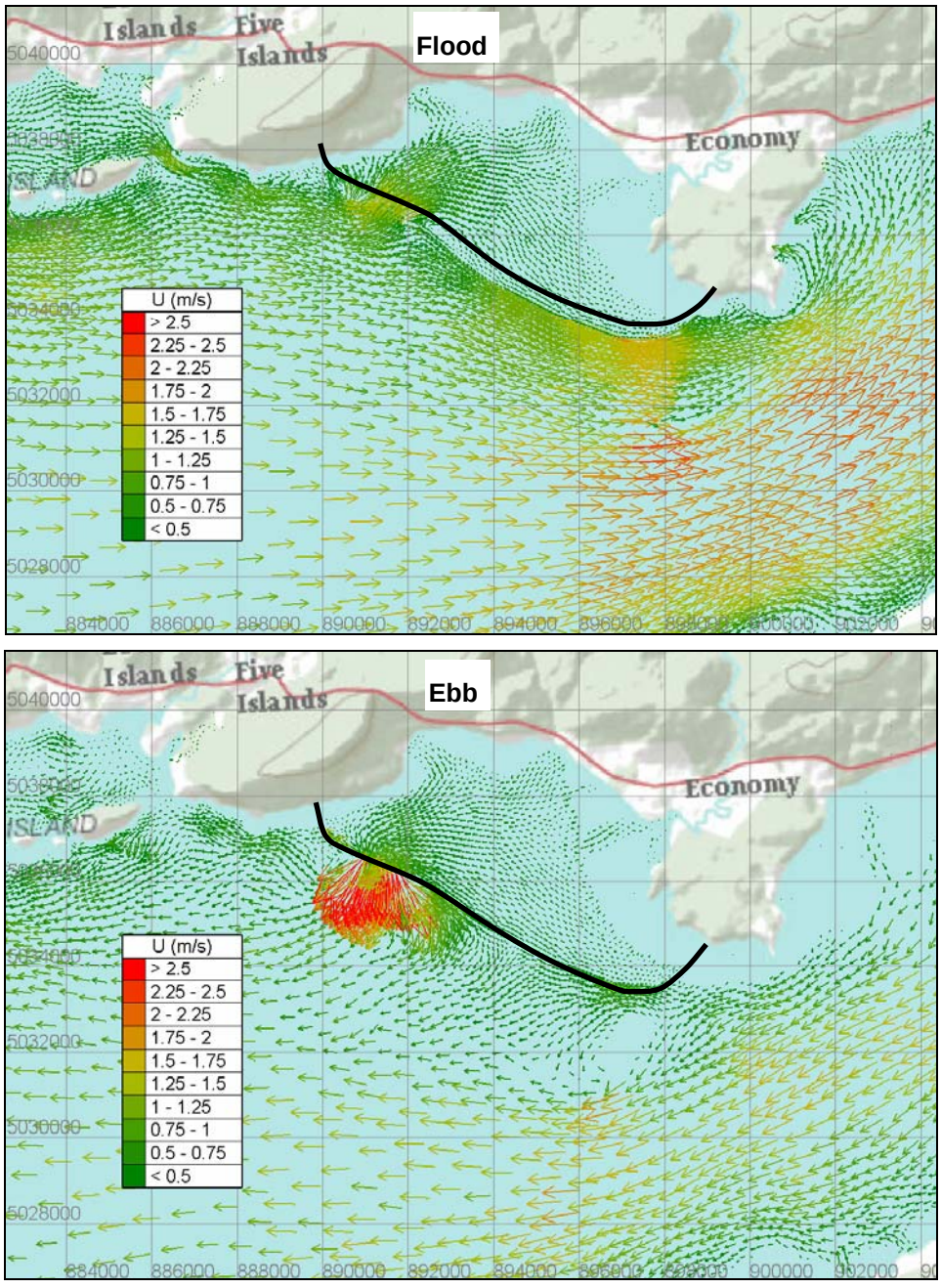

Figure 46. Velocity field near a 26.7 km^2 coastal lagoon during a) flood and b) ebb (2-way generation).

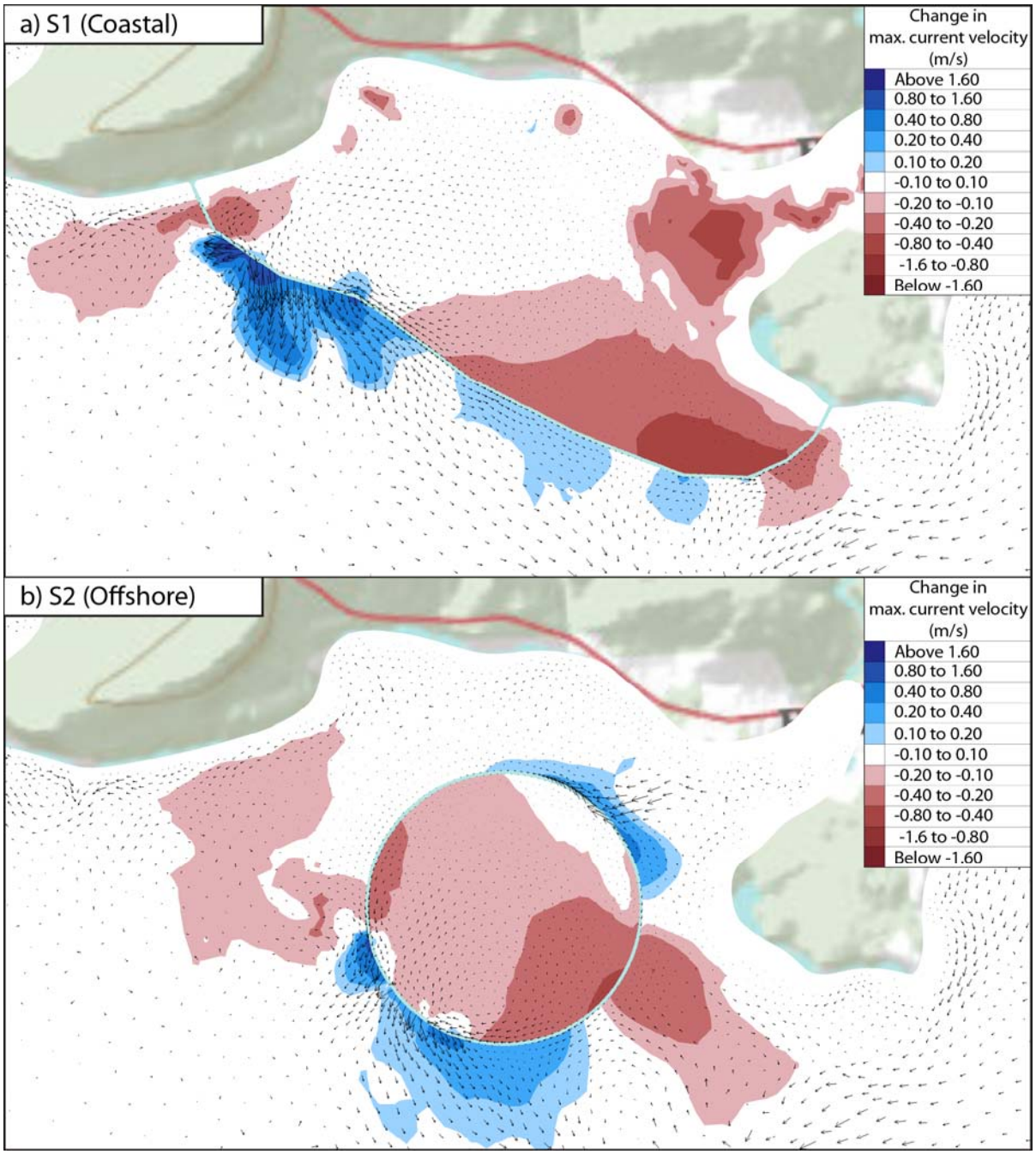

Figure 47. Local change in U_{max} and residual circulation for scenarios S1 and S2.

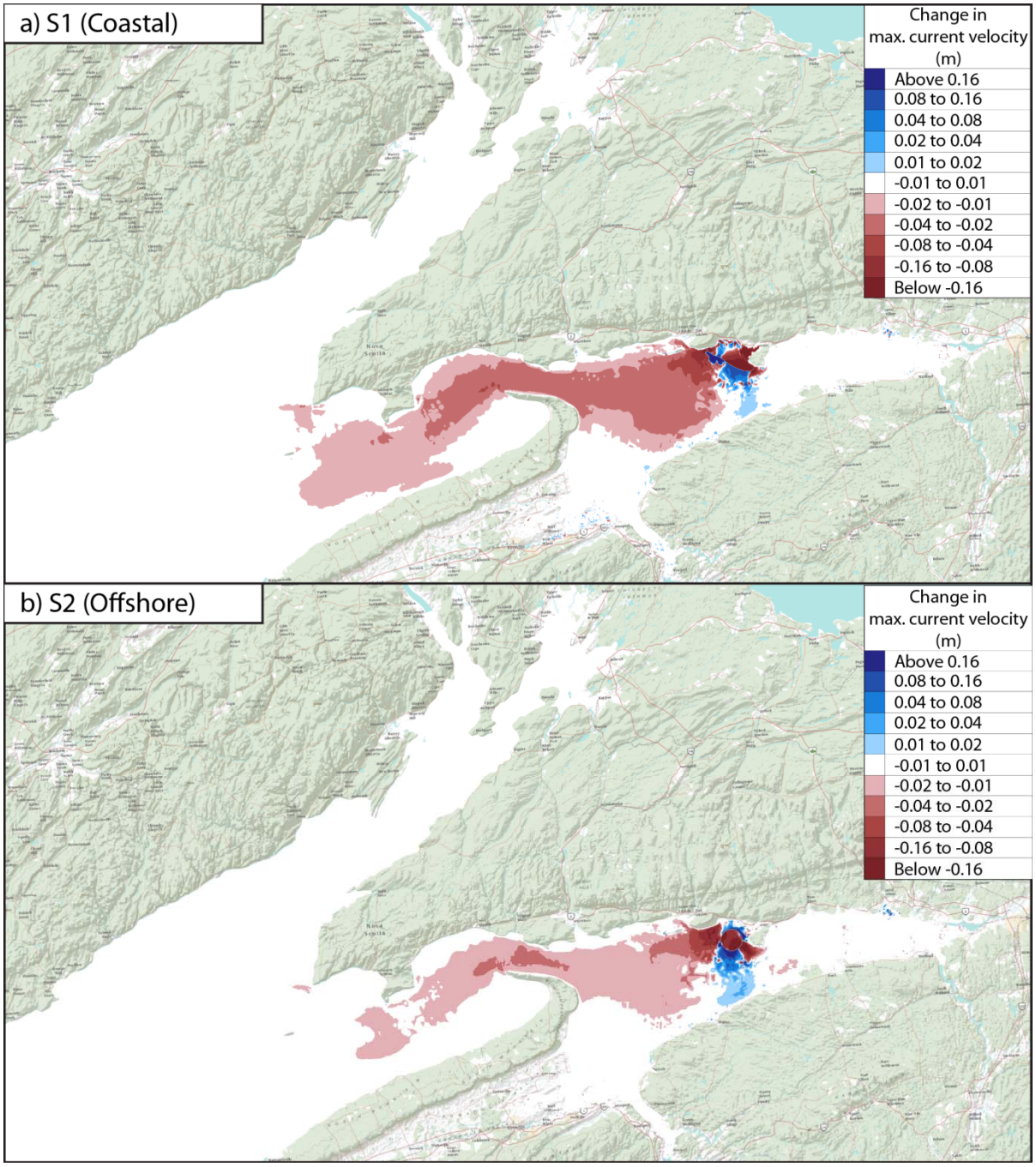

Figure 48. Far-field change in U_{max} for scenarios S1 and S2.

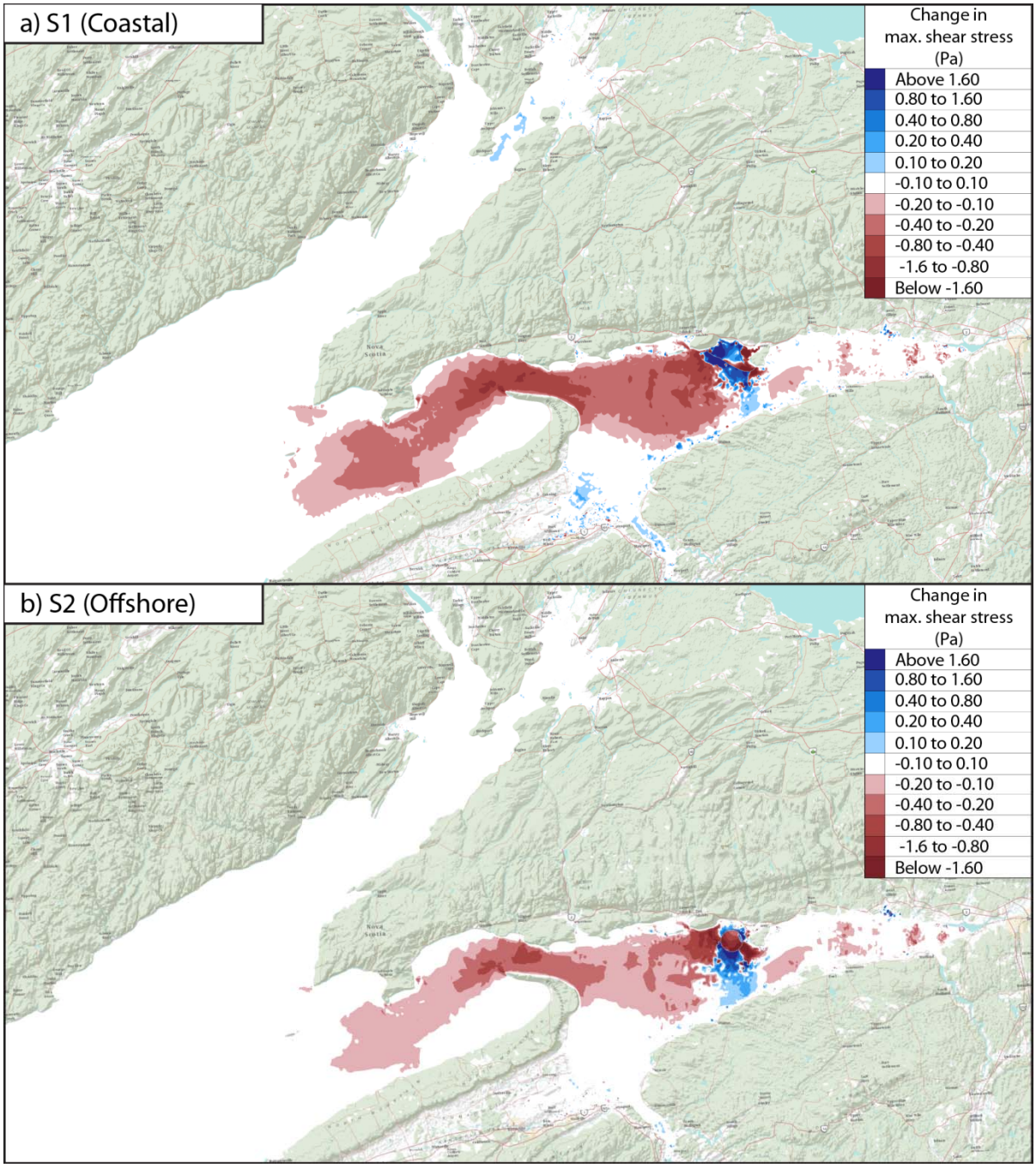

Figure 49. Predicted change in maximum bed shear stress for scenarios S1 and S2.

5.3 Influence of Operating Mode, Scenarios S3-S7

In scenarios S3 to S7, a single 26.7 km^2 coastal lagoon located at site A was modelled in each case. Only the operating mode was varied, everything else remained constant. Two-way generation was simulated in scenario S3, ebb-generation was simulated in scenario S4, and flood-generation was simulated in scenario S5. These operating modes are described in more detail in Section 3.2. In scenario S6, the turbines gates were always closed while the sluice gates were always fully open. In scenario S7, both the turbines and sluices were closed for full duration of the simulation.

The time-varying power outputs for scenarios S3, S4 and S5 are compared graphically in Figure 50. In this figure the power output computed from the finite-element modelling is compared with the power output produced by the analytic model of plant operations (the "box" model) described in Section 3.4. For both flood-generation and ebb-generation, only one power generation cycle occurs per tide cycle; whereas for 2-way generation, there are two power generation cycles per tide cycle. No power is generated in scenarios S6 and S7.

Figure 51 compares the predicted changes in maximum tide range for scenarios S3-S7. These results indicate that the far-field changes in tide range are similar for the three power generating modes (S3-S5). For each case, the maximum tide range at Minas Passage is increased by ~4 cm relative to existing conditions. The maximum tide range at Boston is increased by ~1 cm. For scenarios S3 and S4 (2-way generation and ebb-generation), small decreases in tide range are predicted for some parts of eastern Minas Basin; whereas no reductions in tide range in eastern Minas Basin are predicted for scenario S5 (flood generation).

For scenario S6, where the turbine gates are always closed and the sluices are always open, the maximum tide range in Minas Basin decreases by 2 to 8 cm and increases by 1 to 2 cm for parts of the Gulf of Maine and the lower Bay of Fundy. For scenario S7, where all turbine gates and sluices remain closed for the entire simulation, the maximum tide range increases by 4 to 8 cm over the entire upper BoF, increases by 2 to 4 cm in the lower BoF, and increases by 1 to 2 cm in the Gulf of Maine.

By far the largest changes in water levels occur within the lagoon itself, where the tide range is reduced by several meters, relative to existing conditions. The exact tide range reduction depends on the operating mode and on the characteristics of the turbines and sluices. The estimated reduction in tide range within the lagoon is around 6.3 m for scenario S3, 7.5 m for scenario S4, 4.7 m for scenario S5, and 3.0 m for scenario S6. For scenario S7, the water level within the lagoon does not fluctuate since both the turbines and sluices are assumed to be closed for the entire simulation.

Figure 52 compares the predicted far-field changes in RMS velocity, U_{RMS}, for scenarios S3 to S7; while Figure 53 compares the predicted changes in maximum velocity, U_{max}, near the lagoon for these same five scenarios. The predicted far-field changes in flow velocity are quite similar for each of these five scenarios. Or in other words, the generation mode has a very weak influence on far-field tidal currents. The flow velocities at Minas Passage will be approximately 2 to 4 cm/s slower than for existing conditions. Tidal currents outside Minas Basin are very weakly affected if at all.

As seen in Figure 53, the generation mode has a strong and complicated influence on the pattern and strength of the currents near the lagoon. The most noticeable velocity changes occur near the lagoons, both inside and outside the impoundment dikes. Within the lagoon, compared to existing conditions, peak velocities are generally higher near the powerhouse and lower in other regions within the impoundment. Outside the lagoon, compared to existing conditions, peak velocities tend to amplify near the powerhouse and in certain areas near the perimeter of the impoundment, while peak velocities are attenuated in other areas.

The largest velocity increases are predicted to occur outside the powerhouse, adjacent to the sluices and turbines. The peak velocities outside the powerhouse tend to be larger than the peak velocities within the lagoon, because, during the transition from ebb to flood, the external water level is lower than the internal water level. Hence, the external velocities tend to be higher because the water depth is shallower.

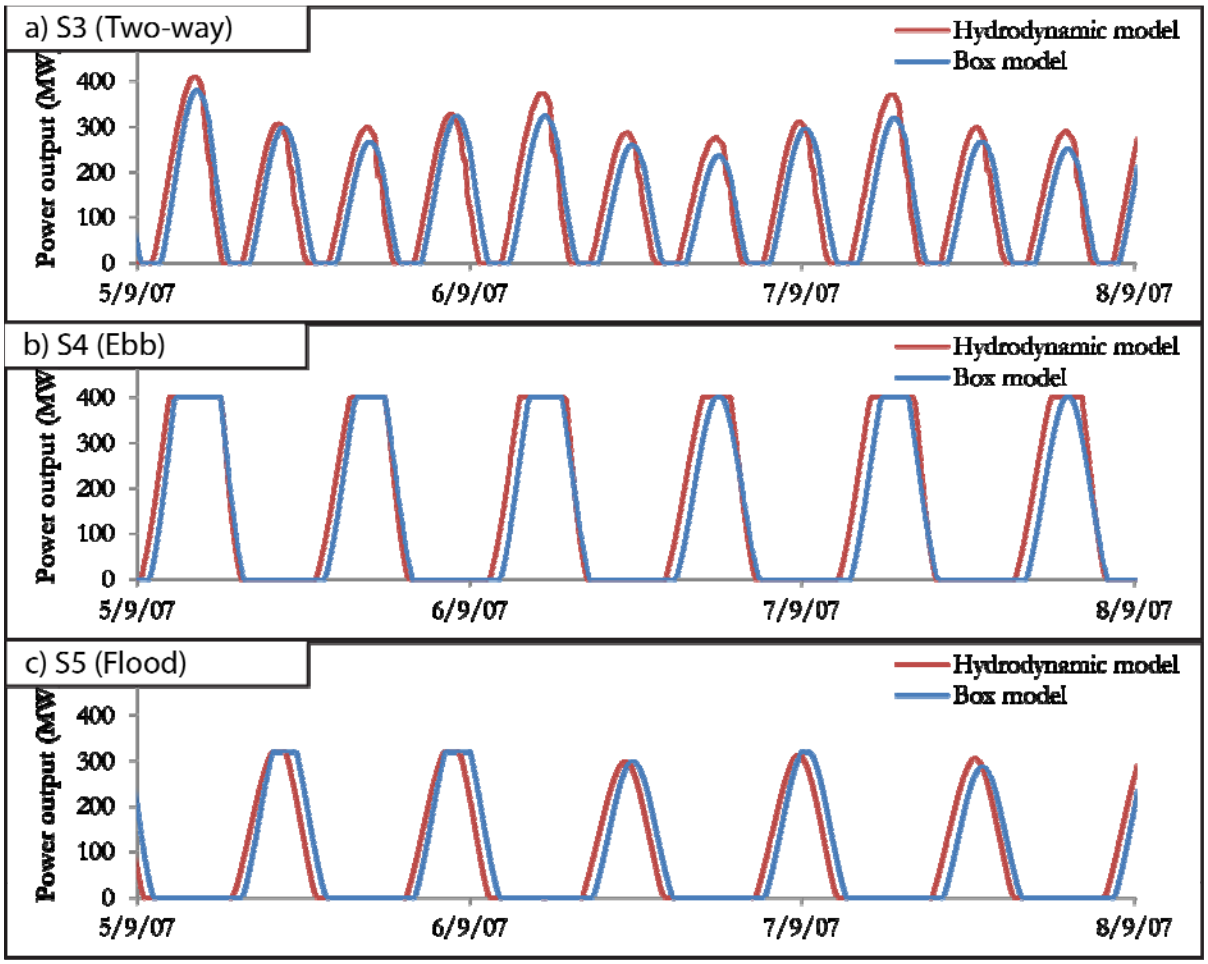

Figure 50. Power output for scenarios S3-S5.

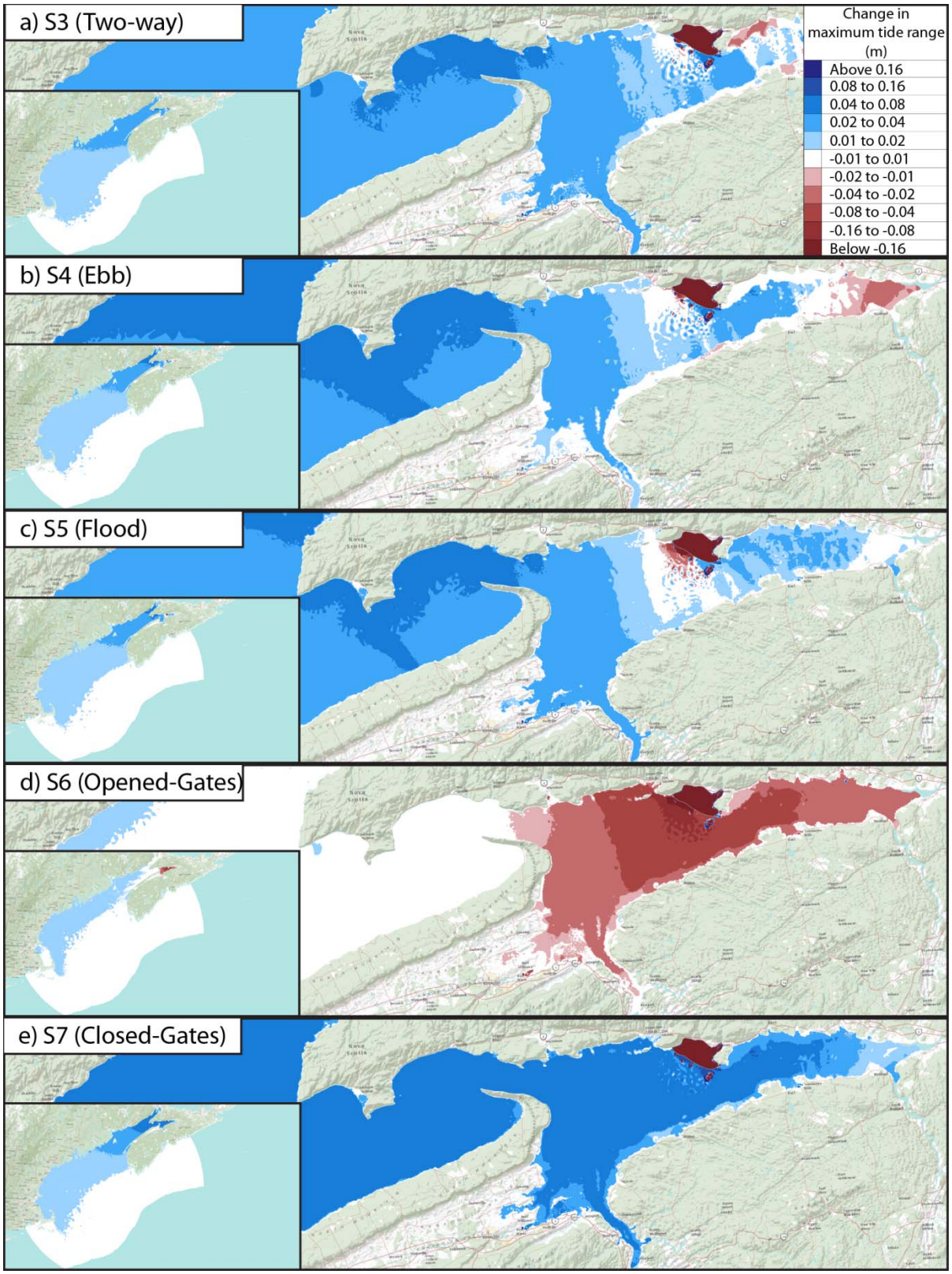

Figure 51. Change in maximum tide range for scenarios S3-S7.

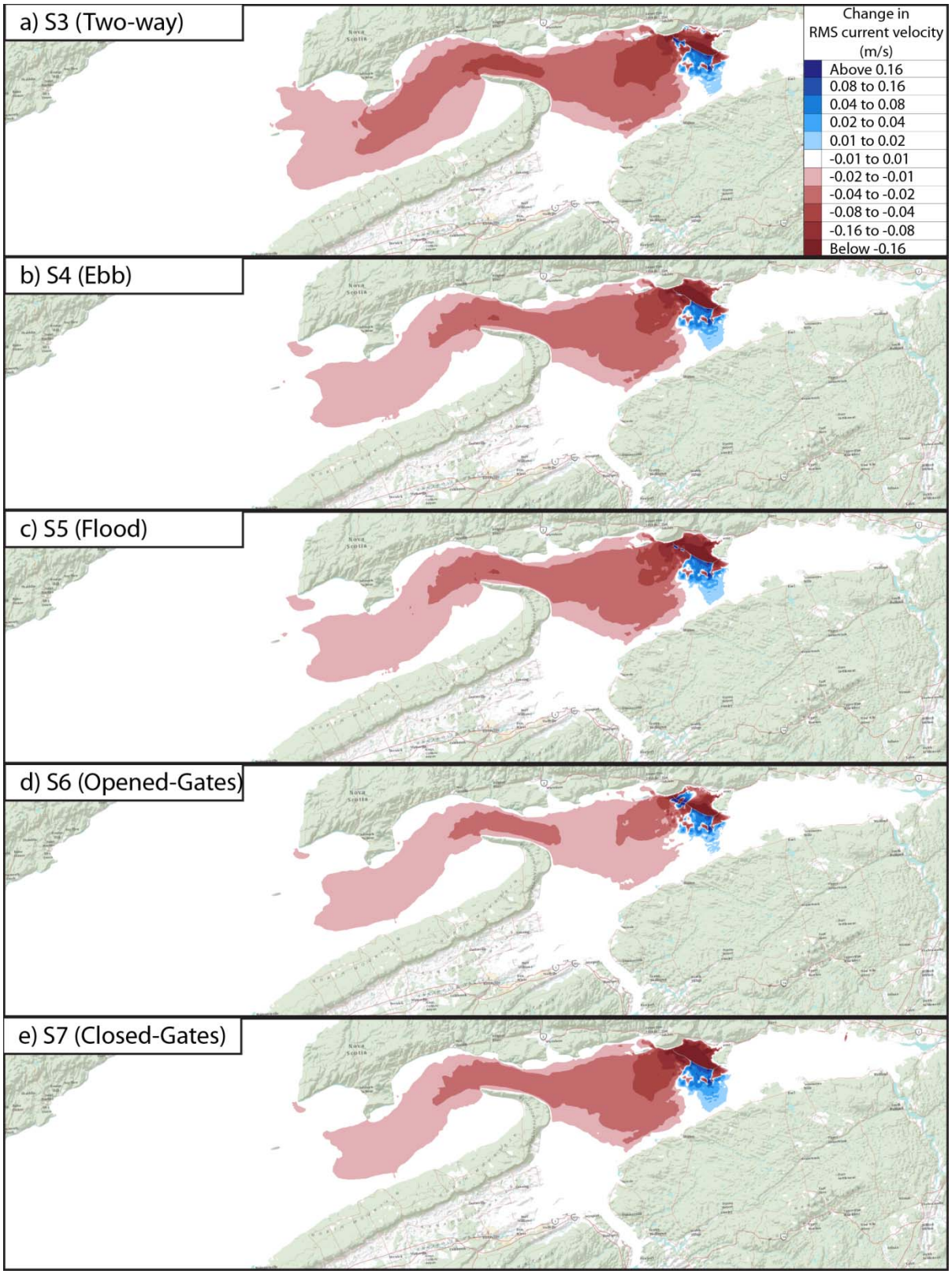

Figure 52. Change in U_{RMS} for scenarios S3-S7.

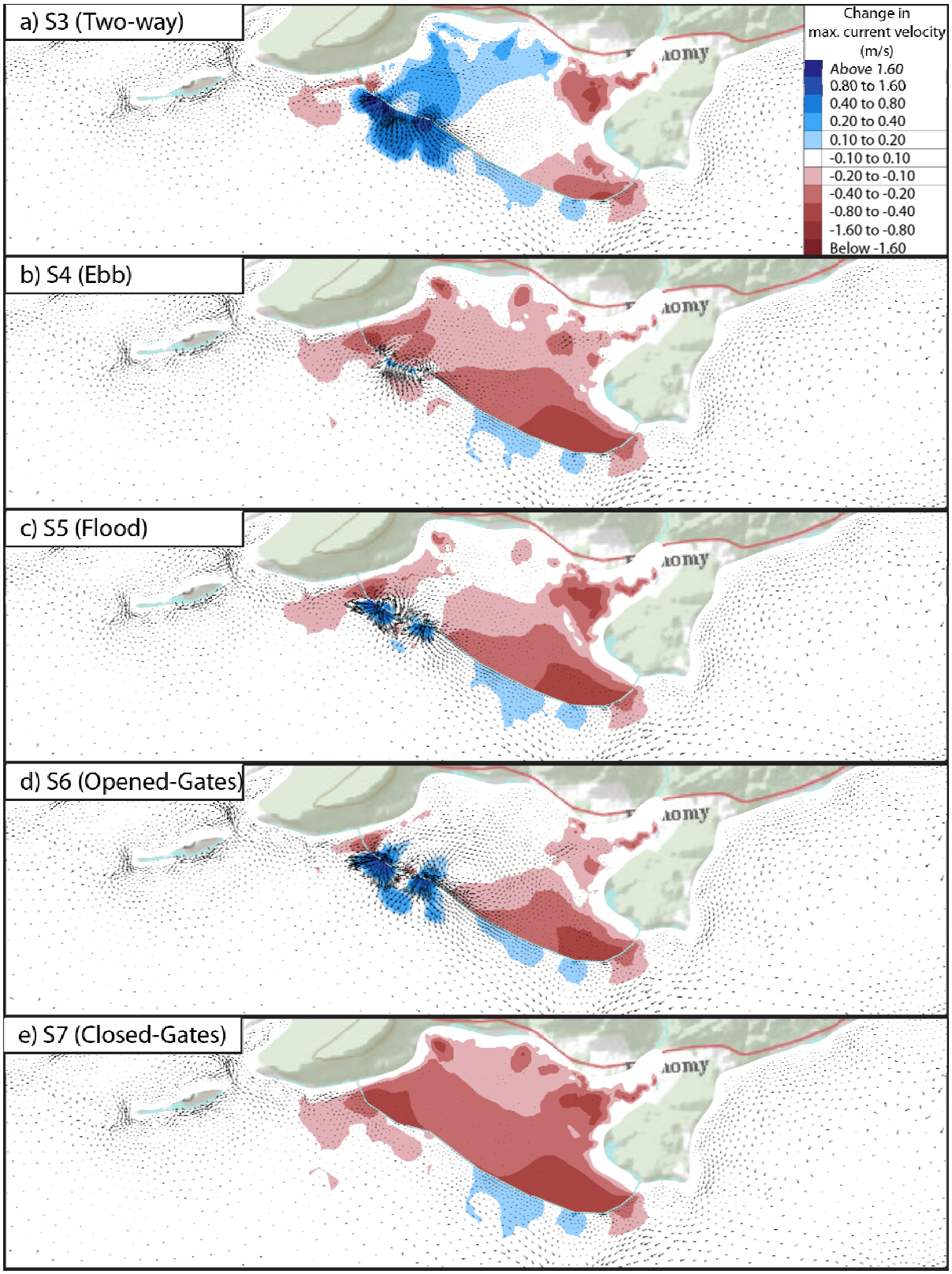

Figure 53. Change in U_{max} and residual circulation for scenarios S3-S7.

5.4 Influence of Lagoon Size, Scenarios S3, S8-S12

The influence of lagoon size on hydrodynamic impact can be assessed by comparing results for scenarios S3, S8 and S9, where coastal lagoons of various sizes were modelled at site A; and for scenarios S10-S12, where offshore lagoons of differing size were modelled at site A. In what follows, results for the coastal lagoons will be considered first, followed by results for the offshore lagoons.

The smallest coastal lagoon, considered in scenario S3, has an area of 26.7 km^2, the medium sized coastal lagoon considered in scenario S8 has an area of 35.1 km^2, while the large coastal lagoon modelled in scenario S9 has an area of 57.7 km^2 (all areas computed at mean sea level). The predicted changes in maximum tide range for these three scenarios are compared in Figure 54. It can be seen that the pattern of the change in tide range is similar for all three cases, but the magnitude of the change increases with increasing lagoon size. At Minas Passage, the increases in maximum tide range for scenarios S3, S8 and S9 are approximately 4 cm, 6 cm and 9 cm, respectively. At Boston, the increases in maximum tide range for scenarios S3, S8 and S9 are approximately 1.4 cm, 2.5 cm and 4.3 cm, respectively.

Figure 55 compares the predicted far-field changes in RMS velocity, U_{RMS}, for scenarios S3, S8 and S9 while Figure 56 compares the predicted changes U_{RMS} near the lagoon for these same three scenarios. It can be seen that the pattern of the far-field change in tidal current velocity is identical for all three cases, but the magnitude of the change increases slightly with increasing lagoon size.

The patterns of the local changes in tidal current speed are also similar for the three cases, except that the area over which significant changes in tidal hydrodynamics are predicted to occur grows with increasing lagoon size. The most significant velocity increases are found near the powerhouse, adjacent to the sluices and turbines. It is worth noting that the powerhouse was assumed to be 2 km long in all cases, while the number of turbines and sluices increases with increasing lagoon size, as shown in Table 6. As a result, the numerical turbines and sluices in the larger lagoons are concentrated closer together than those in the smaller lagoons. Hence, the intensity of the flows near the powerhouse will be higher for the larger lagoons compared with the smaller lagoons. For this reason, the magnitude of the flows near the powerhouse may not be entirely realistic and should therefore be interpreted with caution.

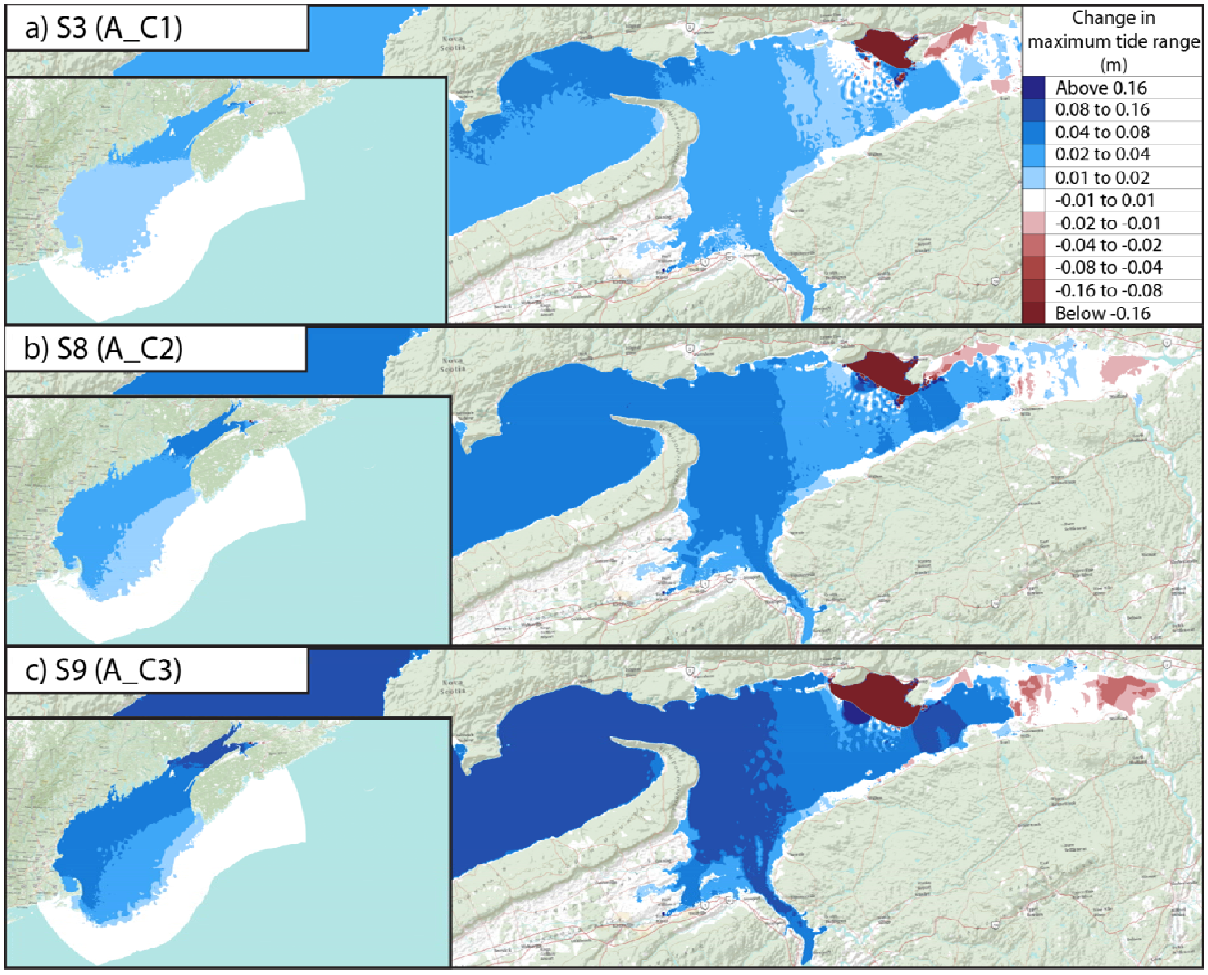

Figure 54. Change in maximum tide range for scenarios S3, S8 and S9.

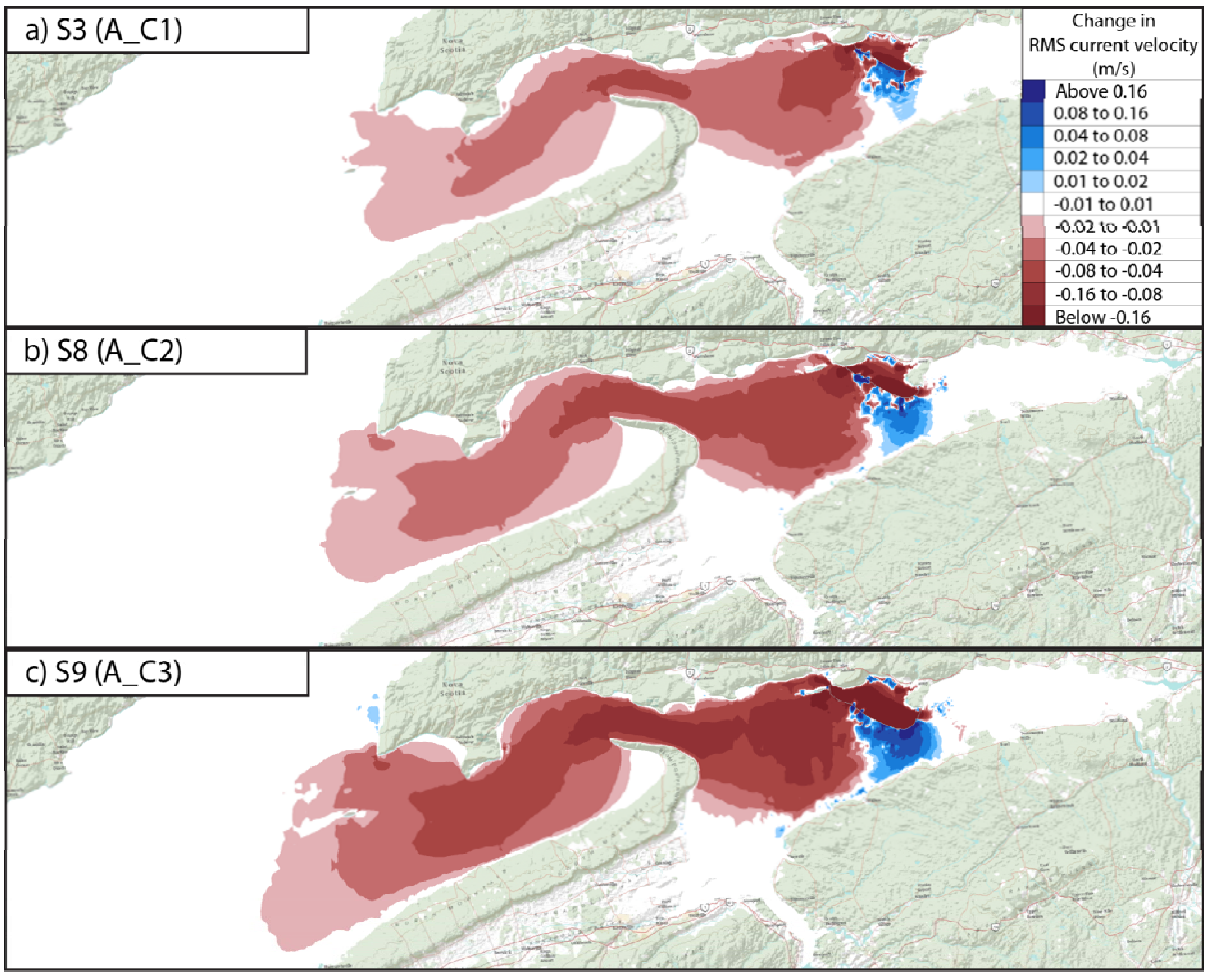

Figure 55. Far-field change in U_{RMS} for scenarios S3, S8 and S9.

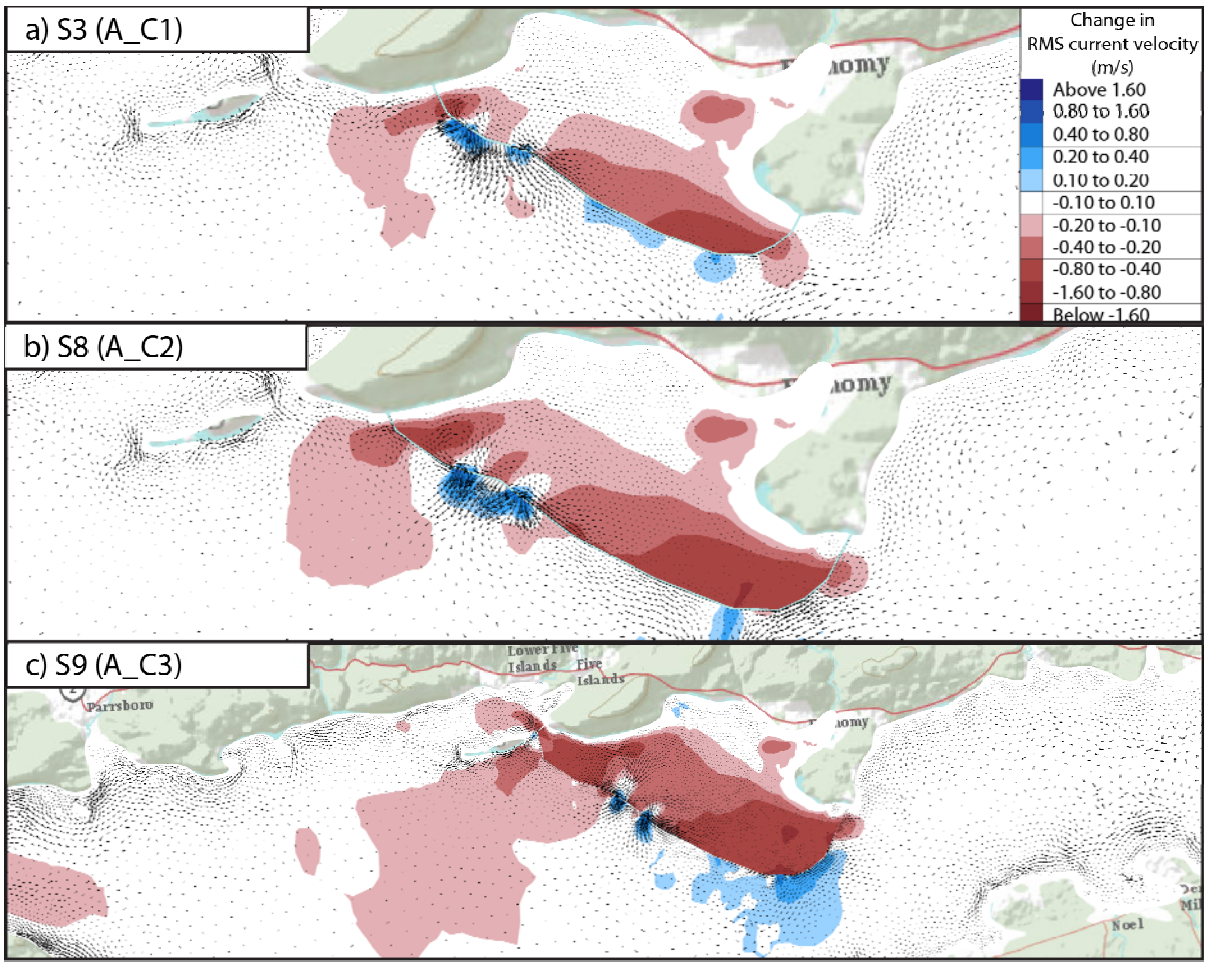

Figure 56. Local change in U_{RMS} and residual current for scenarios S3, S8 and S9.

The smallest offshore lagoon, considered in scenario S10, has an area of 12 km^2, the medium sized offshore lagoon considered in scenario S11 has an area of 18 km^2, while the large offshore lagoon modelled in scenario S12 has an area of 24 km^2 (all areas computed at mean sea level). The predicted changes in maximum tide range for these three scenarios are compared in Figure 57. It can be seen that the pattern of the change in tide range is similar for all three cases, but the magnitude of the change increases with increasing lagoon size. At Minas Passage, the increases in maximum tide range for scenarios S10, S11 and S12 are approximately 1 cm, 2 cm and 4 cm, respectively. At Boston, the increases in maximum tide range for scenarios S10, S11 and S12 are approximately 1.1 cm, 1.4 cm and 2.0 cm, respectively.

Figure 58 compares the predicted far-field changes in RMS velocity, U_{RMS}, for scenarios S10 – S12 while Figure 59 compares the predicted changes U_{RMS} near the lagoon for these same three scenarios. It can be seen that the pattern of the far-field change in tidal current velocity is similar for all three cases, but the magnitude of the change increases slightly with increasing lagoon size. For example, the predicted reductions in depth-averaged current speed at the center of Minas Passage for scenarios S10, S11 and S12 are approximately 2.8 cm/s, 4.8 cm/s and 6.6 cm/s, respectively. Virtually no change in tidal current speed is predicted in the lower Bay of Fundy or the Gulf of Maine for these scenarios.

The patterns of the local changes in tidal current speed are also similar for the three cases, except that the area over which significant changes in tidal hydrodynamics are predicted to occur grows with increasing lagoon size. Within the lagoons, velocities are reduced by up to ~60 cm/s compared to existing conditions. As mentioned previously, this could lead to increased sediment deposition within the lagoon. Outside the lagoon, velocities are increased in some areas and reduced in others. The most significant velocity increases occur outside the lagoon near the powerhouse and along the perimeter of the dyke. It should be remembered that the magnitude of the flows near the powerhouse may not be entirely realistic and should therefore be interpreted with caution.

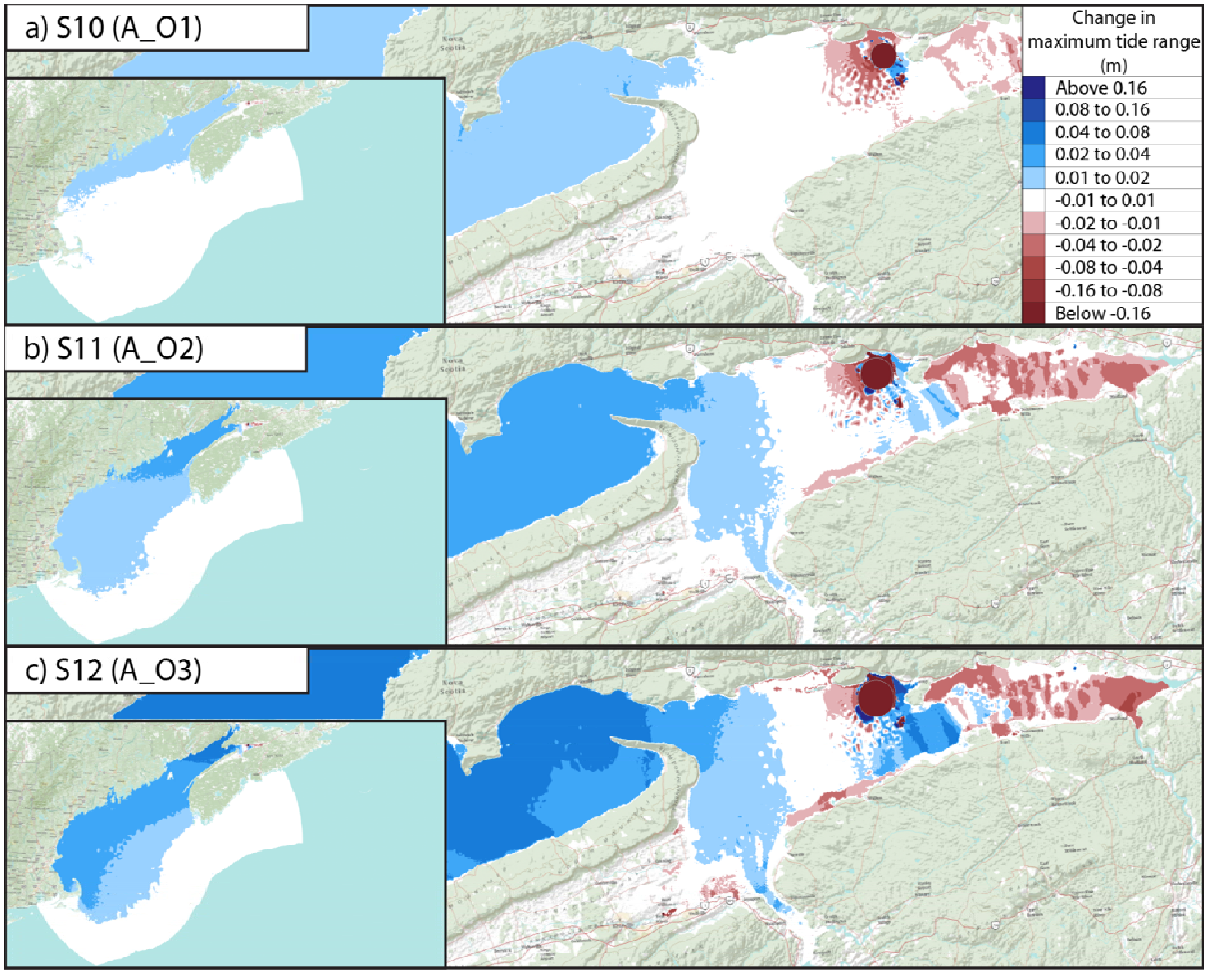

Figure 57. Change in maximum tide range for scenarios S10-S12.

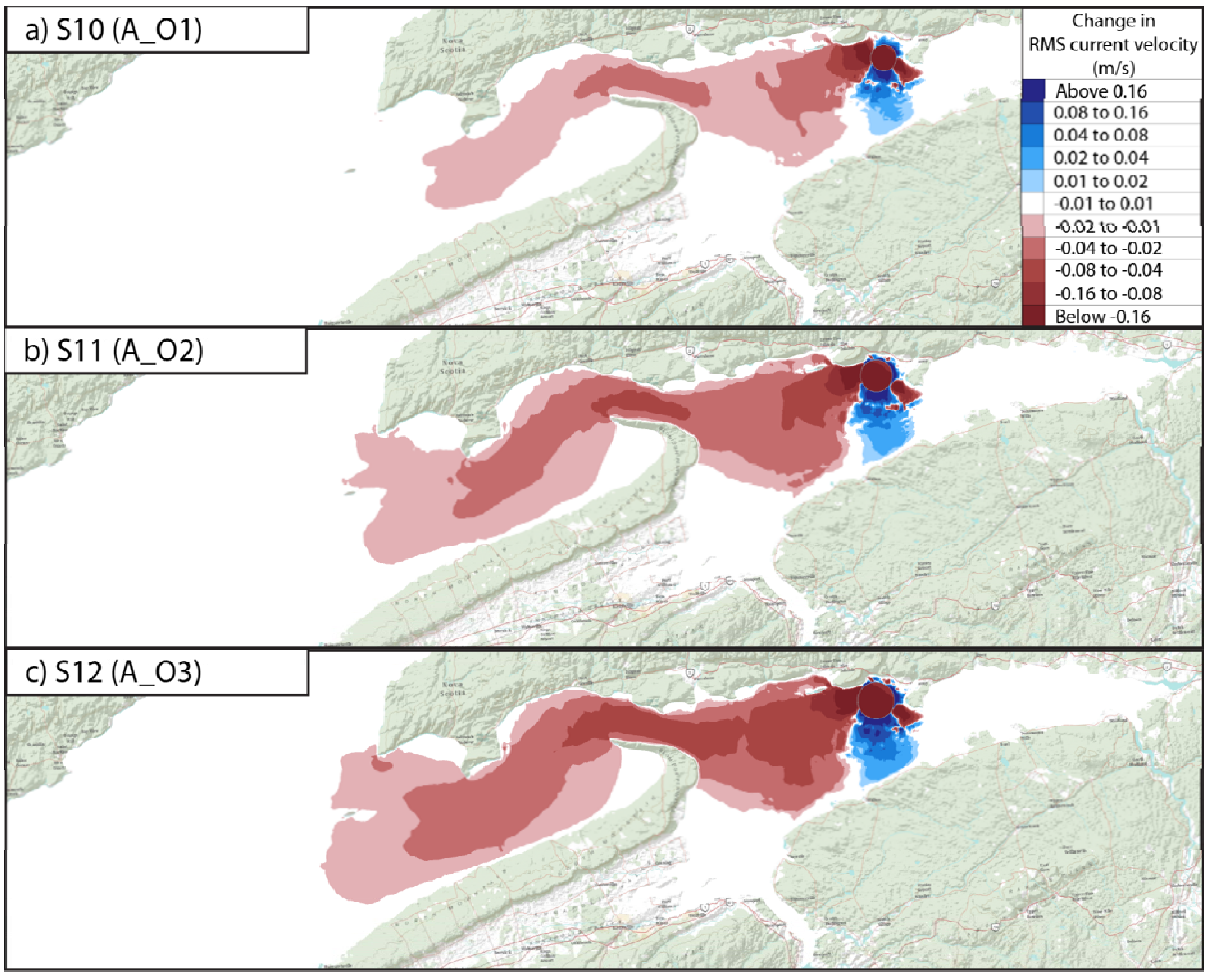

Figure 58. Far-field change in U_{RMS} for scenarios S10-S12.

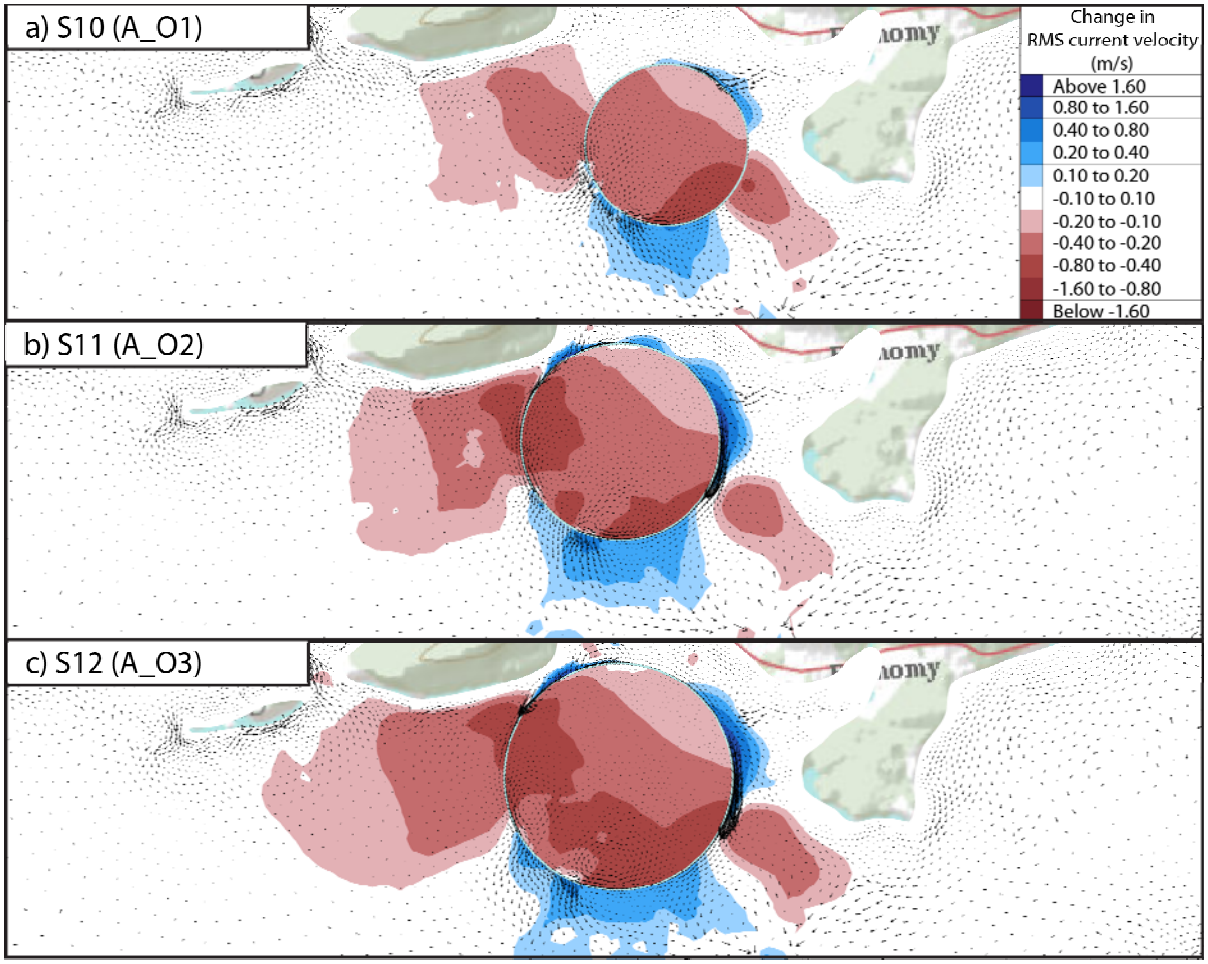

Figure 59. Local change in U_{RMS} and residual current for scenarios S10-S12.

5.5 Influence of Lagoon Location, Scenarios S3, S13, S14

The influence of lagoon location on tidal hydrodynamics can be assessed by comparing results for scenarios S3, S13 and S14. In these three scenarios, similarly-sized coastal lagoons were modelled at three different sites within Minas Basin (sites A, B and C).

The predicted change in maximum tide range for scenarios S3, S13 and S14 are compared in Figure 60. These results show that lagoon location has a strong influence on the resulting hydrodynamic impact. In terms of the change in the tide range at Boston, the impact due to scenario S14 (34 km^2 coastal lagoon in the southern part of Minas Basin at site C) is roughly 50% greater than the impact due to scenarios S3 or S13.

Compared to existing conditions, the maximum tide range for scenario S14, where the lagoon is located in the southern part of Minas Basin, is predicted to increase by from 2 to 4 cm throughout Chignecto Bay, the lower BoF and the Gulf of Maine. In Minas Basin, the tide range is either unaffected or reduced slightly, relative to existing conditions.

The impact of scenario S13, where the lagoon is located in the eastern part of Minas Basin at site B, is markedly different. In this case, the maximum tide range in Minas Basin is predicted to be up to 16 cm larger than for existing conditions. A 4 to 8 cm increase in maximum tide range is predicted for Chignecto Bay and the upper BoF, excluding Minas Basin. Increases ranging from 1.5 to 4 cm are predicted along the Gulf of Maine shoreline.

The pattern of change is again different for scenario S3, where the lagoon is located in the northern part of Minas Basin at site A. In this case, the maximum tide range in the western part of Minas Basin is predicted to be up to 4 cm larger, while the tide range in the eastern part of Minas Basin is predicted to be up to 4 cm smaller than for existing conditions. A 2 to 4 cm increase in maximum tide range is predicted for Chignecto Bay and the upper BoF, excluding Minas Basin. Small increases in maximum tide range on the order of 1.5 cm are predicted along the Gulf of Maine shoreline.

The predicted changes in far-field RMS velocity for scenarios S3, S13 and S14 are compared in Figure 61. The predicted changes within Minas Basin are quite different due to the different lagoon locations considered in each scenario. Outside Minas Basin, the pattern of velocity change for these three scenarios is generally similar, while the magnitude of the velocity change is slightly larger for scenario S14 than for the other two. No appreciable changes in velocity are predicted for Chignecto Bay, the lower BoF and the GoM for any of these three scenarios.

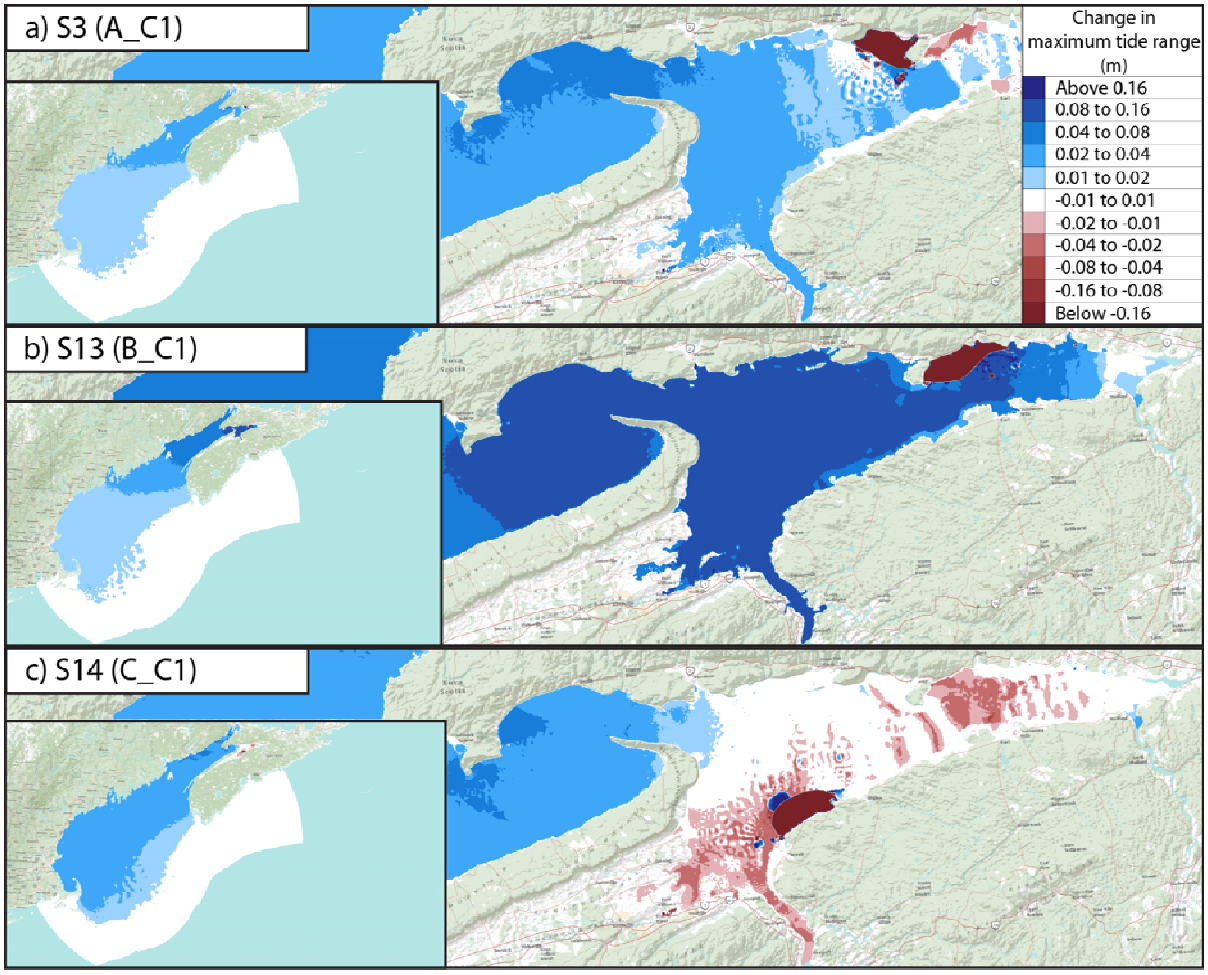

Figure 60. Change in maximum tide range for scenarios S3, S13 and S14.

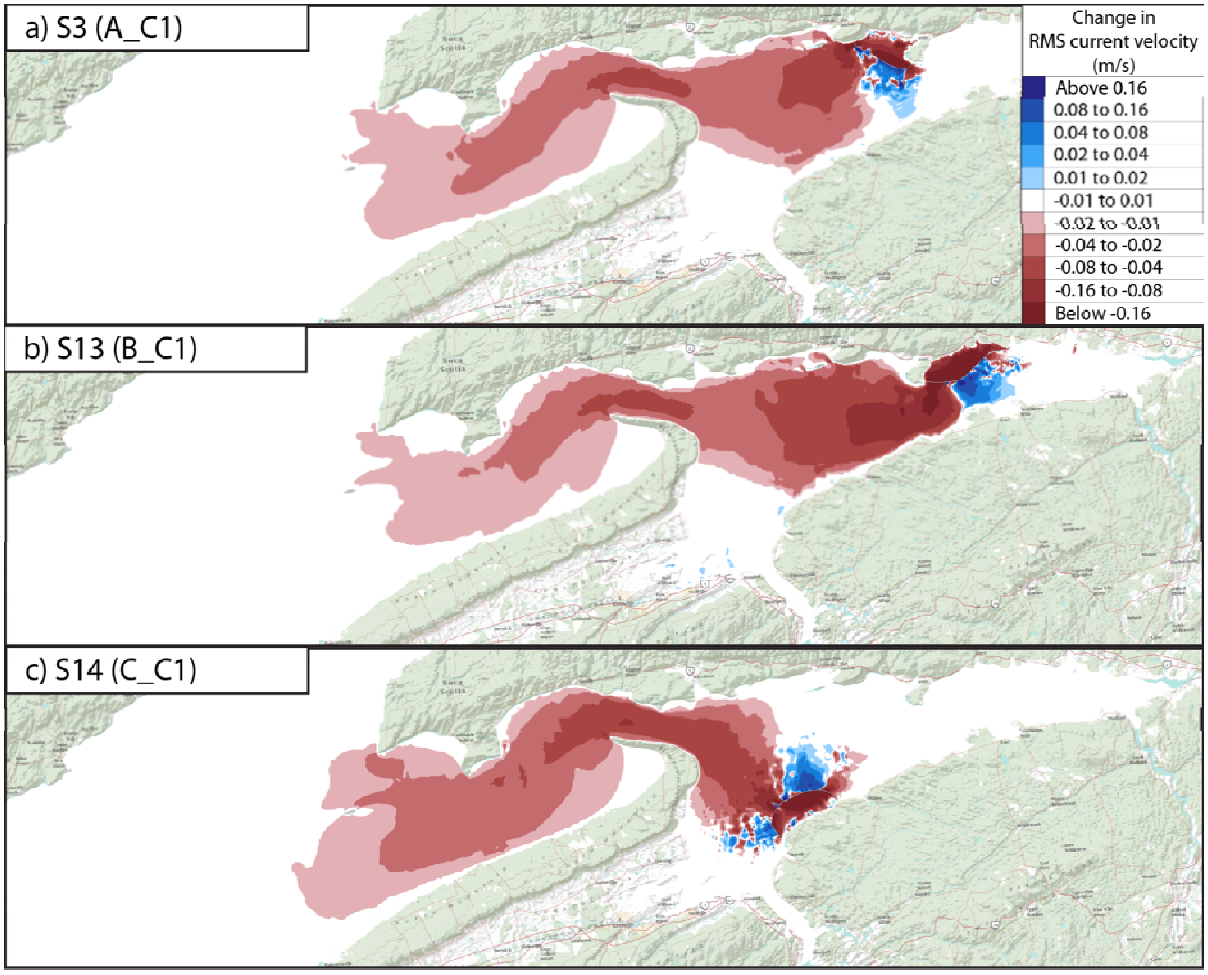

Figure 61. Far-field change in U_{RMS} for scenarios S3, S13 and S14.

5.6 Three Lagoons in Minas Basin, Scenarios S15, S16

Three coastal lagoons located in Minas Basin at sites A, B and C were modelled in scenario S15, while three smaller offshore lagoons at the same sites were modelled in scenario S16. The total area of the three coastal lagoons (94.8 km^2) is approximately 2.6 times the combined area of the three offshore lagoons (36 km^2). Numerical predictions of the change in maximum tide range, relative to existing conditions, for these two scenarios are compared in Figure 62. The scale of the hydrodynamic impacts due to the three coastal lagoons are clearly larger than the impacts due to the three smaller offshore lagoons, and this significant difference can be attributed mainly to the differences in lagoon size and power output between the two scenarios.

Widespread but modest increases in maximum tide range are predicted for scenario S15. Modest increases in tide range are predicted over the entire GoM and BoF, except for the far eastern part of Minas Basin, where the status quo will prevail. Increases greater than 16 cm are predicted at Minas Passage for scenario S15.

The predicted changes in maximum tide range for scenario S16 are also widespread, but smaller in magnitude. The tide range at Minas Passage is predicted to increase by ~4 cm for scenario S16. Increases on the order of 3 to 4 cm are predicted along the shore of the GoM, while increases ranging from 4 to 8 cm are predicted for the upper BoF, including most of Chignecto Bay, but excluding Minas Basin. For eastern parts of Minas Basin, reductions in maximum tide range ranging from 2 to 8 cm are predicted for scenario S16.

Predicted changes in far-field RMS velocity for scenarios S15 and S16 are compared in Figure 63. The overall pattern of velocity change is similar for these two scenarios; however, the magnitudes of the velocity changes are stronger for scenario S15, where the combined lagoon area is 2.6 times larger. The tidal currents at the center of Minas Passage will be approximately 16 cm/s slower with the three coastal lagoons, and roughly 8 cm/s slower with the three offshore lagoons. It is interesting to note that rather weak increases in velocity (~1 cm/s) are predicted in parts of Chignecto Bay for scenario S15. Aside from this, no appreciable changes in velocity are predicted for the lower BoF and the GoM for either of these two scenarios.

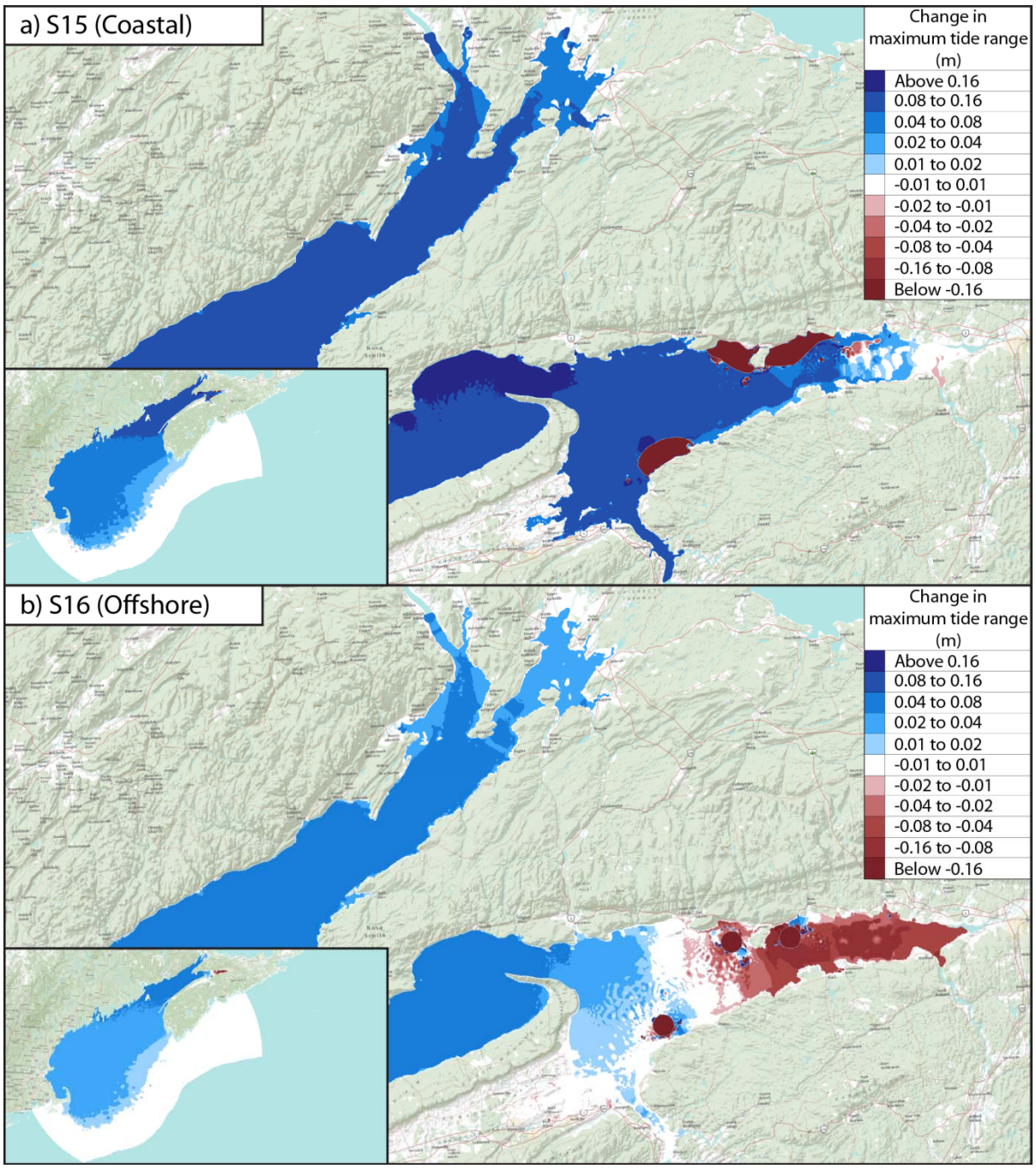

Figure 62. Change in maximum tide range for scenarios S15 and S16.

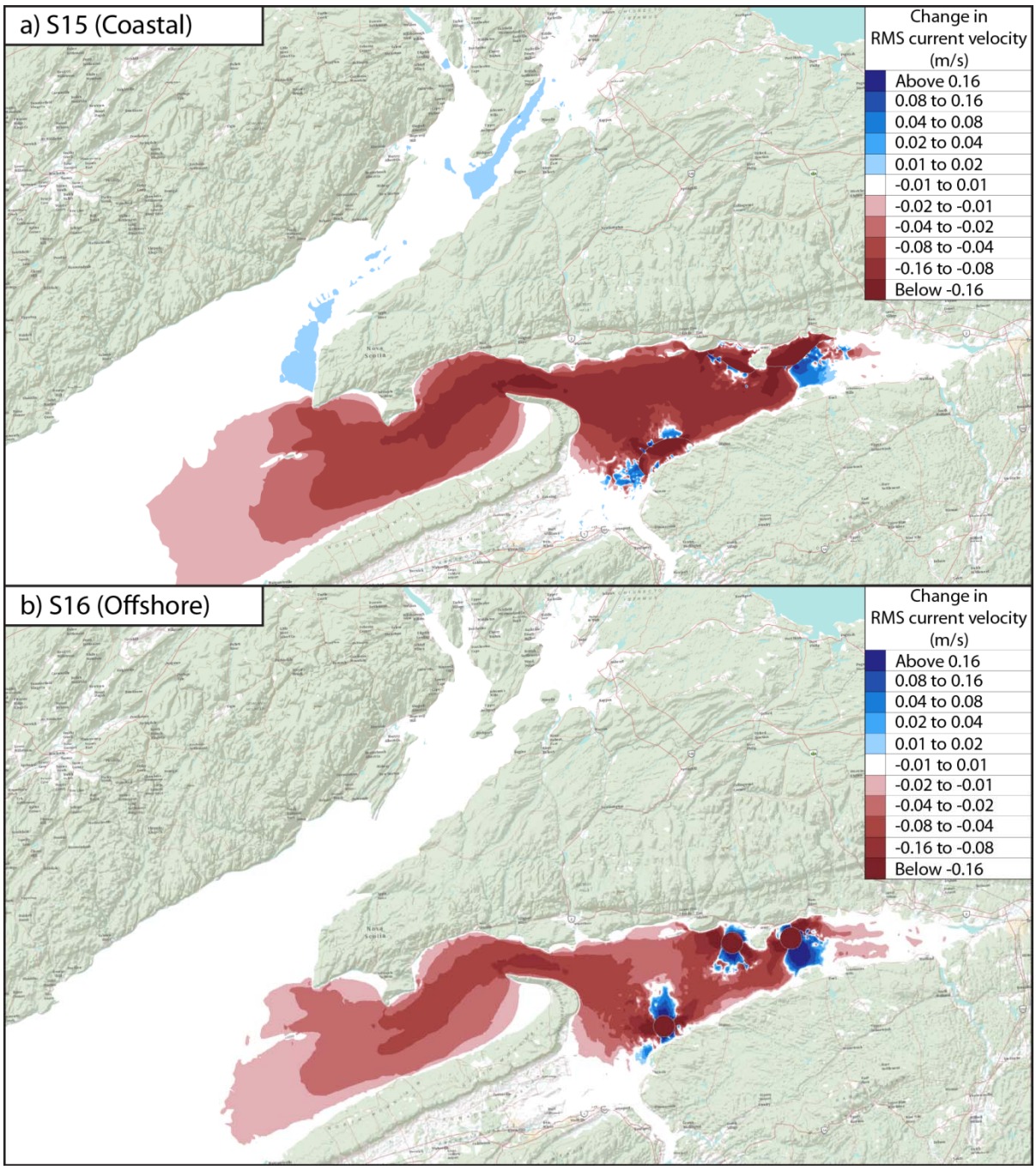

Figure 63. Far-field change in U_{RMS} for scenarios S15 and S16.

5.7 Three Lagoons in Minas Basin, Scenarios S17, S18

Three coastal lagoons located in Chignecto Bay at sites D, E and F were modelled in scenario S17, while three smaller offshore lagoons at the same sites were modelled in scenario S18. The total area of the three coastal lagoons (84.0 km^2) is approximately 2.3 times the combined area of the three offshore lagoons (36 km^2). Numerical predictions of the change in maximum tide range, relative to existing conditions, for these two scenarios are compared in Figure 64. The pattern of the hydrodynamic impacts for these two scenarios is similar, but the scale of the impacts due to the three coastal lagoons is clearly larger than the impacts due to the three smaller offshore lagoons. This difference can be attributed mainly to the differences in lagoon size and power output between the two scenarios. For both scenarios, reductions in tide range are predicted for the upper Bay of Fundy, including Minas Basin and Chignecto Bay, whereas increases in tide range are predicted for the Gulf of Maine. In both cases, virtually no change in tide range is predicted at the entrance to the Bay of Fundy.

For scenario S17, decreases in maximum tide range on the order of 4 to 8 cm are predicted over much of Minas Basin, while reductions ranging from 8 to 16 cm are predicted over much of Chignecto Bay. For the Gulf of Maine shoreline, modest increases in maximum tide range ranging from 4 to 8 cm are predicted for scenario S17.

The predicted changes in maximum tide range for scenario S18 are also widespread, but smaller in magnitude than for scenarios S17. For the Gulf of Maine shoreline, modest increases in maximum tide range on the order of 4 cm are predicted for scenario S18.

Predicted changes in far-field RMS velocity for scenarios S17 and S18 are compared in Figure 65. The overall pattern of velocity change is similar for these two scenarios, however, the magnitudes of the velocity changes are stronger for scenario S17, where the combined lagoon area is 2.3 times larger. It is interesting to note that very weak reductions in velocity (~1 cm/s) are predicted at the center of Minas Passage for both scenarios. Aside from this, no appreciable changes in velocity are predicted in Minas Basin and the Gulf of Maine for either of these two scenarios.

The influence of lagoon location on tidal hydrodynamics can also be assessed by comparing results for scenarios S15, described in Section 5.6, and S17, described above. Similarly, results for scenarios S16 and S18 can also be compared. Inspection of these results indicates that the hydrodynamic impacts due to tidal power lagoons in Chignecto Bay are quite different than the impacts due to similar lagoons located in Minas Basin. Despite these significant differences, the modelling results show that the presence of operating tidal power lagoons in either Minas Basin or Chignecto Bay will tend to increase the range of the tides along the shoreline of the Gulf of Maine, including at Boston.

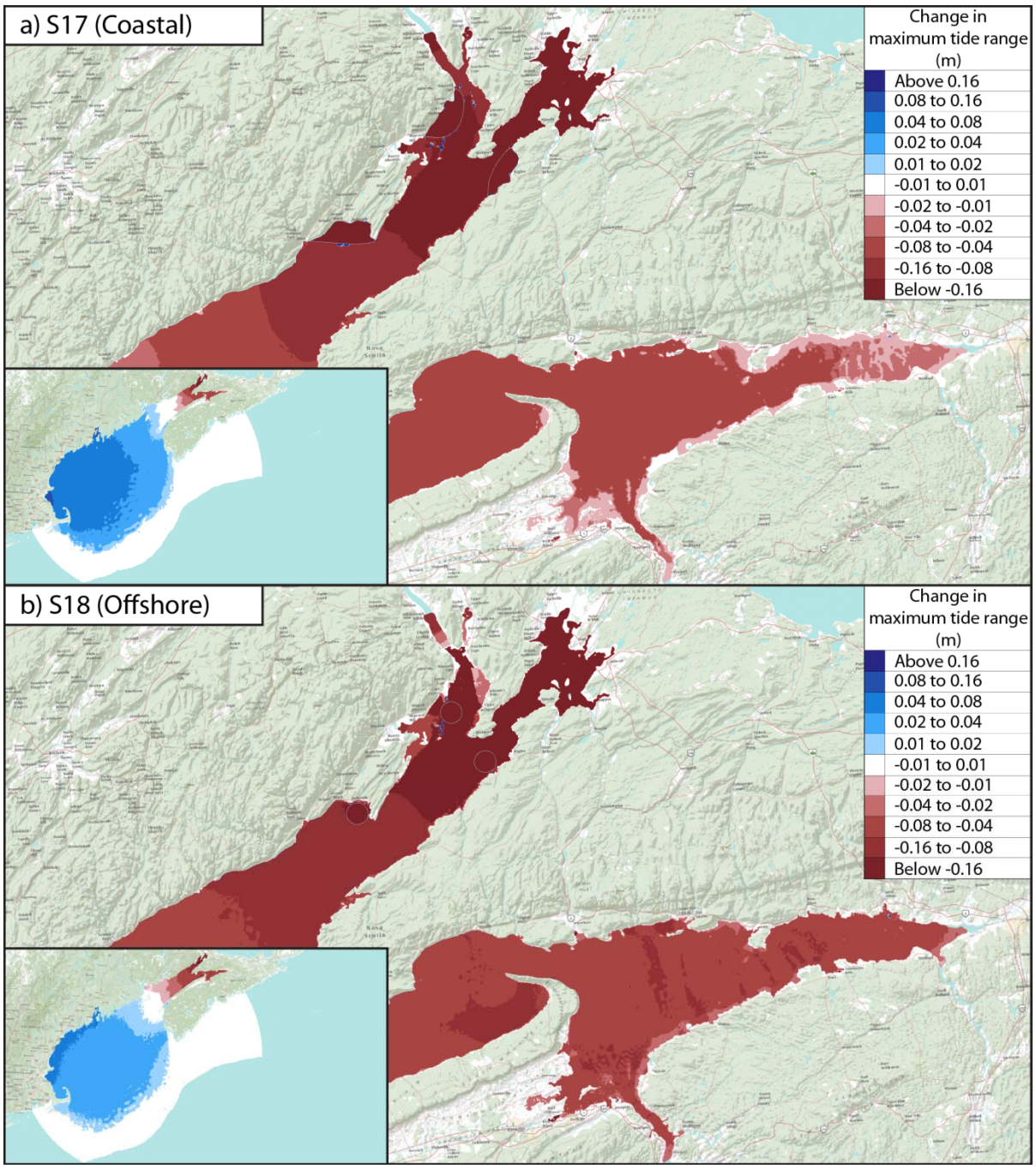

Figure 64. Change in maximum tide range for scenarios S17 and S18.

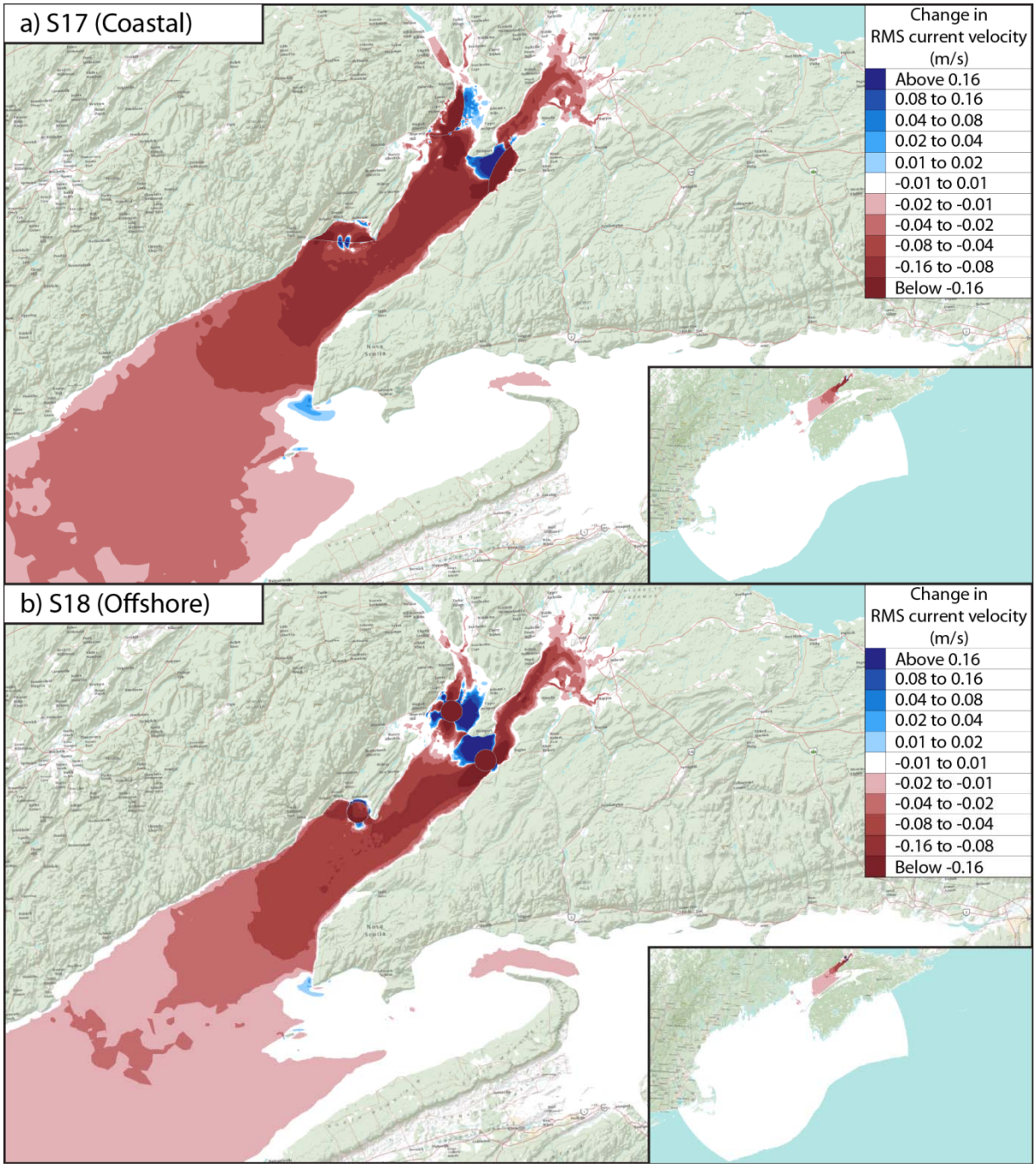

Figure 65. Far-field change in U_{RMS} for scenarios S17 and S18.

5.8 Six Lagoons in Minas Basin and Chignecto Bay, Scenario S19

Six offshore lagoons were modelled in scenario S19; three located in Minas Basin at sites A-C, and three located in Chignecto Bay at sites D-F. The surface area of each impoundment was 12 km^2, and the combined area was therefore 72 km^2. Note that the three offshore lagoons in Minas Basin were considered in scenario S16, while the three offshore lagoons in Chignecto Bay were modelled in scenario S18.

The predicted change in maximum tide range for scenario S19 is mapped in Figure 66, while the predicted change in RMS current velocity is mapped in Figure 67. It can be seen that the pattern of tidal range change for scenario S19 is essentially a mixture of the results for scenarios S16 and S18, shown in Figure 62 and Figure 64. Moderate reductions in maximum tide range are predicted for the upper Bay of Fundy, including both Minas Basin and Chignecto Bay, while moderate increases in tide range are predicted across the Gulf of Maine. The maximum tide range along the shore of the Gulf of Maine is predicted to increase by from 6 to 8 cm for scenario S19, while reductions in maximum tide range greater than 16 cm are predicted for some parts of eastern Minas Basin and northern Chignecto Bay.

The predicted changes in far-field tidal current speed for scenario S19 are a mixture of the results for scenarios S16 and S18 shown above in Figure 63 and Figure 65. These results indicate that the currents at the center of Minas Passage for scenario S19 will be roughly 10 cm/s slower than for existing conditions without lagoons. Virtually no changes in tidal current speed are predicted across the entire Gulf of Maine for scenario S19. The largest changes in tidal currents will occur near the lagoons, particularly inside the lagoons and outside the lagoons near the powerhouses and along the perimeter of the impoundment dykes.

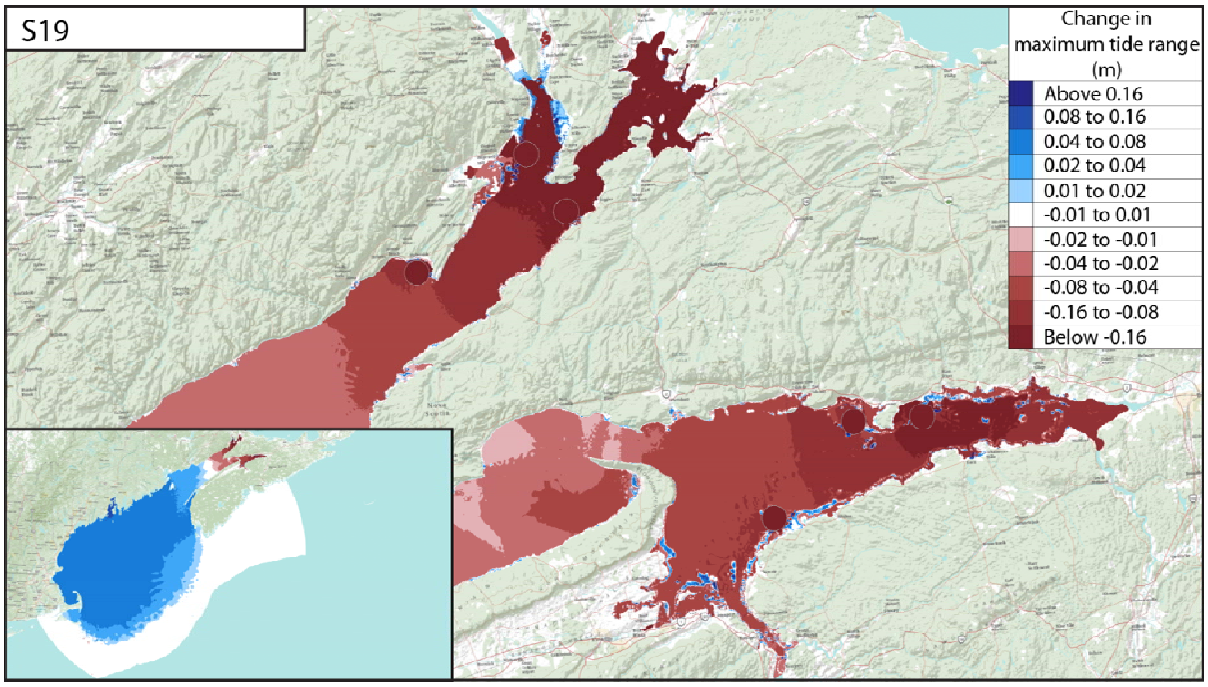

Figure 66. Change in maximum tide range for scenario S19.

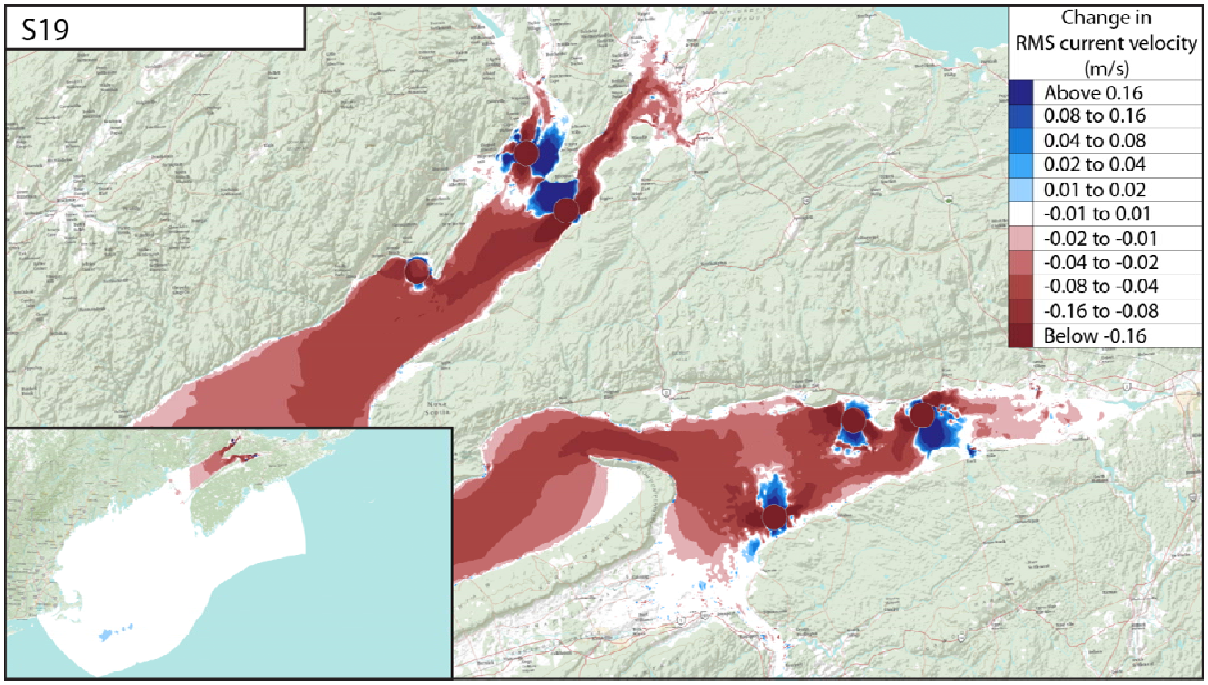

Figure 67. Far-field change in U_{RMS} for scenario S19.

5.9 Summary of Hydrodynamic Impacts at Reference Sites

The hydrodynamic changes (relative to existing conditions) at several locations in the Bay of Fundy and Gulf of Maine, derived from the numerical simulations of scenarios S1-S19, are summarised below in Table 7. The change in maximum tide range is shown for five tide stations distributed across the study domain, namely: Boston, Bar Harbor, Saint John, Chignecto and Five Islands. Similarly, the change in RMS tidal current speed is shown for five reference sites, namely: Minas Basin, Minas Passage, Minas Basin Entrance (MB Entrance), Chignecto Bay Entrance (CB Entrance) and Chignecto. These reference stations and reference sites are mapped in Figure 68.

In Table 7 the change in maximum tide range is expressed as a percentage of the maximum tide range at that station for existing conditions without tidal power lagoons. These values were obtained from simulation S0, and are also shown in Table 7. The predicted changes in RMS tidal current speed for each reference site are also expressed as a percentage of U_{RMS} for existing conditions, as predicted in simulation S0.

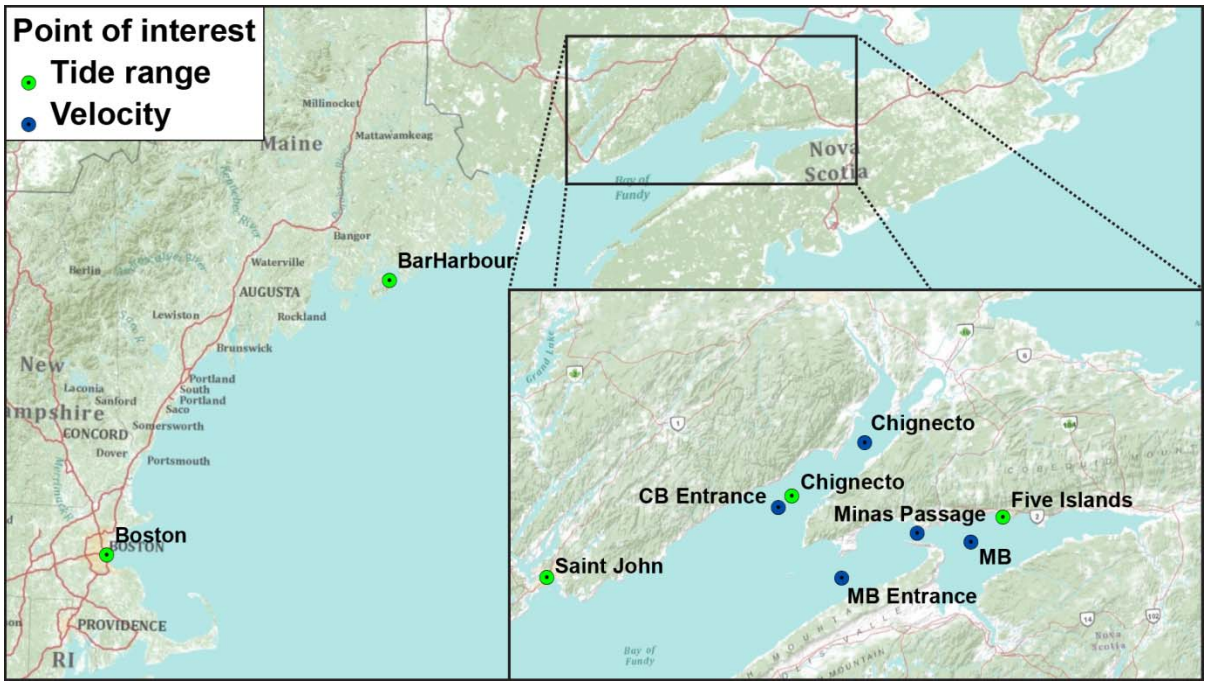

Figure 68. Map of reference stations and reference sites.

		Boston (8443970)	Bar Harbor (8413320)	Saint John (65)	Chignecto (40139)	Five Islands (260)	Minas Basin	Minas Passage	MB Entrance	CB Entrance	Chignecto	
Long. (°)		-71.052	-68.205	-66.067	-64.983	-64.067	-64.211	-64.443	-64.784	-65.043	-64.652	
Lat. (°)		42.355	44.392	45.267	45.483	45.383	45.314	45.349	45.224	45.450	45.636	
Scenario		**Maximum tide range (m)**					**RMS current velocity, U_{RMS} (m/s)**					**RMS power output, P_{RMS} (MW)**
S0		3.60	3.89	7.32	10.14	12.76	0.22	2.01	0.37	0.58	0.70	0
S1	Δ	0.4%	0.5%	0.5%	0.4%	0.0%	-13.4%	-2.2%	-5.1%	0.2%	0.4%	265
S2	Δ	0.3%	0.3%	0.2%	0.2%	-0.1%	-7.9%	-1.4%	-3.2%	0.2%	0.1%	156
S3	Δ	0.4%	0.5%	0.5%	0.4%	0.1%	-14.4%	-2.4%	-5.6%	0.2%	0.4%	264
S4	Δ	0.5%	0.4%	0.5%	0.4%	0.0%	-12.0%	-1.9%	-4.3%	0.3%	0.4%	246
S5	Δ	0.4%	0.4%	0.5%	0.4%	0.0%	-11.6%	-1.9%	-4.3%	0.3%	0.4%	172
S6	Δ	0.3%	0.3%	0.2%	0.1%	-0.7%	-7.4%	-1.4%	-3.7%	0.0%	0.1%	0
S7	Δ	0.4%	0.5%	0.5%	0.5%	0.4%	-11.6%	-1.8%	-3.5%	0.5%	0.6%	0
S8	Δ	0.7%	0.8%	0.7%	0.6%	0.2%	-20.8%	-3.5%	-8.0%	0.3%	0.6%	373
S9	Δ	1.2%	1.6%	1.2%	1.0%	-	-38.0%	-6.4%	-14.4%	0.7%	1.0%	658
S10	Δ	0.3%	0.3%	0.2%	0.2%	-0.1%	-8.3%	-1.4%	-3.5%	0.0%	0.1%	142
S11	Δ	0.4%	0.5%	0.4%	0.3%	-0.1%	-13.9%	-2.4%	-5.6%	0.2%	0.3%	239
S12	Δ	0.6%	0.7%	0.6%	0.5%	-0.1%	-19.4%	-3.3%	-7.5%	0.3%	0.4%	296
S13	Δ	0.5%	0.6%	0.8%	0.7%	0.9%	-16.2%	-2.4%	-4.8%	0.7%	0.7%	360
S14	Δ	0.6%	0.8%	0.5%	0.4%	0.0%	-12.5%	-3.9%	-9.4%	0.2%	0.4%	385
S15	Δ	1.7%	2.2%	1.7%	1.4%	0.8%	-45.8%	-9.0%	-20.3%	0.9%	1.4%	988
S16	Δ	0.7%	1.0%	0.7%	0.5%	0.0%	-20.8%	-4.6%	-11.0%	0.2%	0.4%	411
S17	Δ	2.4%	0.8%	0.0%	-0.9%	-0.4%	-2.3%	-0.5%	-2.1%	-12.0%	-18.5%	747
S18	Δ	1.3%	0.4%	-0.2%	-0.9%	-0.6%	-2.8%	-0.6%	-2.7%	-8.2%	-14.1%	312
S19	Δ	2.0%	1.5%	0.5%	-0.4%	-0.8%	-23.1%	-5.2%	-13.6%	-8.0%	-13.6%	723

Table 7. Summary of hydrodynamic changes at reference sites for scenarios S1-S19.

5.10 Relationships Between Power Output and Hydrodynamic Impact

As expected, our simulations suggest that the scale of the changes in tidal hydrodynamics increase with increases in the scale of lagoon development. While multiple lagoons or larger lagoons located in the upper BoF will generate more electrical power, they also constitute a larger perturbation to a near resonant system, and can therefore be expected to induce larger changes in tidal hydrodynamics. The results of this study delineate the trade-off between power generation from tidal lagoons and hydrodynamic impact. In this section, various relationships are developed linking the power generation by tidal power lagoons to the associated hydrodynamic impact.

The power output for the tidal power lagoons considered in this study is found to be directly proportional to the impoundment area, A. Results for the bi-directional generation mode are plotted in Figure 69. In this figure, the triangular and circular symbols denote results from hypothetical scenarios with coastal and offshore tidal lagoons, respectively. For offshore lagoons in Minas Basin, $P_{RMS} = 11.1A$ provides a good description of the relationship between power output and impoundment area, while for coastal lagoons in Minas Basin, $P_{RMS} = 10.6A$. For a fixed lagoon size, the power output in Chignecto Bay will be slightly less than in Minas Basin due to the lower tide range.

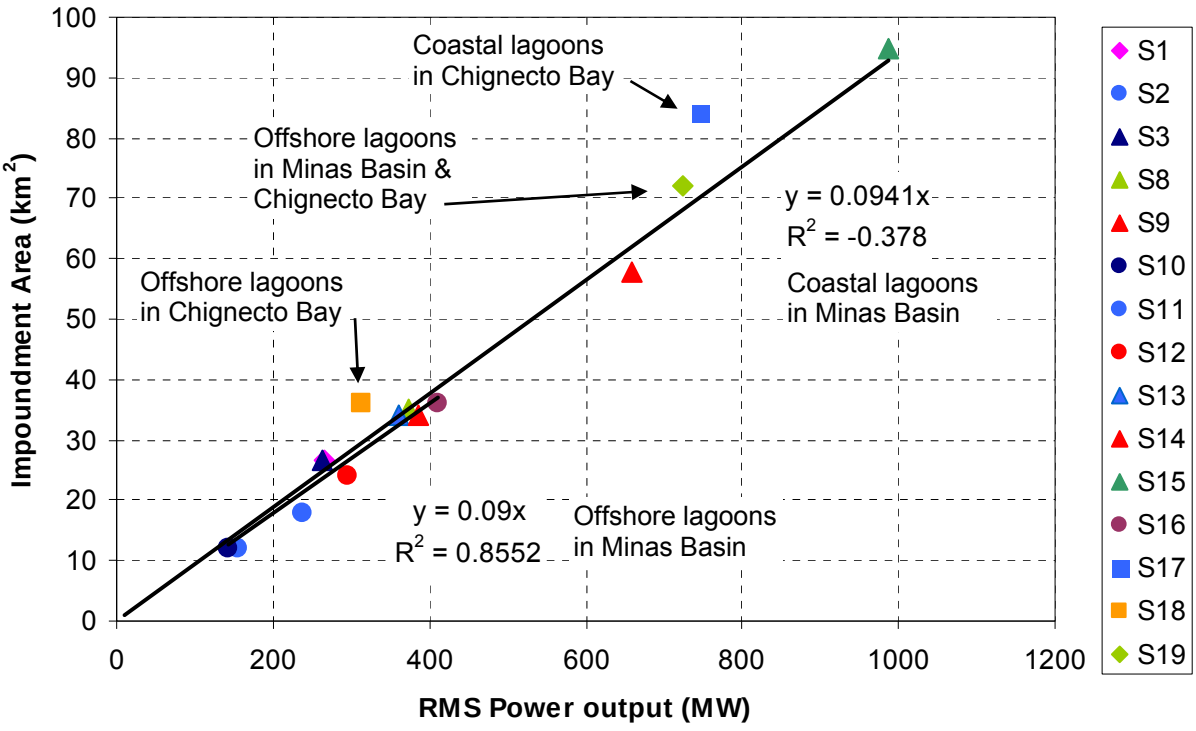

Figure 69. Relationship between lagoon area and power output.

The predicted impacts of the various hypothetical scenarios considered in this study on the maximum tide range at Boston are plotted in Figure 70 versus RMS power output. Blue diamonds are used to denote results for scenarios with tidal lagoons in Minas Basin (scenarios S1-S3 and S8-S16), violet squares denote results for scenarios S17 and S18, with tidal lagoons in Chignecto Bay, and a red diamond denotes the result for scenario S19, where lagoons in Minas Basin and Chignecto Bay were modelled together. For tidal power lagoons in Minas Basin, these results reveal a strong linear relationship between the power output and the change in amplitude of the Boston tides. Although lagoons in Chignecto Bay were only considered in two scenarios, these results also suggest a linear relationship between power output and the change in the amplitude of the tides at Boston. Greater power generation is clearly linked to stronger hydrodynamic impact. Moreover, for equal power output, the impact on the Boston tides due to tidal power lagoons in Chignecto Bay will be roughly double the impact due to lagoons in Minas Basin. In other words, the tides at Boston are roughly twice as sensitive to power generation in Chignecto Bay compared to equivalent power generation in Minas Basin.

The predicted change in the maximum tide range at Bar Harbor due to the various hypothetical scenarios considered in this study is plotted in Figure 71 as a function of RMS power output. As at Boston, separate linear relationships are found between power output and the change in tide range at Bar Harbor for lagoons in Minas Basin and in Chignecto Bay. However, unlike at Boston, these results indicate that the tides at Bar Harbor are more sensitive to power generation in Minas Basin than in Chignecto Bay. For equal power output, the impact on the Bar Harbor tides due to tidal power lagoons in Chignecto Bay will be roughly half as large as the impact due to lagoons in Minas Basin.

The predicted change in the maximum tide range at Saint John is plotted versus RMS power output in Figure 72. Again, the results indicate a strong linear relationship between power generation in Minas Basin and the impact on the tide range at Saint John. Greater power generation is again clearly linked to stronger hydrodynamic impact. However, results for scenarios with lagoons in Chignecto Bay do not follow this rule. In fact, although only two data points are available, they suggest that producing power in Chignecto Bay has virtually no impact on the tide range at Saint John.

Finally, Figure 73 shows the predicted change in the maximum tide range at the Chignecto reference station for each of the various hypothetical scenarios considered in this study, plotted as a function of the RMS power output. In this case, the results confirm a strong linear relationship between the power output from lagoons in Minas Basin and the tide range at Chignecto. The tide range at Chignecto will increase in response to increases in the power output from lagoons in Minas Basin. However, for the case of lagoons in Chignecto Bay, the results suggest that the tide range at Chignecto will decrease in response to increases in the power output from lagoons in Chignecto Bay. Generating power in Minas Basin increases the tides at the Chignecto station, while generating power in Chignecto Bay reduces them. Based on these observations it seems reasonable to conclude that changes in the tide range at Chignecto might be minimized by generating power in both Minas Basin and Chignecto Bay at the same time. The results for scenario S19, plotted in Figure 73, support this conclusion. This interesting result is particular to the Chignecto reference station, and does not apply elsewhere.

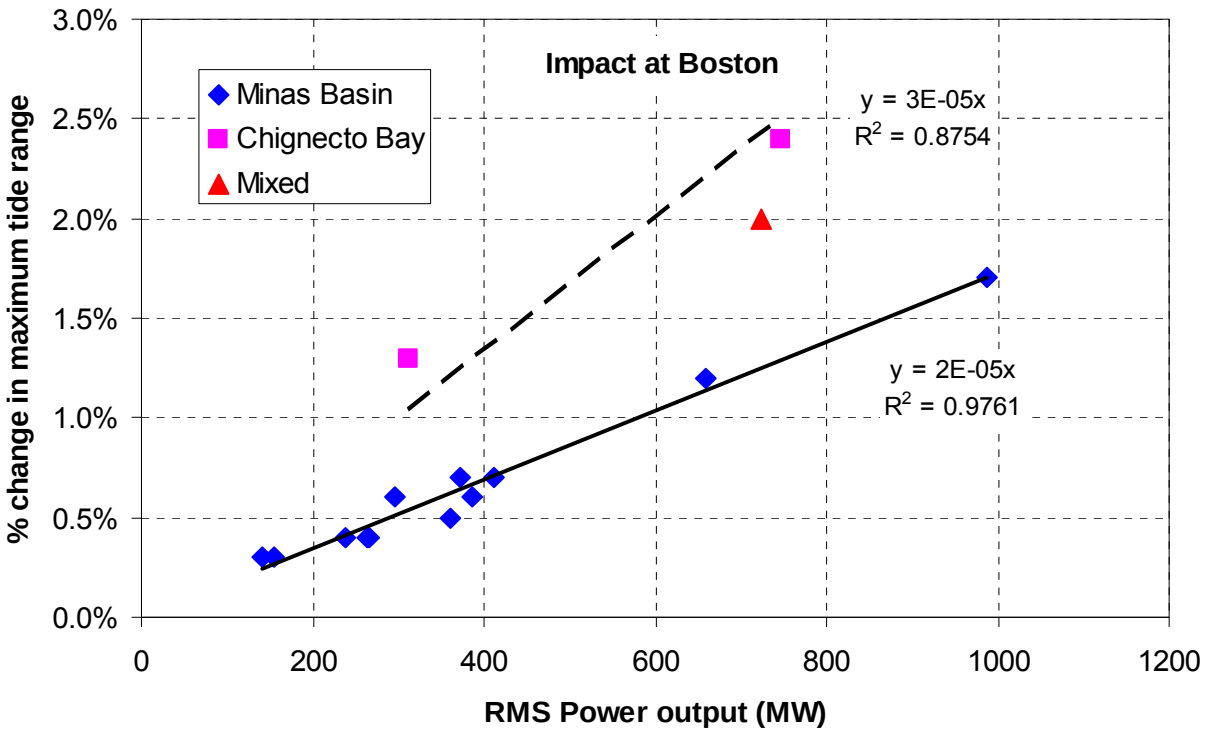

Figure 70. Influence of power generation by tidal lagoons on the maximum tide range at Boston.

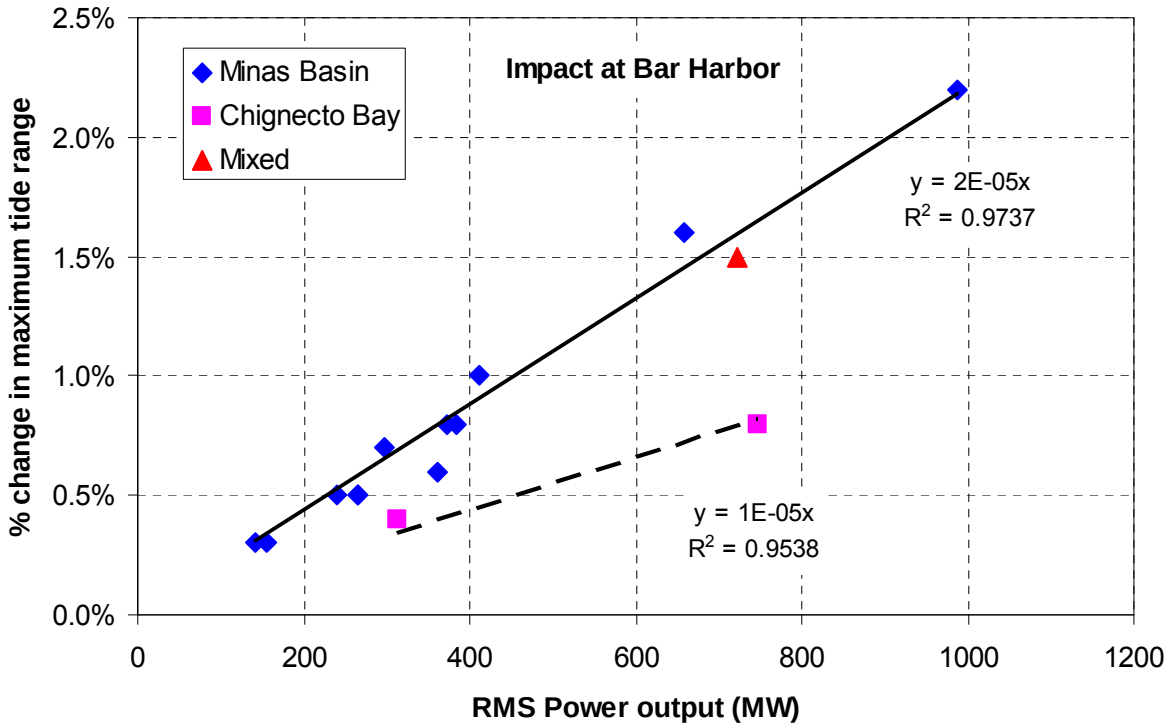

Figure 71. Influence of power generation by tidal lagoons on the maximum tide range at Bar Harbor.

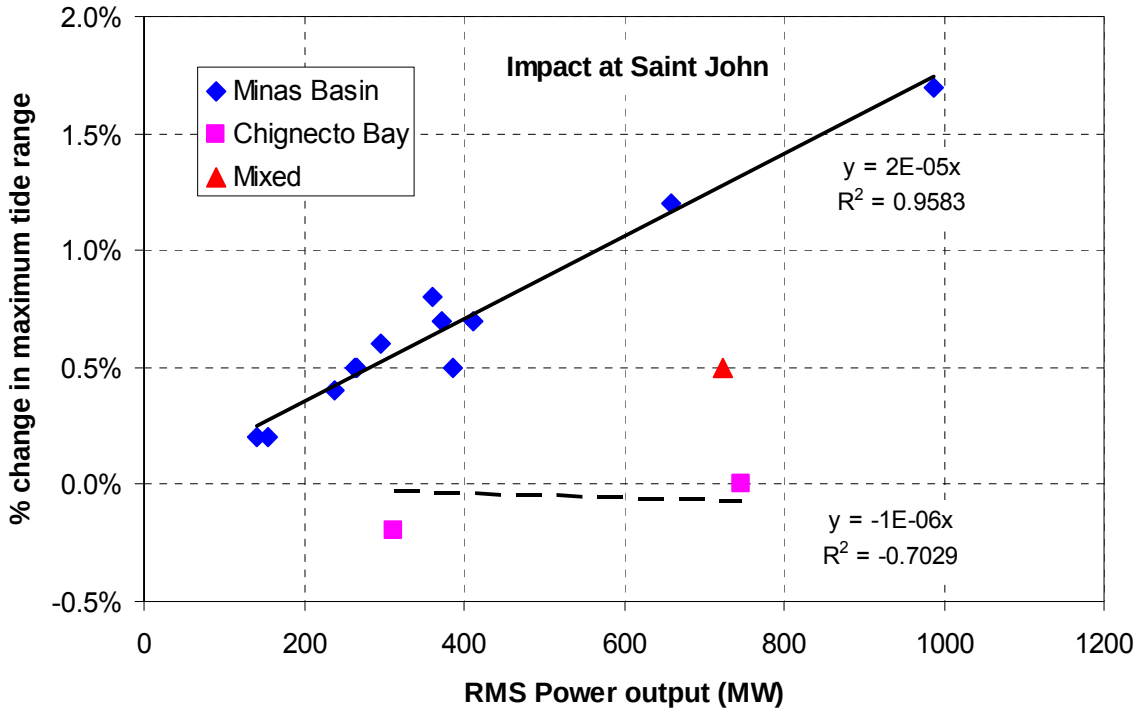

Figure 72. Influence of power generation by tidal lagoons on the maximum tide range at Saint John.

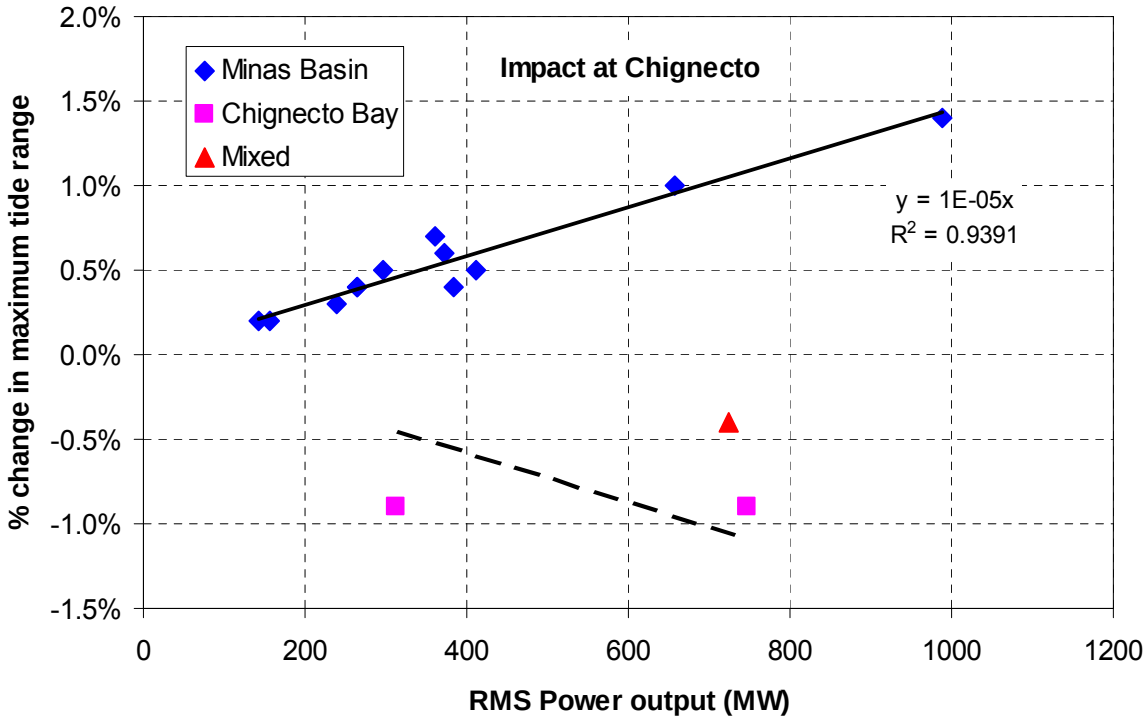

Figure 73. Influence of power generation by tidal lagoons on the maximum tide range at Chignecto.

The variation in hydrodynamic impact (change in maximum tide range) with distance for scenarios S3 and S8-S14 is plotted in Figure 74. All of these scenarios feature a single tidal power lagoon operating in Minas Basin. Coastal lagoons at site A were modelled in scenarios S3, S8 and S9, offshore lagoons at site A were modelled in scenarios S10-S12, and coastal lagoons at sites B and C were modelled in scenarios S13 and S14, respectively. In all cases, the magnitude of the hydrodynamic impact attenuates with increasing distance. The pattern of the attenuation is similar for all lagoons at sites A and C. However, the pattern for site B is different; the near-field change in tide range for scenario S13 (coastal lagoon at site B) is significantly larger than for the other cases. Figure 74a and Figure 74b also highlight the strong dependence of far-field hydrodynamic impact on lagoon size. The magnitude of the change in tide range increases linearly with increasing lagoon size.

The graph shown in Figure 75 was prepared to illustrate the influence of operating mode on the changes in maximum tide range induced by a 26.7 km^2 coastal lagoon in Minas Basin at site A. The changes in maximum water level at the five reference stations mapped in Figure 68 are plotted in Figure 75 as a function of the distance from site A. Different symbols are used to denote the results from scenarios S3-S7. The impact at Five Islands, located only 15 km from site A, is relatively sensitive to the operating mode, whereas the impact at more distant sites, such as Bar Harbor and Boston, are fairly insensitive to changes in operating mode. These results show that the far-field change in tide range is minimized for scenario S6, where the sluice gates are always open, and maximized for scenario S7, where the sluices are always closed. The hydrodynamic impact at each reference station is similar for the three different power generating operating modes modelled in scenarios S3, S4 and S5 (2-way generation, ebb-generation and flood-generation, respectively).

The changes in maximum depth-averaged current speed at the five reference sites mapped in Figure 68 are plotted in Figure 76 as a function of the distance from site A. Different symbols are used to denote the results from scenarios S3-S7. At each site, the impact is smallest for scenario S6, where the sluice gates are always open, and greatest for scenario S3, where a 2-way generation scheme was modelled. The predicted changes in tidal flows at distant locations are very small and quite insensitive to changes in operating mode. Closer to the lagoon, the changes are larger and more sensitive to the operating mode.

The predicted change in RMS current speed at Minas Passage for each of the various hypothetical scenarios considered in this study is plotted in Figure 77 as a function of RMS power output. These results reveal the presence of a strong linear relationship between power generation from tidal lagoons in Minas Basin and reductions in current speed at Minas Passage. They also show that the flows at Minas Passage are insensitive to power generation from tidal lagoons in Chignecto Bay.

Figure 78 is a similar figure in which only results for lagoons at site A are shown. This figure shows that the linear relationship between power output and hydrodynamic impact is virtually identical for both offshore lagoons and coastal lagoons.

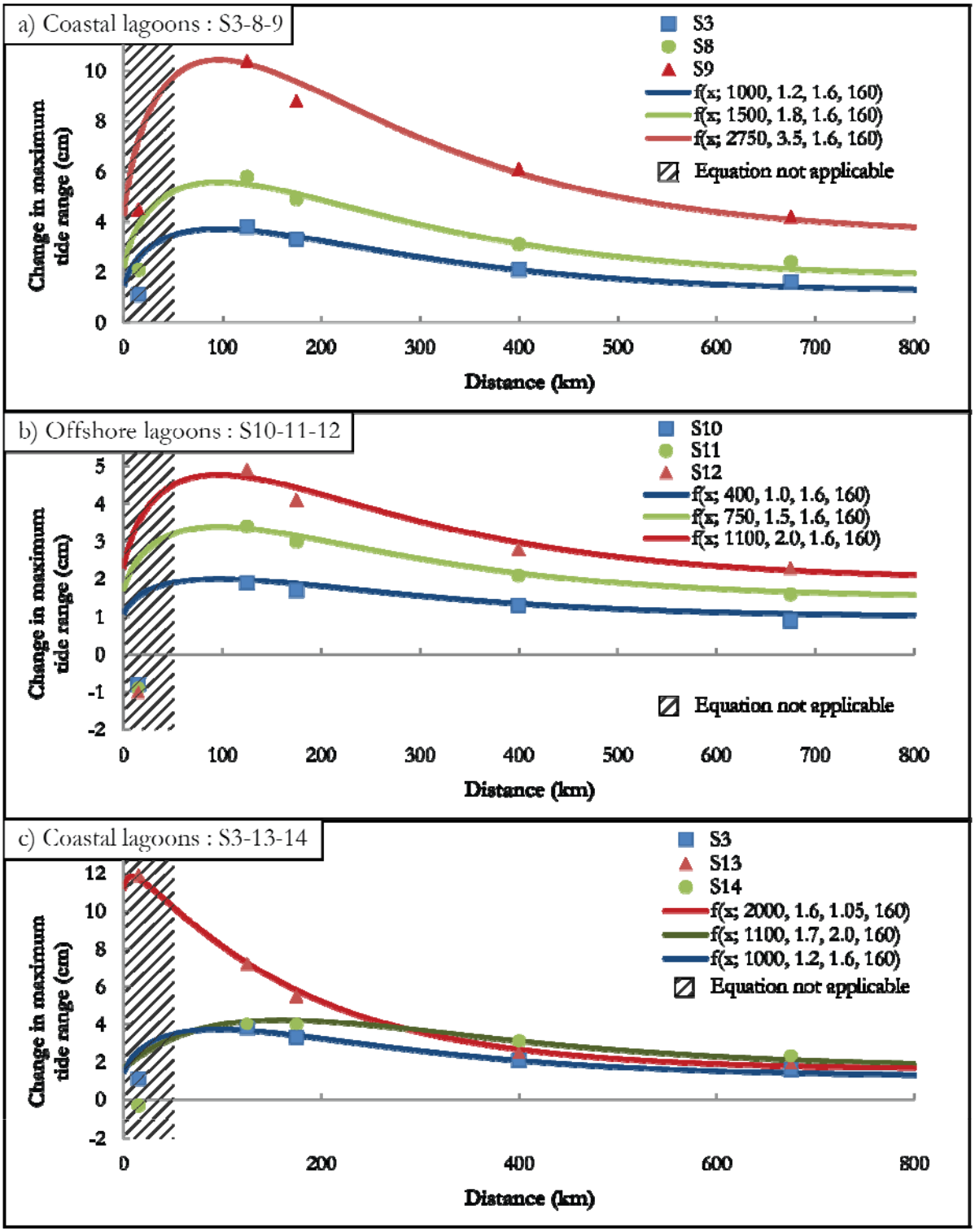

Figure 74. Far field change in maximum tide range due to tidal power lagoons in Minas Basin.

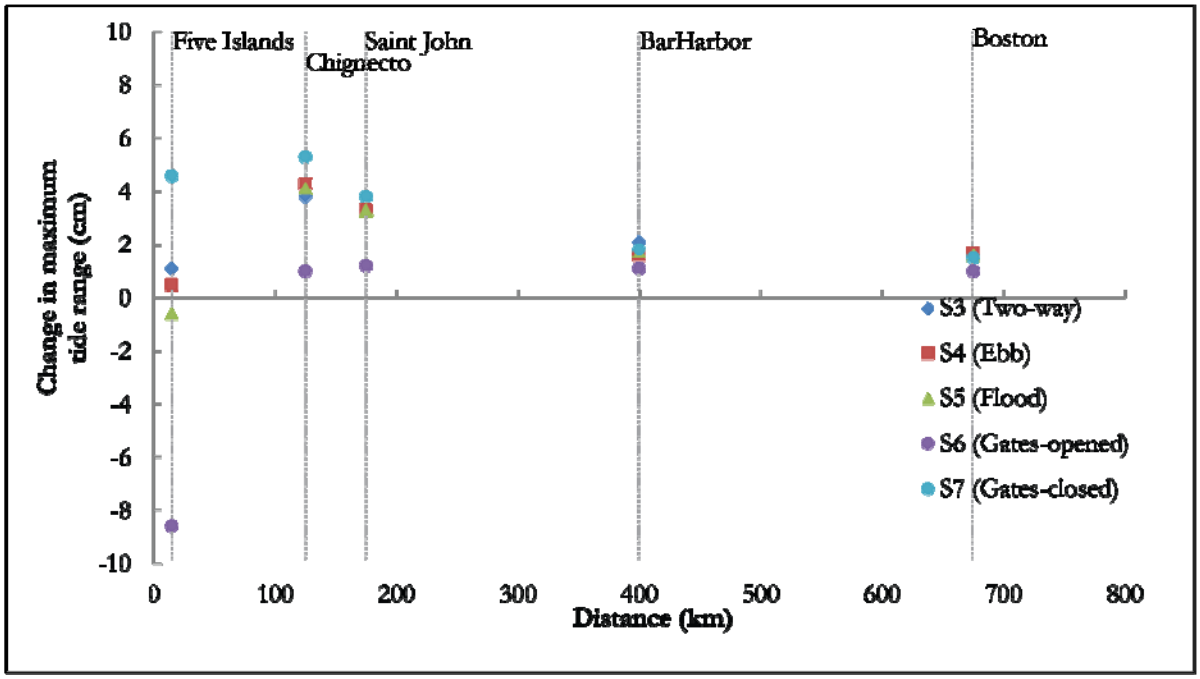

Figure 75. Change in maximum tide range versus distance for scenarios S3-S7.

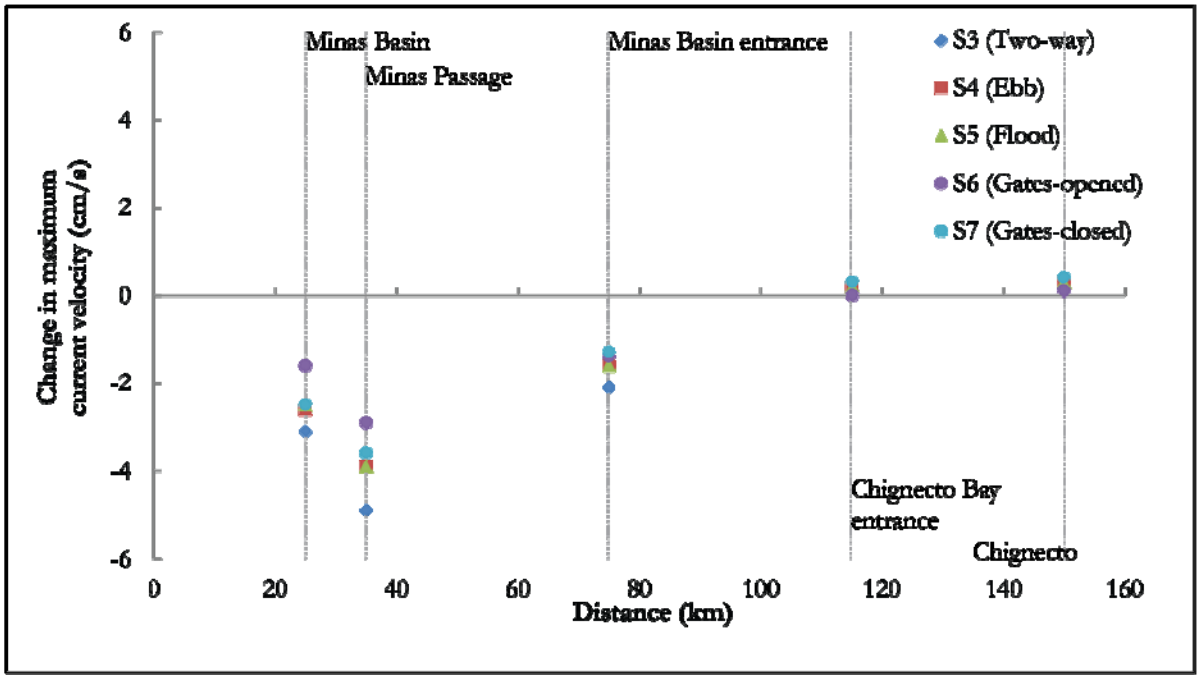

Figure 76. Change in maximum depth-averaged current speed versus distance for scenarios S3-S7.

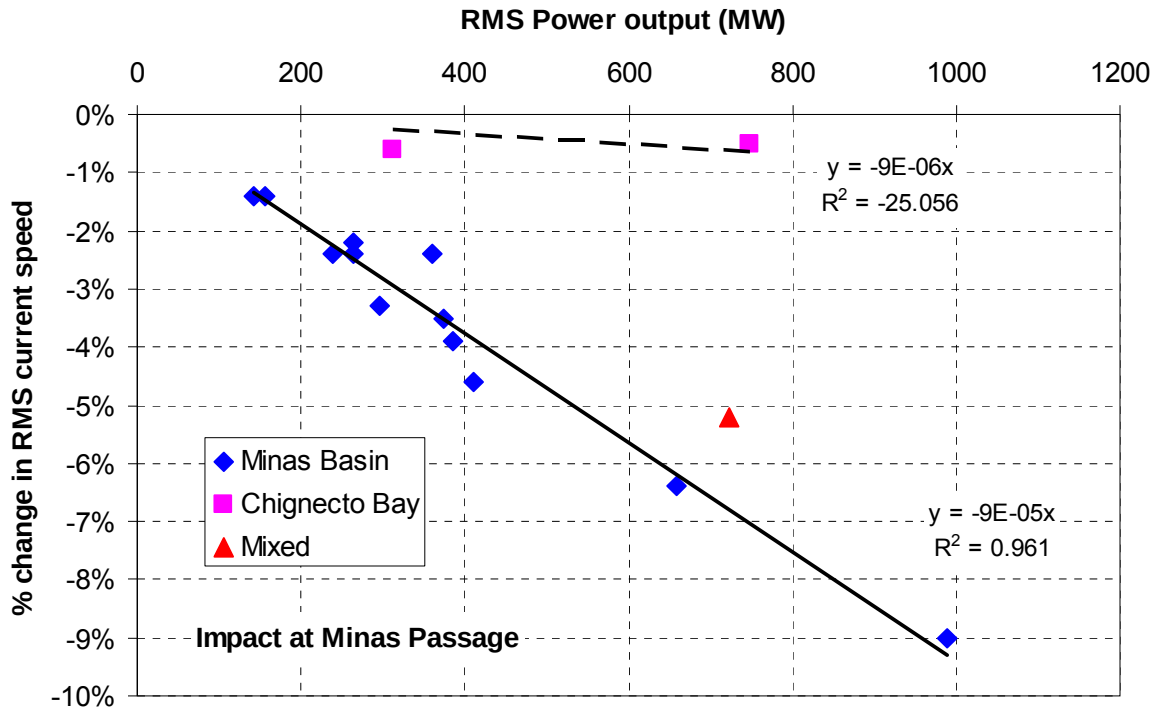

Figure 77. Influence of power generation by tidal lagoons on current speed at Minas Passage.

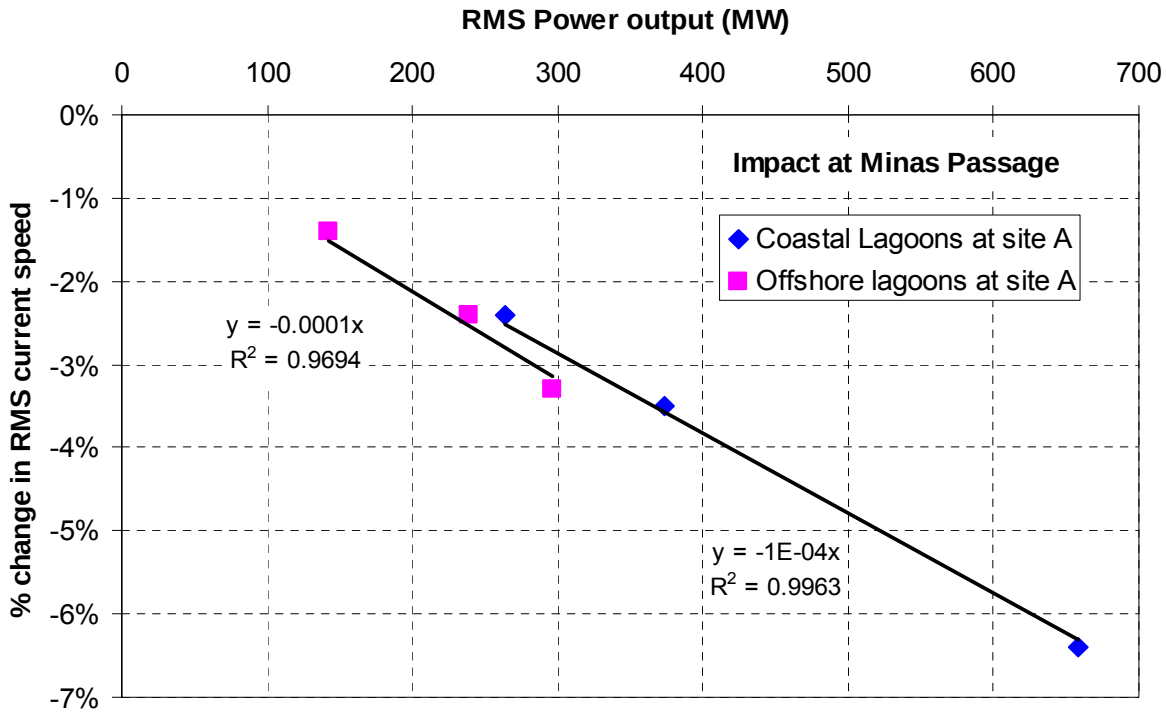

Figure 78. Influence of power generation by lagoons at site A on current speed at Minas Passage.

6 Conclusions

This study has examined the changes in the tidal hydrodynamics in the Gulf of Maine and the Bay of Fundy resulting from the operation of man-made lagoons for converting tidal fluctuations into electrical power, located in the upper part of the Bay, in Minas Basin and Chignecto Bay. Tidal power lagoons are a newer approach to tidal power conversion that attempts to achieve high efficiency while avoiding some of the environmental problems associated with tidal barrages. A typical tidal power lagoon consists of a large impoundment structure (a rubble-mound dyke or caisson) and a power-house containing sluices and conventional low-head hydroelectric generating equipment, situated a mile or more offshore in an area with shallow depths and high tides

A detailed two-dimensional (depth-averaged) hydrodynamic model, based on the TELEMAC modelling system, has been developed and applied to investigate the changes in water levels and tidal currents for a range of hypothetical lagoon development scenarios. The model was successfully calibrated and validated against water level observations for many tide stations throughout the region, and can be used to predict tidal hydrodynamics with good accuracy. Lagoons are simulated by partitioning the model domain into sub-domains, and using source-sink pairs to simulate the exchange of seawater through sluices and turbines. The flows through sluices are estimated using an orifice equation, while the flows through turbines and the resulting power output are based on published performance curves for double-regulated bulb turbines. This modelling approach is able to provide a reasonable simulation of the hydrodynamic processes at man-made tidal power lagoons. All of the hypothetical lagoons considered in this study included a single storage basin.

The model was subsequently applied to predict tidal hydrodynamics for present conditions without lagoons, and for nineteen different hypothetical scenarios featuring from one to six individual lagoons. Lagoons were simulated at three sites in Minas Basin and at three sites in Chignecto Bay. The scenarios included variations in lagoon size, lagoon type (coastal or offshore), lagoon location, the number of lagoons, and the operating mode (2-way generation, ebb-generation or flood-generation). Hydrodynamic impacts have been estimated by differencing results for each hypothetical scenario from equivalent results for existing conditions without lagoons. The sensitivities to changes in lagoon location, lagoon size, lagoon type, operating mode and the number of lagoons have been investigated by comparing results for various scenarios.

As expected, the numerical results indicate that any tidal power lagoon will induce some large changes in the pattern and strength of the local tidal currents, particularly near the powerhouse and possibly along portions of the impoundment dyke. Numerical results indicate that the changes in water levels and tidal current velocities are largest near the lagoons and generally diminish with increasing distance. Notably, however, a small change in tide range is predicted throughout the entire Gulf of Maine, even for the smallest development scenario.

While larger tidal power lagoons and more numerous lagoons will produce more energy, they also constitute a larger perturbation to a near resonant system, and can therefore be expected to cause bigger changes in the tidal hydrodynamics. As expected, our results suggest that the magnitude of the changes in tidal hydrodynamics increase with increases in the scale of lagoon development; with larger lagoons and multiple lagoons inducing greater hydrodynamic change. For example the numerical results indicate that a single 26.7 km^2 coastal lagoon operating in

Minas Basin with an RMS power output of 264 MW will cause the tide range in Boston to increase by ~1.4 cm; a single 57.7 km^2 coastal lagoon operating in Minas Basin with an RMS power output of 658 MW will cause the tide range in Boston to increase by ~4.3 cm; and three coastal lagoons operating in Minas Basin with a combined area of 94.8 km^2 and a combined RMS power output of 988 MW will induce a ~7.2 cm increase in the Boston tides. While these changes represent a small fraction of the tide range, their potential impact on communities and ecosystems warrants careful consideration and further investigation. Hence, without further study, it is difficult to comment on whether the potential benefits of tidal power lagoons might outweigh the drawbacks associated with these changes in tidal hydrodynamics.

The trade-off between power generation from tidal lagoons and hydrodynamic impact is delineated by way of a set of linear relationships linking power output and hydrodynamic change. Strong linear relationships are found between the scale of lagoon development (characterized by the combined RMS power output) and the change in maximum tide range for several communities around the Bay of Fundy and Gulf of Maine, including, Boston, Bar Harbor and Saint John. Interestingly, the tide range at Boston is found to be more sensitive to lagoon development in Chignecto Bay than in Minas Basin, whereas the tide range at Bar Harbor, is more sensitive to lagoon development in Minas Basin. Furthermore, at Saint John the tide range is found to be sensitive to lagoon development in Minas Basin, but is found to be insensitive to lagoon development in Chignecto Bay. Expressed in another way; lagoon development in Chignecto Bay will increase the tide range at Boston and Bar Harbor, but not at Saint John; whereas lagoon development in Minas Basin will increase the tide range at all three cities.

A strong linear relationship is also found linking the scale of the lagoon development in Minas Basin to the attenuation in the speed of the depth-averaged currents at Minas Passage. For example, the numerical results indicate that a single 26.7 km^2 coastal lagoon operating in Minas Basin with an RMS power output of 264 MW will cause a ~2.4% reduction in the RMS current speed at Minas Passage; a single 57.7 km^2 coastal lagoon operating in Minas Basin with an RMS power output of 658 MW will cause a ~6.4% reduction in the RMS current speed at Minas Passage; and three coastal lagoons operating in Minas Basin with a combined area of 94.8 km^2 and a combined RMS power output of 988 MW will induce a ~9% reduction in the currents at Minas Passage. The speed of the current at Minas Passage is found to be insensitive to lagoon development in Chignecto Bay.

For the lagoons considered in this study, the power output for a given operating mode was found to be proportional to the surface area of the impoundment. However, because the tide range in Minas Basin is slightly larger than in Chignecto Bay, a lagoon with unit area can generate slightly more energy when located in Minas Basin.

Three different operating modes have been modelled and assessed in this study, namely: flood-generation, ebb-generation and 2-way generation. The flood-generation mode is found to yield less energy than either the ebb-generation or 2-way generation modes, which produce similar amounts of energy. These operating modes are found to have considerable influence on local velocities near the lagoon, particularly near the powerhouse. However, the operating mode appears to have little influence on the magnitude of far-field hydrodynamic impacts.

In this study we have developed methods for simulating the presence and operation of man-made tidal power lagoons within a 2D hydrodynamic model, and applied these methods to discover and assess the magnitude and character of the changes in tidal hydrodynamics throughout the

Bay of Fundy and Gulf of Maine that would be caused by tidal power lagoons operating in Minas Basin and in Chignecto Bay. The study has generated lots of good new information concerning the relationships between power generation and hydrodynamic change, and the influences on these relationships of variations in lagoon size, lagoon location, lagoon type, operating mode and the number of lagoons. These results will help inform current and future policies concerning the development of the vast tidal energy resources in the Bay of Fundy.

A future direction for this research is to investigate the implications of the velocity changes on sediment transport and on the response of the seabed near and within a lagoon. Another future direction is to simulate the impact of lagoons with multiple storage basins. The new numerical model can also be applied to simulate and assess the hydrodynamic impacts of other tidal energy developments, including tidal barrages and arrays of in-stream turbines.

7 Acknowledgment

The authors gratefully acknowledge funding received from the Nova Scotia Association for Offshore Energy Environmental and Technical Research. They also acknowledge with gratitude the many contributions to this research made by Dr. Ioan Nistor, Associate Professor with the University of Ottawa.

8 References & Bibliography

[1] AEA Energy and Environment, 2007. Severn Estuary Tidal Energy from Non-barrage Options. Report to the UK Sustainable Development Commission.

[2] Baker, A. C., 1991. *Tidal Power.*, Peter Peregrinus Ltd., London, United Kingdom.

[3] Bay of Fundy Tidal Power Review Board. 1974. Preliminary Reassessment of Feasibility of Tidal Power Development in the Bay of Fundy.

[4] Bay of Fundy Tidal Power Review Board. 1977. Reassessment of Fundy Tidal Power. Ottawa, Report prepared for the Minister of Supply and Services (Canada), under contract No. 02KX 23384-5207.

[5] Chow, V. T. 1959. *Open-Channel Hydraulics*., McGraw-Hill, Inc.

[6] Cousineau, J., Cornett, A., Nistor, I., 2011. Assessment of hydrodynamic impacts throughout the Bay of Fundy and Gulf of Maine due to tidal energy extraction by tidal lagoons. *Proc. 20th Canadian Hydrotechnical Conf.*, CSCE, Ottawa

[7] Cousineau, J., 2011. Hydrodynamic Impacts of Tidal Lagoons in the Upper Bay of Fundy. M.A.Sc. Thesis, Dept. of Civil Engineering, University of Ottawa.

[8] Cornett, A., 2006. Inventory of Canada's Renewable Marine Energy Resources. Canadian Hydraulics Centre, National Research Council, Report CHC-TR-041.

[9] Cornett, A., Cousineau, J.; Nistor, I., 2011. Hydrodynamic Impacts due to Tidal Power Lagoons in the Upper Bay of Fundy, Canada. *Proc. 2011 European Wave and Tidal Energy Conf.*, Southampton

[10] Cornett, A., Durand, N., Serrer, M., 2010. 3-D Modelling and assessment of tidal current resources in the Bay of Fundy, Canada. *Proc. 3rd Int. Conf. on Ocean Energy*, Bilbao.

[11] Delta Marine Consultants (DMC), 2007. Tidal Power Plant: Bay of Fundy, Technical Feasibility Study. 2007.

[12] Dupont, F., Hannah, C.G., and Greenberg, D.A., 2005. Modelling the Sea Level of the Upper Bay of Fundy. *Atmosphere-Ocean*, 2005, 43(1), 33–47.

[13] Durand, N., Cornett, A., and Bourban, S. 2008. 3-D modelling and assessment of tidal current energy resources in the Bay of Fundy. Canadian Hydraulic Centre, NRC, Ottawa, Report CHC-TR-052.

[14] Falconer, R., Xia, J., Lin, B., Ahmadian, R., 2009. The Severn barrage and other tidal energy options: Hydrodynamic and power output modelling. *Sci China Ser E-Tech Sci*, 2009, 52(11) 3413-3424.

[15] Electric Power Research Institute (EPRI), 2006. New Brunswick Tidal In-Stream Energy Conversion (TISEC): Survey and Characterization of Potential Project Sites. Report EPRI-TP-003-NB.

[16] Electric Power Research Institute (EPRI), 2006. Nova Scotia Tidal In-Stream Energy Conversion (TISEC): Survey and Characterization of Potential Project Sites. Report EPRI-TP-003-NS.

[17] Fisheries and Oceans Canada (DFO), 2005. WebTide Tidal Prediction Model. (www.mar.dfo-mpo.gc.ca/science/ocean/coastal_hydrodynamics/WebTide).

[18] Fisheries and Oceans Canada (DFO), 2007. Canadian Tide and Current Tables, Volume 1, Atlantic Coast and Bay of Fundy. (www.tides.gc.ca).

[19] Garret, C., 1972. Tidal resonance in the Bay of Fundy and Gulf of Maine. *Nature*, 238, 441-443, 1972.

[20] Garrett, C., 1974. Normal modes of the Bay of Fundy and Gulf of Maine. *Journal of Earth Science*, 11:549-556.

[21] Gordon, D. C. and Longhurst, A. R., 1979. The Enrionmental Aspects of a Tidal Power Project in the Upper Reaches of the Bay of Fundy. *Marine Pollution Bulletin*, 10(38):38-45.

[22] Greenberg, D. A., 1977. Mathematical studies of tidal behaviour in the Bay of Fundy. Department of Fisheries, Ottawa, Report No. 46.

[23] Greenberg, D.A., 1979. A numerical model investigation of tidal phenomena in the Bay of Fundy and Gulf of Maine. *Marine Geodesy*, 1979, 2(2), 161-187.

[24] Greenberg, D. A., 1983. Modeling the mean baratropic circulation in the Bay of Fundy and Gulf of Maine. *Journal of Physical Oceanography*, 13:886-904.

[25] Greenberg, D., Shore, J., and Shen, Y., 1997. Modelling tidal flows in Passamaquoddy Bay. *Proc. of the Maritime Atlantic Ecozone Science Workshop*, 58-64.

[26] Henderson, F. M. 1966. *Open Channel Flow*., McMillan Company, New York, USA.

[27] Hervouet, J.-M., *Hydrodynamics of free-surface flows – modelling with the finite element method.* John Wiley & Sons Ltd.

[28] Karsten, R.H., McMillan, J.M., Lickley, M.J. and Haynes, R.D., 2008. Assessment of tidal current energy in the Minas Passage, Bay of Fundy. Proc. IMechE Vol. 222 Part A: *J. Power and Energy*, 493-507.

[29] Lynch, D. R. and Naimie, C. R., 1993. The M2 tide and its residual on the outer banks of the Gulf of Maine. *J. Physical Oceanography*, 23(10): 2222-2253.

[30] Menint, L., 1986. The new design of bulb turbine units based on the experience from the Rance tidal station and on-the-river buld units. Proc. 3rd International Symposium on Wave, Tidal, OTEC and Small Scale Hydro Energy. BHRA.

[31] Parsons Brinckerhoff Ltd., Black & Veatch Ltd., 2008. Analysis of Options for Tidal Power Development in the Severn Estuary – Interim Options Analysis Report. Report to the UK DECC.

[32] Rao, D. B., 1968. Natural Oscillations of the Bay of Fundy. *J. Fisheries Research Board of Canada*, 25(6):1097-1114.

[33] Sankaranarayanan, S. and McCay, D. F., 2003. Three-Dimensional Modeling of Tidal Circulation in Bay of Fundy. *J. Waterway, Port, Coastal and Ocean Engineering*, 129(3):114-123.

[34] Smagorinsky, J., 1963. General circulation experiments with the primitive equations I: the basic experiment. *Mon. Weather Rev*., 91:99-164.

[35] Severn Barrage Committee (SBC), 1981. Tidal Power from the Severn Estuary. HMSO.

[36] Severn Tidal Power Group (STPG), 1993. Severn Barrage Project: further environmental and energy capture studies. ETSU report (TID 4099).

[37] Sucsy, P., Pearce, B., Panchang, V., 1993. Comparison of two- and three-dimensional model simulation of the effect of a tidal barrier on the Gulf of Maine tides. *J. Physical Oceanography*, 23(6), 1231-1248.

[38] Xia, J., Falconer, R., Lin, B., 2010. Impact of different tidal renewable energy projects on the hydrodynamic processes in the Severn Estuary, UK. *Ocean Modelling* 32, 86-104.

[39] Xia, J., Falconer, R.A., Lin, B., 2010. Impact of different operating modes for a Severn Barrage on the tidal power and flood inundation in the Severn Estuary, UK. *Applied Energy*, 87, 2374-2391.

[40] Xia, J., Falconer, R.A., Lin, B., 2010. Hydrodynamic impact of a tidal barrage in the Severn Estuary, UK. *Renewable Energy*, 35, 1455–1468.

[41] Zhang, A., Wei, E., and Parker, B., 2003. Optimal estimation of tidal open boundary conditions using predicted tides and adjoint data assimilation technique. *J. Continenal Shelf Research*, 23, 1055-1070.